

**STRUCTURAL CHARACTERIZATION OF THE ATG1 KINASE COMPLEX  
BY SINGLE PARTICLE ELECTRON MICROSCOPY**

by

LEON HAROLD CHEW

B.Sc., The University of British Columbia, 2011

A THESIS SUBMITTED IN PARTIAL FULFILLMENT OF  
THE REQUIREMENTS FOR THE DEGREE OF

MASTER OF SCIENCE

in

THE FACULTY OF GRADUATE AND POSTDOCTORAL STUDIES

(Biochemistry and Molecular Biology)

THE UNIVERSITY OF BRITISH COLUMBIA

(Vancouver)

December 2013

©Leon Harold Chew, 2013

## Abstract

In eukaryotes, autophagy is an evolutionarily conserved and essential “self-degradative” process used to maintain cellular homeostasis. Central to autophagy is the formation of double-membrane vesicles termed autophagosomes. The process of autophagosome formation is coordinated by over 35 autophagy-related (Atg) proteins. The Atg1 kinase complex constitutes one group of proteins required for the initial induction step of autophagosome formation. The Atg1 kinase complex is composed of the kinase Atg1, a regulatory phosphoprotein Atg13, and a protein scaffold Atg17 that forms a ternary complex with Atg31 and Atg29.

In this study, we have determined the structure of the *Saccharomyces cerevisiae* Atg17-Atg31-Atg29 ternary complex by single-particle electron microscopy. The complex is an “S-shaped” dimer exhibiting an elongated architecture with an end-to-end distance of 345Å. Atg17 was found to form the central scaffold while Atg31 and Atg29 formed two globular densities tethered to the arcs formed by Atg17. Further analysis of purified Atg17 dimers showed that Atg17 mediated dimerization of the complex while Atg31 and Atg29 had a structural role in maintaining the distinct curvature of the complex.

We further studied Atg1 kinase complex assembly by co-expressing a minimal pentameric assembly consisting of Atg1 CTD (residues 589-897) and Atg13 CTD (residues 384-738) with Atg17-Atg31-Atg29. Structural analysis localized Atg1 CTD and Atg13 CTD to the terminal regions of the ternary complex supporting that the N-terminus of Atg17 likely mediates complex assembly. Finally, we structurally characterized an important Atg1 kinase complex interacting partner, Atg11. Purified Atg11 exhibited an elongated architecture supporting its role as a coiled-coil protein scaffold.

## Preface

The following publications were based on the work performed in this thesis:

1. **Chew, L. H.**, Setiাপutra, D., Klionsky, D. J., and Yip, C. K. (2013) Structural characterization of the *Saccharomyces cerevisiae* autophagy regulatory complex Atg17-Atg31-Atg29. *Autophagy* **9**, 1467–1474.

I wrote the manuscript with C.K.Y. I designed and conducted all experiments with assistance from C.K.Y. I further interpreted the data and finally made most of the figures in the manuscript. Some figures were produced by D.S. while D.J.K. contributed to analysis and interpretation of some data.

2. Mao, K., **Chew, L. H.**, Inoue-Aono, Y., Cheong, H., Nair, U., Popelka, H., Yip, C. K., and Klionsky, D. J. (2013) Atg29 phosphorylation regulates coordination of the Atg17-Atg31-Atg29 complex with the Atg11 scaffold during autophagy initiation. *Proc. Natl. Acad. Sci. U. S. A.* **110**, E2875–84.

I designed and conducted several of the experiments in this manuscript primarily based on EM structural analysis of Atg17-Atg31-Atg29 phosphomimetic mutants. I further analyzed the data and interpreted the significance of its models. The author contributions excerpt from the manuscript is as follows:

Author contributions: K.M., Y.I.-A., H.C., U.N., H.P., C.K.Y., and D.J.K. designed research; K.M., **L.H.C.**, Y.I.-A., H.C., U.N., H.P., and C.K.Y. performed research; K.M., Y.I.-A., H.C., U.N., H.P., and C.K.Y. contributed new reagents/analytic tools; K.M., **L.H.C.**, Y.I.-A., H.C., U.N., H.P., C.K.Y., and D.J.K. analyzed data; and K.M., H.C., H.P., C.K.Y., and D.J.K. wrote the paper.

# Table of contents

Abstract.....	ii
Preface.....	iii
Table of contents.....	iv
List of tables.....	vi
List of figures.....	vii
List of abbreviations.....	viii
Acknowledgements.....	ix
Dedication.....	x
<b>Chapter 1. Introduction.....</b>	<b>1</b>
<b>1.1 Overview of autophagy.....</b>	<b>1</b>
<b>1.2 Molecular autophagy machinery required for autophagosome formation.....</b>	<b>5</b>
1.2.1 Induction.....	6
1.2.2 Elongation.....	6
1.2.3 Completion.....	7
<b>1.3 Regulation of autophagosome formation.....</b>	<b>10</b>
<b>1.4 The Atg1 kinase complex.....</b>	<b>12</b>
1.4.1 Atg1 and Atg13.....	13
1.4.2 The Atg17-Atg31-Atg29 ternary subcomplex.....	15
<b>1.5 The protein scaffold Atg11.....</b>	<b>16</b>
<b>1.6 Studying large macromolecular assemblies using electron microscopy.....</b>	<b>16</b>
<b>1.7 Thesis Overview.....</b>	<b>18</b>
<b>Chapter 2: Materials and Methods.....</b>	<b>19</b>
<b>2.1 Purification in <i>S. cerevisiae</i>.....</b>	<b>19</b>
2.1.1 TAP tagging of Atg29 and Atg31 in yeast.....	19
2.1.2 TAP purification.....	19
<b>2.2 Cloning and construction of co-expression vectors for recombinant protein expression.....</b>	<b>20</b>
2.2.1 Cloning Atg genes for recombinant expression of Atg17-Atg31-Atg29 using the pET-Duet system.....	20
2.2.2 Construction of GFP-fusion label vectors for GFP labelling of Atg31 and Atg29.....	21
2.2.3 Cloning Atg genes for recombinant expression using the pQLINK system.....	21
2.2.6 Cloning of Atg11 into the pESC yeast expression system.....	22
<b>2.3 Recombinant expression and purification.....</b>	<b>23</b>
2.3.1 Purification of recombinant Atg17-Atg31-Atg29.....	23
2.3.2 Purification of recombinant Atg1 kinase pentamer complex.....	24
2.3.3 GraFix protocol.....	25
2.3.3 Expression and purification of Atg11 using the pESC yeast expression system.....	25

2.4 Electron microscopy .....	26
2.5 Image processing .....	27
2.6 Length and curvature analysis.....	28
2.7 Bioinformatics .....	28
2.8 Construction of figures .....	28
<b>Chapter 3. Results .....</b>	<b>29</b>
3.1 Analysis of <i>in vivo</i> purification of TAP tagged Atg17-Atg31-Atg29 ternary subcomplex.....	29
3.2 Recombinant purification of the Atg17-Atg31-Atg29 ternary subcomplex .....	31
3.3 Electron microscopy analysis of the recombinant Atg17-Atg31-Atg29 ternary subcomplex .	33
3.4 Subunit localization of Atg17, Atg31 and Atg29 using GFP and MBP fusion labels. ....	34
3.5 Atg17 mediates dimerization and forms the central scaffold of the complex.....	36
3.6 Analyzing the conformational flexibility of the Atg17 dimer. ....	38
3.7 Analysis of an “autophagy-induced” complex with phosphomimetic Atg29.....	40
3.8 Purification of the Atg1 kinase complex pentamer .....	41
3.9 Structural analysis of the Atg1 kinase complex pentamer .....	44
3.10 Subunit localization of Atg1 and Atg13 in the pentamer assembly.....	47
3.11 Purification and EM analysis of Atg11 .....	49
<b>Chapter 4: Discussion .....</b>	<b>51</b>
4.1 Structure of the Atg17-Atg31-Atg29 regulatory subcomplex .....	51
4.1.1 The EM structure of <i>S. cerevisiae</i> Atg17-Atg31-Atg29 from.....	51
4.1.2 The crystal structure of <i>L. thermotolerans</i> Atg17-Atg31-Atg29 .....	52
4.1.3 The business “N” of Atg17 .....	55
4.2 Structure of the Atg1 kinase complex .....	57
4.2.1 Purification of the Atg1 kinase complex pentamer.....	57
4.2.2 The EM structure of the Atg1 kinase complex pentamer.....	58
4.2.3 Models of Atg1 kinase complex function .....	62
4.3 The EM structure of Atg11 .....	64
<b>Chapter 5. Conclusions .....</b>	<b>65</b>
<b>Chapter 6. Future Experiments .....</b>	<b>66</b>
<b>References .....</b>	<b>67</b>
<b>Appendix .....</b>	<b>78</b>

## List of tables

Table 1.1 Autophagy machinery functional groups .....	4
Table 2.1 Summary of processing parameters for data set .....	27
Appendix Table A.1 Primers used for cloning .....	78
Appendix Table A.2 Plasmids for bacterial expression.....	79
Appendix Table B.2 Mass spectrometry of TAP purified Atg17-Atg31-Atg29.....	80

## List of figures

Figure 1.1 Overview of autophagosome formation. ....	3
Figure 1.2 Hierarchy of Atg proteins.....	5
Figure 1.3 Signalling pathways regulating the <i>S.cerevisiae</i> Atg1 kinase complex.....	9
Figure 1.4 Summary of interactions mediating <i>S.cerevisiae</i> Atg1 kinase complex formation.....	12
Figure 3.1 Purification and negative stain EM analysis of native Atg29-TAP tagged complex. ....	30
Figure 3.2 <i>In vitro</i> purification and negative stain EM analysis of recombinant Atg17-Atg31-Atg29 .....	32
Figure 3.3 Mapping of Atg17-Atg31-Atg29 complex subunits.....	35
Figure 3.4 Purification and EM analysis of the MBP-Atg17 dimer.....	37
Figure 3.5 Analysis of Atg17 dimer flexibility. ....	39
Figure 3.6 Analysis of phosphomimetic Atg29 containing complexes.. ....	40
Figure 3.7 Expression and purification of Atg1 kinase complex assemblies.....	43
Figure 3.8 EM analysis of the Atg1 kinase complex pentamer. ....	46
Figure 3.9 Mapping of Atg1 CTD and Atg13 CTD in the Atg1 kinase complex pentamer.....	48
Figure 3.10 Purification and EM analysis of Atg11.....	50
Figure 4.1 The crystal structure of <i>L. thermotolerans</i> Atg17-Atg31-Atg29.....	54
Figure 4.2 The N-terminus of Atg17 forms a curved interaction interface.....	56
Figure 4.3 Intrinsically disordered protein prediction of Atg1 and Atg13 by the IUPRED server. ....	59
Figure 4.4 Model of Atg1 kinase complex assembly.....	61
Figure 4.5 Models of Atg1 kinase complex function.....	63
Appendix B.1 <i>In vivo</i> purification of Atg17-TAP and Atg13-TAP strains.....	80
Appendix C.1 Alignment of Atg17.....	82
Appendix C.2 Purified Atg13 exhibiting multiple bands.....	83
Appendix C.3 Coiled coil prediction for Atg17 and Atg11.....	83

## List of abbreviations

2D	Two-dimensional
3D	Three-dimensional
Atg	Autophagy-related
CHAPS	3-[(3-Cholamidopropyl)dimethylammonio]-1-propanesulfonate
CCD	Charge-coupled device
DNA	Deoxyribonucleic acid
dCTP	Deoxycytidine triphosphate
dGTP	Deoxyguanosine triphosphate
DTT	Dithiothreitol
EDTA	Ethylenediaminetetraacetic acid
EGTA	Ethylene glycol tetraacetic acid
EM	Electron microscopy
GFP	Green Fluorescent Protein
GraFix	Gradient Fixation
GST	Glutathione S-transferase
HEPES	2-[4-(2-hydroxyethyl)piperazin-1-yl]ethanesulfonic acid
IgG	Immunoglobulin G
LIC	Ligation independent cloning
MBP	Maltose Binding Protein
PAGE	Polyacrylamide gel electrophoresis
PMSF	Phenylmethylsulfonyl fluoride
SDS	Sodium dodecyl sulphate
SGD	Saccharomyces Genome Database
TAP	Tandem affinity purification
TCA	Trichloroacetic acid
TEV	Tobacco etch virus
TOR	Target of rapamycin
Tris-HCl	2-Amino-2-hydroxymethyl-propane-1,3-diol
Ura	Uracil
Y2H	Yeast two-hybrid

## Acknowledgements

I would first like to thank my family for their unyielding support, patience and care. Next, I would like to thank my supervisor Dr. Calvin Yip for the opportunity to work on such a stimulating and exciting project. There have been many highs and lows during the course of my study and he has been a pillar of support and knowledge. I have been especially inspired by his compassion and kindness that has not gone unnoticed. It has been a pleasure to have worked in such a young and enthusiastic lab environment where we are encouraged to explore. The rest of the members of the Yip lab deserve due praise. Dheva Setiাপutra has been a great colleague, classmate and friend during grad school that I know will amount to great things. Katarina Prieцelova, Samantha Schaffner, James Ross, Franco Li, Celine Chan and Hayeong Rho have all contributed to aspects of this study and their assistance has been greatly appreciated. Martine Boutine has been a superb tech that provided technical assistance and knowledge. Dr. Angela Yu and Dr. Catherine Chan have also provided helpful discussion. I would also like to thank Dr. Daniel J. Klionsky and Kai Mao from the University of Michigan. Dr. Klionsky was a catalyzing force in starting this project in our lab. Without him it would have been unlikely I would have had such an exciting project to work on and been introduced to the amazing field of autophagy research.

Additionally, I would like to thank all old and new members of the van Petegem lab. They provided essential reagents for the GFP labelling experiments. I would especially like to thank Jett Tung and Lynn Kimlicka who first taught me cloning and protein purification. I would also like to thank Paolo Lobo, Michael Yuchi, Kelvin Lau and Samir Das who also contributed to great discussion.

I would also like to thank my committee members, Dr. Elizabeth Conibear, Dr. Filip van Petegem and my examination chair Dr. Michel Roberge, for providing useful input and making graduate studies relatively smooth sailings. Finally I would like to thank Dr. Pascal Lavoie, Dr. Bernd O. Keller, Cristina Martins and additional thanks to Dr. Filip van Petegem for providing references so that I could obtain NSERC funding.

## **Dedication**

To my mother, father, sister and brother.

# Chapter 1. Introduction

## 1.1 Overview of autophagy

The ability of cells to maintain homeostasis through synthesizing and degrading intracellular components is a fundamental process required for life. In eukaryotes, two branches are responsible for protein degradation; the proteasome-ubiquitin conjugation system and autophagy in conjunction with the vacuole/lysosome<sup>1,2</sup>. Unlike the proteasome-ubiquitin system, autophagy has the capacity to degrade much larger cargo such as protein aggregates and even whole organelles<sup>1</sup>. In this role, autophagy is an essential adaptive degradative mechanism to remove cellular components during a defined physiological state.

Several forms of autophagy exist and include: chaperone-mediated autophagy<sup>3</sup>, microautophagy<sup>4</sup>, and macroautophagy<sup>5</sup>. The three forms of autophagy differ in the mechanism of sequestering cargo and delivery of cargo to the degradative compartment. Chaperone-mediated autophagy requires the formation of a chaperone-substrate complex, which associate with a lysosomal receptor to mediate fusion and degradation<sup>3</sup>. Microautophagy is the direct engulfment of cytoplasm through invagination of the vacuole/lysosome membrane<sup>4</sup>. Microautophagy is poorly characterized except in the case of micropexophagy (peroxisome degradation) in methylotrophic yeast or micronucleophagy (nuclear degradation)<sup>5</sup>. Nonselective macroautophagy (hereafter autophagy) is the most extensively studied form of autophagy and is thought to be the primary form in cells<sup>5</sup>. Another autophagy-like pathway worth mentioning is the cytoplasm-to-vacuole (Cvt) pathway only found in yeast<sup>6</sup>. This pathway is a selective and anabolic form of autophagy that shares many of the components required for autophagy. The Cvt pathway is required for the synthesis and delivery of two resident vacuolar hydrolases, ApeI and AmsI, to the vacuole. Together these various forms of autophagy function to deliver cytoplasmic components to the degradative compartment.

Autophagy's primary role is adapting to conditions of stress, such as nutrient deprivation, oxidative stress, and hypoxia. In this response, autophagy promotes homeostasis by regenerating essential

macromolecules and ATP for biosynthesis and by removing deleterious cellular debris<sup>7,8</sup>. Importantly, autophagy has been recognized to occur at a basal level in most cell types independent of extraneous stressors and its function is required for the proper maintenance of cells<sup>9,10</sup>. Due to autophagy's central role in homeostasis, deregulation of this pathway is associated with many human diseases<sup>11,12</sup> including neurodegeneration<sup>9</sup>, myopathies<sup>13</sup>, cancer<sup>10</sup>, cellular immunity<sup>14</sup>, and aging<sup>15</sup> and is further involved in diverse physiological processes such as growth and development, differentiation and apoptosis<sup>16</sup>. Thus, it is not surprising that further understanding the molecular details of this pathway has important implications in human health and disease.

Autophagy was first discovered in the 1950s as a morphological phenomenon where cytoplasmic components were observed to be encapsulated in double-membrane structures<sup>17</sup>. The frequency of these observations was increased in cells exposed to nutrient deprivation or catabolic hormones, such as glucagon<sup>17,18</sup>. These double-membrane organelles are now known as autophagosomes and have a principal role in mediating autophagy function through engulfment of cytoplasmic material and delivery to the vacuole/lysosome (Figure 1.1). Autophagosome synthesis begins at the preautophagosomal structure (PAS) and is thought to occur in a sequential manner<sup>5,19,20</sup>. Fusion of smaller vesicles leads to expansion and formation of a cup-shaped membrane sac, termed an isolation membrane or phagophore. Cytoplasmic content becomes sequestered into the growing membrane structure until the vesicle is sealed forming a double-membrane autophagosome ~300 to 900 nm in diameter. Mature autophagosomes are subsequently delivered to the vacuolar/lysosomal compartments where the outer membrane fuses with the vacuolar/lysosomal membrane leading to the delivery of the inner vesicle encapsulating the cargo into the lumen of the lysosome. Hydrolytic enzymes degrade the inner membrane vesicle, termed an autophagic body, and the resulting metabolites can be recycled for anabolic pathways. Before the early 1990s, the study of autophagy was limited due to the transient nature of the autophagosome. The discovery of autophagy in the baker's yeast *Saccharomyces cerevisiae* have allowed scientist to determine the molecular mechanisms of autophagosome formation<sup>21,22</sup>.

# 1. Initiation

# 2. Elongation

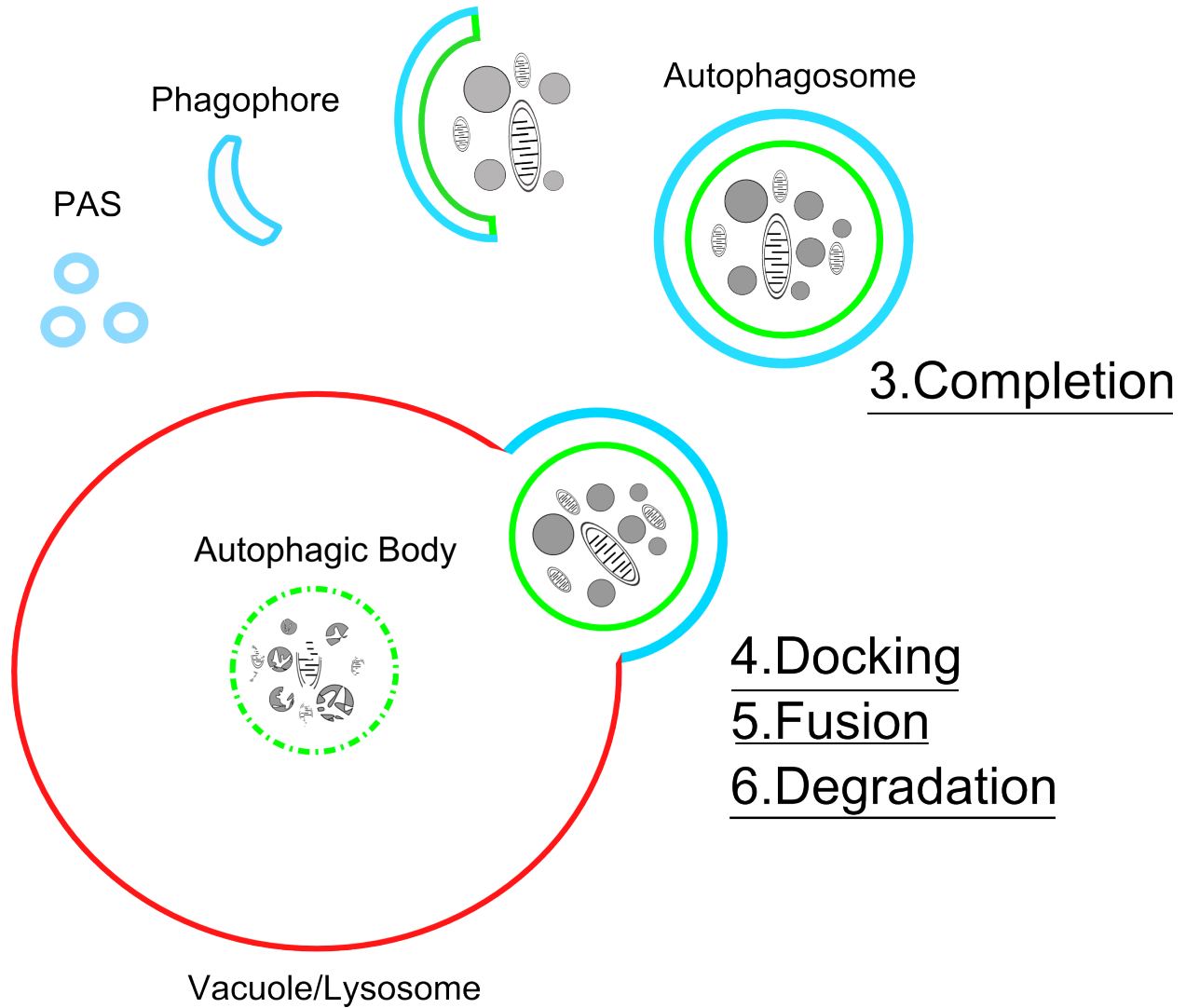


**Figure 1.1 Overview of autophagosome formation.** Autophagosome formation initiates at the preautophagosomal structure (PAS). The PAS matures into a phagophore followed by nucleation and elongation events leading to formation of a cup-shaped sac. Cytoplasmic content is encapsulated by this growing double-membrane structure until completion of the autophagosome. The mature autophagosome is then delivered to the degradative body, vacuole/lysosome, where the inner membrane vesicle is deposited. Hydrolases lead to the degradation of the autophagic body.

**Table 1.1 Autophagy machinery functional groups**

<b>Functional Group</b>	<b>Role in Autophagosome Formation</b>	<b>Yeast</b>	<b>Human</b>
Atg1 Complex	Atg1 is a serine/threonine kinase with a role in tethering membranes. Atg17-Atg31-Atg29 acts a scaffold for assembling the Atg1 complex	Atg1	ULK1
		Atg13	ATG13
		Atg17	FIP200
		Atg29	
		Atg31	
			ATG101
PI(3)K Complex	Produces Ptdins(3)P on autophagic membranes. Atg14 and Atg6 have shown membrane-binding capabilities.	Vps34	VPS34
		Vps15	VPS15
		Atg14	ATG14L/BARKOR
		Vps30/Atg6	Beclin1
Atg9	Integral membrane protein. Provides early membrane source for PAS formation.	Atg9	Atg9
Atg18–Atg2 complex	Atg18 specifically binds PI(3)P. Recruits ubiquitin-like conjugation system and recycles Atg9	Atg18	WIPI1-4
		Atg2	Atg2
Atg12 conjugation	Atg12 is conjugated to Atg5 through a ubiquitin-like cascade. Atg12-Atg5 conjugates form a complex with Atg16. Atg5 can bind membranes and may tether membranes through dimerization of Atg16.	Atg12	ATG12
		Atg7	ATG7
		Atg10	ATG10
		Atg5	ATG5
		Atg16	ATG16L1/2
Atg8 conjugation	Atg8 is lipidated to PE through an ubiquitin-like cascade. Atg4 proteolytically activates Atg8 followed by conjugation to the enzymes Atg7 (E1), Atg3 (E2). Atg8-PE conjugates tether membranes.	Atg8	LC3A/B/C GABARAP GATE-16
		Atg4	ATG4A-D
		Atg7	ATG7
		Atg3	ATG3

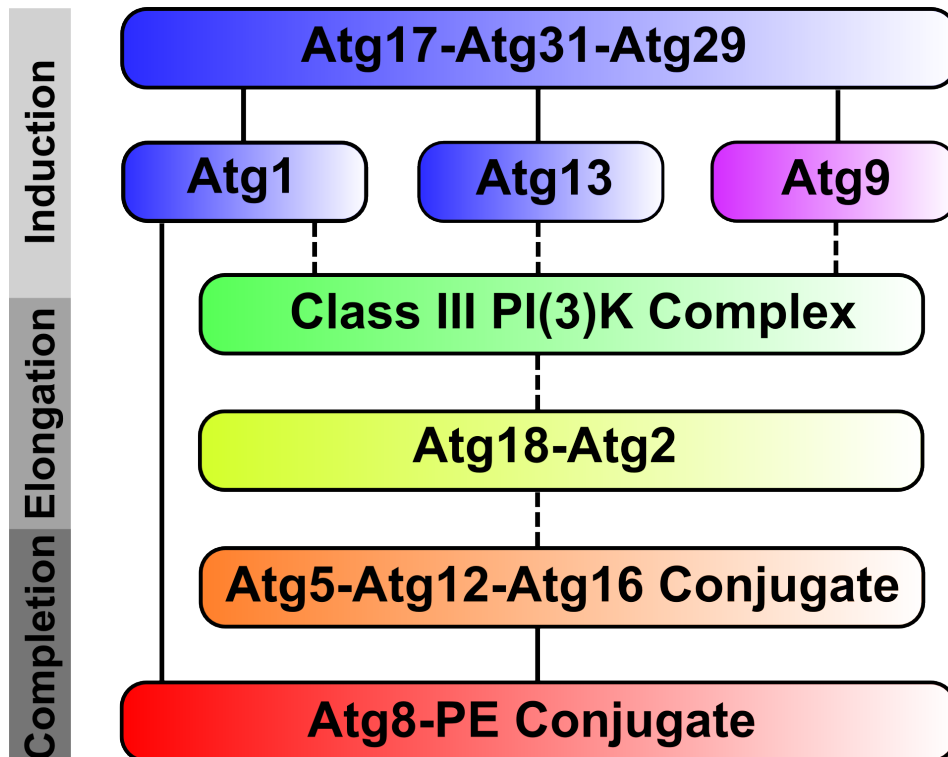


**Figure 1.2 Hierarchy of Atg proteins.** Groups of Atg proteins are recruited to the PAS in a step-wise manner and function at different stages. The Atg1 kinase complex serves as a scaffold, through Atg17-Atg31-Atg29. Solid lines are confirmed physical interactions between protein groups while dotted lines are genetic interactions. The functions for each protein group are described in Table 1.1.

### 1.2 Molecular autophagy machinery required for autophagosome formation

Various genetic screens carried out in *Saccharomyces cerevisiae* and other fungal species led to the identification of more than 35 AuTophaGy-related (Atg) genes<sup>22</sup>. Of these Atg genes, approximately 18 core proteins are essential for autophagosome formation in yeast and can be classified into five functional groups based primarily on identified protein-protein interactions<sup>19</sup> (Table 1): (i) the Atg1 kinase complex, (ii) the autophagy-specific phosphatidylinositol 3-kinase (PI(3)K) complex, (iii) Atg9 and the Atg2-Atg18 cycling system, (iv) the Atg12 conjugation system, and (v) the Atg8 conjugation system. Importantly, the autophagy pathway and core machineries are evolutionarily conserved with more than half of the Atg proteins in yeast having orthologs in higher eukaryotes (Table 1). Through the use of yeast gene deletion strains, the hierarchical relationship between the different groups of Atg proteins was established (Figure 1.2)<sup>23,24</sup>. Each group of Atg proteins functions at a different step of autophagosome formation, which can be divided into several steps: induction, elongation, and completion<sup>20</sup>.

### 1.2.1 Induction

Induction of autophagosome formation occurs through activation and localization of the conserved Atg1 kinase complex to the PAS<sup>25</sup> (further discussed in section 1.3 and 1.4). Atg1 is a serine/threonine kinase whose activity is regulated by its association with several proteins: Atg13, a phosphoprotein, Atg17, a protein scaffold, and two non-conserved regulatory subunits, Atg31 and Atg29. This complex is an important regulatory hub that initiates autophagosome formation<sup>25</sup>. Once activated, the Atg1 kinase complex functions to further localize and activate factors, such as Atg8 and Atg14, to the PAS to mediate autophagosome elongation<sup>25,95</sup>.

### 1.2.2 Elongation

Addition of new membrane to the PAS mediates the elongation phase of nascent autophagosome formation. The exact origin of the membrane source is unclear but it has been speculated to derive from several compartments including mitochondria<sup>26,30</sup>, Golgi<sup>27</sup>, ER<sup>27,28,30</sup>, and plasma membrane<sup>29</sup>. What is known is that Atg9, the only transmembrane protein essential for autophagy, likely has a role in contributing some membrane to the growing autophagosome<sup>31,32</sup>. Atg9 has six predicted transmembrane segments with both termini projecting to and localized in the cytoplasm<sup>33</sup>. Atg9 is present in high curvature 30-60 nm lipid vesicles known as Atg9 vesicles, which are believed to be derived from Golgi-endosome sources<sup>32</sup>. The Atg1 kinase complex has a role in recruiting Atg9 through Atg17<sup>34,35</sup>. Additional factors including Atg23 and Atg27 are also required for Atg9 vesicle formation<sup>32</sup>. In nutrient rich conditions, Atg9 vesicles exist as a pre-PAS. Upon induction of autophagy, several Atg9 vesicles are trafficked to the vacuole to form the initial isolation membrane and provide the first membrane source for the autophagosome. It is thought that as little as three Atg9 vesicles participate in this early autophagosome biogenesis event<sup>32</sup>. Because Atg9 vesicles likely contribute only a small amount of membranes to autophagosomes, these specialized lipid vesicles may possess alternative functions to conscript additional membrane sources. Indeed, recent studies revealed that Atg9 recruits the TRAPP III vesicle tethering complex and Ypt1 Rab GTPase to the PAS<sup>36,37</sup>.

Another required feature for elongation is the generation of phosphatidylinositol 3-phosphate (PI(3)P), on autophagic membranes<sup>38,39</sup>. In yeast, the primary module required for *de novo* PI(3)P synthesis is the class III PI(3) kinase (PI(3)K) complex<sup>40</sup> which is composed of Vps34, the sole catalytic class III PI(3)kinase, Vps15, a myristoylated regulatory serine/threonine kinase, Vps30 (aka Atg6), the autophagy specific Atg14, and a recently discovered component, Atg38<sup>41</sup>. Together, this complex is targeted to the PAS, through Atg14<sup>42,43,44</sup> and by membrane association with Vps30<sup>45</sup>. Targeting of this complex to the PAS promotes phosphorylation of the PAS by Vps34, which ultimately leads to recruitment of additional Atg protein effectors.

The production of PI(3)P recruits Atg18<sup>46,47</sup>, Atg20<sup>48</sup>, Atg21<sup>49</sup> and Atg24<sup>50</sup> that associate with autophagic membranes through phosphoinositide binding domains<sup>51</sup>. Of these proteins Atg18<sup>47</sup> is required for autophagy while Atg20 and Atg24 have been implicated in the Cvt pathway<sup>48</sup>. Interestingly, both electron and fluorescent microscopy based studies have shown that PI(3)P is enriched on the inner surface of the autophagosome membrane, and inhibiting the production of PI(3)P completely abolishes the autophagic response during starvation conditions<sup>39</sup>. However, aside from its role in recruitment of Atg proteins, the significance of PI(3)P localization to the inner surface of autophagosomes is not clear.

The PI(3)P effector, Atg18, forms a complex with Atg2<sup>47</sup>. Recent studies have shown that Atg2 can localize to the PAS independent of Atg18. The importance of Atg2 localization is highlighted by the observation that artificially inducing PI(3)P targeting of Atg2 can rescue the autophagy defect resulting from the absence of Atg18<sup>52</sup>. The exact biological functions of the Atg18-Atg2 complex are not known but likely have a role in recycling Atg9 and further recruit the ubiquitin-like conjugation systems to the growing phagophore<sup>35,53</sup>.

### 1.2.3 Completion

The sealing and completion of autophagosomes are mediated by two ubiquitin-like conjugation systems<sup>54,55</sup>. Each system has a unique ubiquitin-like protein, Atg8 or Atg12, which are conjugated to phosphatidylethanolamine (PE) or Atg5, respectively. The process of Atg12 conjugation to Atg5 can be

separated into several distinct events<sup>54</sup>. First, the C-terminal Gly186 residue of Atg12 forms a thioester linkage with Cys507 of the E1-like enzyme Atg7. Atg12 is then transferred to the E2-like enzyme Atg10 before finally being conjugated to Lys149 of Atg5. The Atg12-Atg5 conjugate, through Atg5, can further form a non-covalent complex with Atg16. The Atg12-Atg5-Atg16 complex, which is capable of forming higher-order oligomers, localizes to the concave side of the expanding phagophore and dissociates prior to autophagosome completion. Importantly, the Atg12-Atg5-Atg16 complex has E3-like activity to promote lipidation of Atg8 to form the Atg8-PE conjugate<sup>56</sup>.

Lipidation of Atg8 with PE proceeds through a conjugation event<sup>55</sup>. First, nascent Atg8 is proteolytically processed at a C-terminal arginine by the Atg4 cysteine protease to expose a glycine residue. Next, this glycine residue is activated by adenylation to form a thioester bond with Cys507 of the E1-like enzyme Atg7. Atg8 is then transferred to a cysteine residue of the E2-like enzyme Atg3. In the final step, Atg8 is conjugated to the amino group of PE, which is mediated by the Atg12-Atg5-Atg16 complex. Importantly, Atg8 is the only Atg protein to be transcriptionally upregulated during autophagy induction and serves as a marker for autophagy due to its change in localization from the cytosol to a membrane bound form. Both the Atg8-PE conjugate and the Atg12-Atg5-Atg16 complex are likely to have a role in tethering membranes to promote the completion and closure of the autophagosome. Atg16 in particular has the capacity to self dimerize<sup>57</sup>. Furthermore, deconjugation of Atg8-PE by the protease Atg4 is important for autophagosome maturation and autophagic flux<sup>58,59,60</sup>.

The final fate of mature autophagosomes is delivery and fusion with degradative compartments. The inner vesicle of the autophagosome, termed an autophagic body, is released into the lumen of the vacuole/lysosome and is subsequently degraded by hydrolytic enzymes, such as Atg15<sup>61</sup>. The resulting macromolecules are recycled by vacuolar effluxers, Atg22, Avt3 and Avt4, which shuttle free amino acids back into the cytoplasm for anabolic processes<sup>62</sup>.

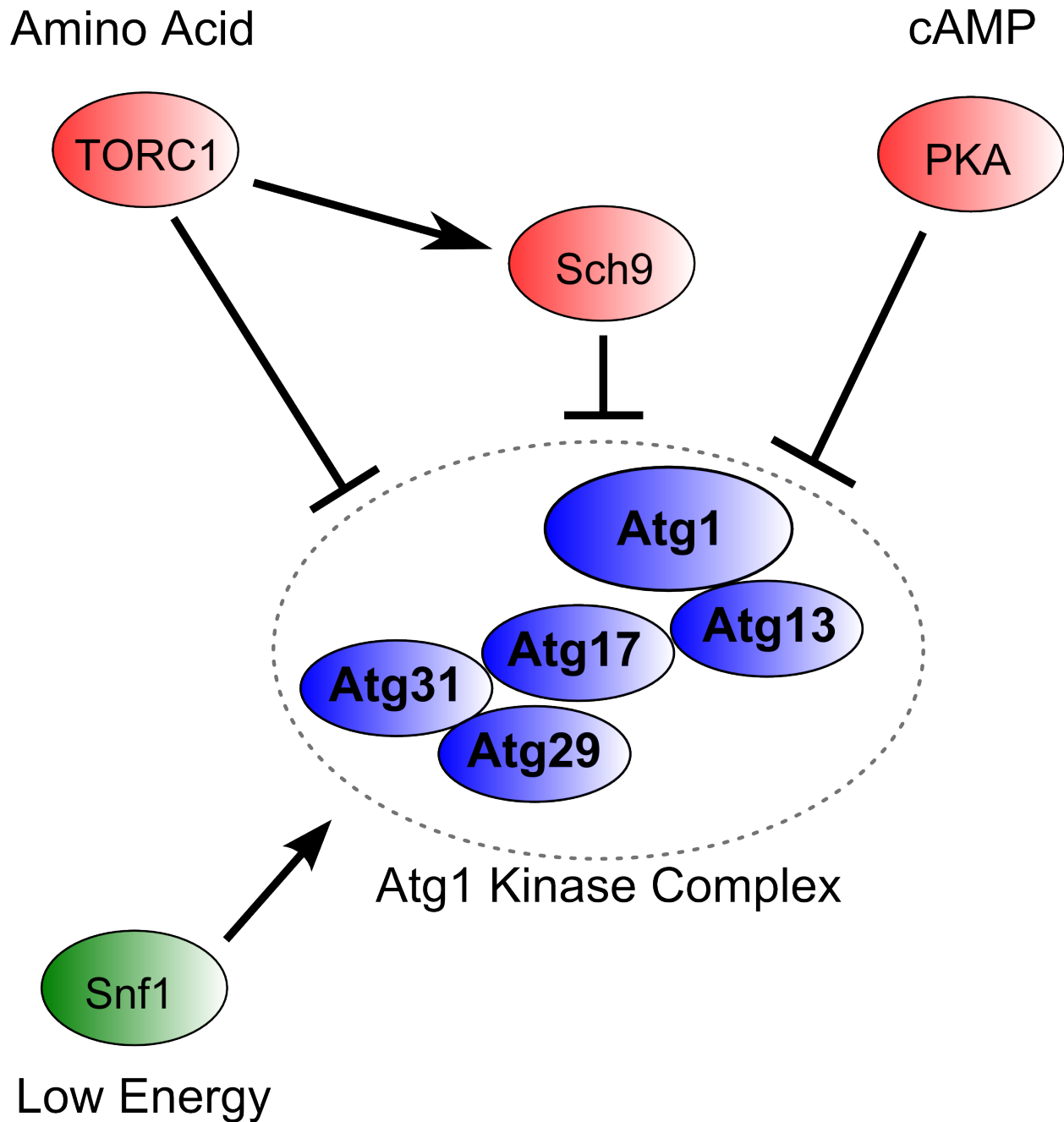


**Figure 1.3 Signalling pathways regulating the *S. cerevisiae* Atg1 kinase complex.** TORC1 sense amino acid levels in cells. During nutrient rich conditions, TORC1 is active and activates Sch9 (or SK6) while inhibiting the Atg1 kinase complex. PKA senses the cAMP levels in cells produced by the activity of adenylyl cyclase. During high cAMP signalling PKA inhibits the Atg1 kinase complex. Snf1 (or AMPK) is activated by sensing a low ATP/AMP ratio in the cell. This signal promotes Snf1 activation of the Atg1 kinase complex.

### 1.3 Regulation of autophagosome formation

During normal cell growth, autophagy is kept at a low basal level, but is highly induced during periods of stress. One of the major inducers of autophagy is nutrient deprivation, which is signalled through the action of different kinases including the target of rapamycin (TOR)<sup>63,64, 67,73</sup>, protein kinase A (PKA)<sup>64</sup>, and AMP-activated protein kinase (AMPK)<sup>65,66</sup> (Figure 1.3).

In yeast, TOR (homolog of mTOR) is a conserved serine/threonine kinase of the phosphoinositide 3-kinase (PI3K)-related kinase (PIKK) family<sup>67,68</sup>. TOR is aptly named due to its targeted inhibition by the immunosuppressive drug rapamycin<sup>67,68</sup>. TOR forms two signalling complexes in yeast: TOR complex 1 (TORC1), and TOR complex 2 (TORC2). TORC1 receives information about the amino acid status of cells from the tuberous sclerosis complex (TSC1-TSC2) where upstream signals converge<sup>68</sup>. Under nutrient rich conditions, TORC1 is active and will inhibit autophagy through phosphorylation of Atg13 and Atg1, components of the Atg1 kinase complex<sup>63,64</sup>. Inactivation of TORC1 leads to rapid dephosphorylation of Atg13 and removal of inhibition leading to autophagy. TORC1 is an important regulator of autophagy and inhibition of the complex with rapamycin mimics starvation. Rapamycin has been widely used as an agent to induce autophagy independent of nutrient status in the cell. Additionally, Sch9 (homolog of the mammalian SK6 kinase) is a serine/threonine kinase and downstream target of TORC1. Increased TORC1 signalling also increases the kinase activity of Sch9, which inhibits autophagosome formation. Importantly, inactivation of Sch9 is sufficient to promote autophagy<sup>69</sup>, highlighting an additional layer of regulation for autophagosome formation.

The Ras/PKA pathway represents another nutrient-dependent pathway that has an important role in regulating autophagy<sup>64,69,70</sup>. In nutrient rich conditions, the small GTPase RAS enhances cAMP production through adenylyl cyclase. Free cAMP in the cell activates PKA activity, which acts on Atg13 to inhibit autophagy. Further inactivation of PKA was shown to be sufficient to induce autophagy, indicating a central regulatory role for PKA<sup>64,69</sup>. Both TORC1 and PKA phosphorylate Atg13 but do so at different sites<sup>64</sup>. Interestingly, the simultaneous inactivation of the TORC1 and PKA pathways produced a

synergistic increase in autophagy activation defining that the inhibitory function work through separate mechanisms<sup>64</sup>.

A final positive regulator that has been identified is Snf1 (homolog of mammalian AMPK). Snf1 is a serine/threonine kinase whose activity is regulated by the relative energy levels in the cell<sup>65,66</sup>. Snf1 is allosterically activated by a decreased ATP/AMP ratio indicative of an energy crisis. Snf1 activity increases autophagy activity in cells presumably through Atg1, although the molecular mechanism has yet to be elucidated in yeast<sup>65</sup>. In mammalian cells, AMPK has been shown to directly phosphorylate ULK1 kinase, a component of the ULK1 complex (mammalian homolog of Atg1 kinase complex)<sup>66</sup>. Importantly, TORC1 also has an effect on Snf1, and under nutrient-rich conditions Snf1 is inactivated by TORC1<sup>71</sup>. Thus a network of interactions and regulation exist between the upstream nutrient-sensing kinases to control autophagy activation. Evidently, the common factor between these pathways is the convergence of regulation on the Atg1 kinase complex, thus highlighting its essential role as a hub for autophagy induction and regulation<sup>72,73,74,75</sup>.

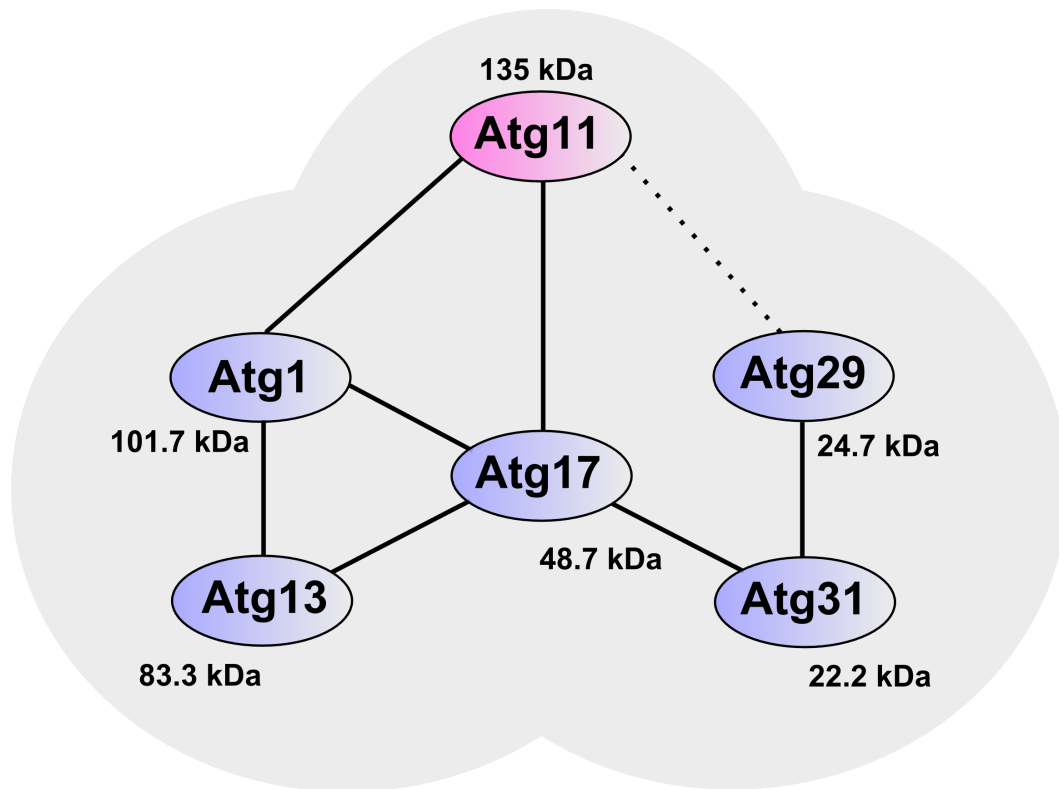


**Figure 1.4 Summary of interactions mediating *S.cerevisiae* Atg1 kinase complex formation.** Map of interactions between components of the Atg1 kinase complex that include the core components; Atg1, Atg13, Atg17, Atg31 and Atg29 while Atg11 is proposed to serve a similar role as Atg17 during non-starvation conditions and in the Cvt pathway. Solid lines are confirmed physical interactions between proteins while dotted lines are genetic interactions. Molecular weights are depicted.

#### 1.4 The Atg1 kinase complex

In yeast, the Atg1 kinase complex consists of five core subunits; Atg1, Atg13 and a ternary subcomplex composed of Atg17, Atg31 and Atg29 (Figure 1.4). Evidence for formation of this complex was identified primarily through yeast-2-hybrid, co-immunoprecipitation and mass spectrometry analysis<sup>63,76,77,78,79</sup>. This pentameric assembly coordinates early events in autophagosome formation by recruiting effectors to the PAS and by activating Atg1 kinase activity. In mammalian cells, the ULK1 kinase complex is functionally analogous to the yeast Atg1 kinase complex<sup>80</sup>. The ULK1 complex is composed of ULK1, mATG13, FIP200, the orthologs of Atg1, Atg13 and Atg17 respectively, and a unique component ATG101<sup>81</sup>. Functionally, the Atg1 kinase complex likely has a role in tethering membrane vesicles and as a scaffold to recruit downstream effectors, these roles will be discussed.

### 1.4.1 Atg1 and Atg13

Yeast Atg1 is an 897 amino acid (101.7 kDa) serine/threonine kinase and was one of the first autophagy genes characterized<sup>82</sup>. Yeast Atg1 has two functional domains: an N-terminal kinase domain (residues 1-331) and a C-terminal domain (residues 550-897) required for protein-protein interactions<sup>83</sup>. These two domains mediate distinct functions. Atg1's kinase-dependent function is in autophosphorylation of key residues in its activation loop that promote autophagy<sup>83,84</sup>. Autophosphorylation required complex formation with Atg17 and Atg13 and was increased during the autophagy response<sup>84</sup>. Although important for autophagy, Atg1's kinase function has been found to be dispensable during induction<sup>85</sup>, and has been implicated only in the late-stages of autophagosome formation. Aside from itself, an endogenous Atg1 kinase substrate has yet to be identified in *S. cerevisiae*<sup>86</sup>. Atg1 substrates have been identified in fly and human systems with one example showing direct activation of the PI(3)K complex through phosphorylation of Beclin1, the homolog of Vps30<sup>87</sup>.

Conversely, the kinase-independent function of yeast Atg1 has been widely studied. The C-terminal domain of Atg1 has been found to associate with at least seven different Atg proteins; Atg13<sup>63</sup>, Atg17<sup>63</sup>, Atg31<sup>88</sup>, Atg29<sup>88</sup>, Atg11<sup>63</sup>, Atg8<sup>89,90</sup> and Atg9<sup>32</sup>. While Atg17, Atg29 and Atg31 are required for starvation-induced autophagy<sup>90</sup>, Atg11 has a role in the Cvt pathway<sup>24</sup>. The interaction of Atg13 with Atg1 was found to be essential for activating Atg1 kinase activity and the autophagy response<sup>63</sup>. More specifically, the C-terminal domain of Atg1 was shown to mediate interaction with Atg13 and is likely to be important for complex integrity<sup>78,91</sup>. Indeed, the Atg1-Atg17 interaction is mediated by a bridging interaction with Atg13<sup>78,91</sup>.

Additionally, Atg1 interacts with Atg8 through a conserved LIR (LC3-interacting) motif localized to the central region of Atg1<sup>89,90</sup>. This interaction does not upregulate Atg1 kinase activity but rather likely mediates Atg1's role during the late stages of autophagosome formation. This interaction mediates degradation of Atg1 and likely has a role in autophagic flux as a way to dampen the autophagy response. Recently, a C-terminal domain of Atg1 was discovered to have the ability to bind and tether small (<50 nm) highly curved membranes *in vitro*<sup>92</sup>. Interestingly, this domain could self-dimerize which may further

promote vesicle fusion. Further evidence for Atg1's membrane binding role has come in the observation that the Rab GTPase, Ypt1, recruited Atg1 to the PAS<sup>93</sup>. Ypt1 is a component of the TRAPP<sup>III</sup> vesicle tethering complex.

Yeast Atg13 is a 738 amino acid (83.2 kDa) protein and is considered a regulatory subunit of the Atg1 kinase complex<sup>94</sup>. Atg13 is a phosphoprotein and a direct substrate of the aforementioned regulatory kinases (see section 1.3). Atg13 contains a structured N-terminal domain and a predicted unstructured C-terminal domain that is thought to mediate interaction with Atg1 and Atg17. During nutrient-rich conditions Atg13 is highly phosphorylated, while upon induction of autophagy Atg13 is rapidly dephosphorylated. TORC1 induced Atg13 phosphorylation sites have been mapped out using mass spectrometry analysis with and without rapamycin treatment to chemically induce starvation<sup>73</sup>. The majority of these sites were mapped to the C-terminal region of Atg13 and may prove to be important regulatory residues for interaction with Atg17 and Atg1. The dephosphorylation of Atg13 precedes autophagy induction. Indeed, an unphosphorylatable form of Atg13 is sufficient to induce autophagy<sup>73</sup>. Biochemically, Atg1 was found to only interact with dephosphorylated Atg13, which suggests that the Atg1-Atg13 interaction only forms during starvation conditions<sup>63</sup>. However, recent evidence has shown that Atg1 and Atg13 are constitutively associated, regardless of nutrient status; similar to what has been observed in higher eukaryotes<sup>89</sup>. These conflicting observations have shed doubt on an established model for Atg1 kinase complex assembly in yeast.

The structure of an N-terminal region of Atg13 (residues 1-268) was recently determined by X-ray crystallography<sup>95</sup>. This previously unidentified Atg13 domain shows structural similarity to the HORMA (Hop1p, Rev1p, and Mad2) domain family of proteins that are involved in recognizing DNA damage<sup>96</sup>. From this structure, a potential function for recruitment of the PI(3)K complex was proposed. Deletion of the Atg13 HORMA domain results in the loss of Atg14 localization to the PAS and a defect in autophagy. A putative phosphate sensor in the HORMA domain was implicated in Atg14's localization to the PAS. Another recent study has further shown that the N-terminus region of mammalian ATG13

(mATG13) can associate with mono-phosphorylated phosphatidylinositol (PI(3)P and PI(4)P), indicating a role of the mATG13 HORMA domain in binding this important lipid modification (see section 1.2.2).

#### 1.4.2 The Atg17-Atg31-Atg29 ternary subcomplex

Atg17 is a 417-amino acid (48.7 kDa) protein that forms a ternary subcomplex with Atg31 and Atg29. Atg17 was first discovered as an interacting partner of the Atg1-Atg13 complex through its predicted coiled-coil domains<sup>63,76</sup>. Functionally, the role of Atg17 in autophagosome formation has largely been studied using a yeast strain harbouring a deletion of the *atg17* gene (*Atg17Δ*)<sup>76,77,78,91</sup>. The *Atg17Δ* strain exhibited a mild defect in the autophagy response. Intriguingly, *Atg17Δ* strains produced autophagosomes that were less than half their normal size<sup>76,91</sup>. These observations are likely due to the compensatory effect of another protein, Atg11, which has a role in acting as a PAS organizer during the Cvt pathway (see section 1.5). Indeed in *Atg17Δ/Atg11Δ* strains, autophagosomes do not form, which coincides with mislocalization of key essential Atg genes, such as Atg1 and Atg8<sup>77,78</sup>. These results indicate that Atg17, perhaps in conjunction with Atg11, are the first proteins localized to the PAS.

Atg17, with Atg31 and Atg29 serves as a platform for assembly of the full Atg1 kinase complex during autophagy induction. Evidence for formation of this subcomplex has come from yeast 2-hybrid (Y2H) and co-immunoprecipitation (co-IP) analysis<sup>77,79,88,97,98</sup>. Atg17 was shown to directly interact with Atg31 while Atg29 is likely bridged to Atg17 through Atg31<sup>79</sup>. Both Atg29 and Atg31 were found to be essential for the autophagy response<sup>97,98</sup>. *In vivo* biochemical studies have shown that this subcomplex exists as a constitutive dimer independent of nutrient status<sup>88</sup>. Furthermore, Atg17, Atg31 and Atg29 were recombinantly co-expressed in an *E.coli* system showing that Atg17-Atg31-Atg29 could be stably purified as a ternary complex<sup>88</sup>.

The two smaller components of the Atg17-Atg31-Atg29 complex, Atg31 and Atg29, may have regulatory roles in complex function. Atg31 and Atg29 are both phosphorylated under starvation conditions<sup>88,99</sup>. Although the physiological role of Atg31 phosphorylation is unknown, it was recently determined that Atg29 phosphorylation is functionally important for autophagy<sup>99</sup>. Putative Atg29

phosphorylation sites were mapped out and a C-terminal region was identified to be essential for autophagy function and PAS localization. Importantly, phosphorylated Atg29 required the protein scaffold Atg11 to promote localization of the Atg17-Atg31-Atg29 complex to the PAS.

### **1.5 The protein scaffold Atg11**

Atg11 was initially discovered as a protein essential for the Cvt pathway that transports two resident vacuolar hydrolases, ApeI and AmsI, from the cytosol to vacuole in *S. cerevisiae*<sup>6,100</sup>. The two hydrolases are packaged by a specific receptor, Atg19, as a large complex into 100-200 nm double-membrane vesicles, termed Cvt vesicles<sup>101</sup>. Cvt vesicles are markedly smaller than autophagosomes. Cvt vesicles are then delivered to the vacuole. The Cvt pathway is mechanistically similar to autophagosome formation despite apparent conflicting function; the Cvt pathway is an anabolic process while autophagy is a catabolic degradative process. Intriguingly, both pathways share all components of the autophagosome machinery.

Atg11 is an 1178-amino acid (135 kDa) that is predicted to contain four coiled-coil domains<sup>101</sup>. Atg11 has been shown to interact with many proteins including Atg1, Atg17, Atg29, Atg20, Atg19 and is predicted to homodimerize through a central domain. As mentioned previously, despite an assigned function in the Cvt pathway, Atg11 likely has a role in mediating an effective autophagy response as an early PAS organizer during normal conditions required prior to activation of starvation-induced autophagy. Atg17 and Atg11 likely have redundant roles as PAS organizers. Furthermore Atg11 is necessary for recruitment of the Atg17-Atg31-Atg29 complex to the PAS in the absence of other Atg proteins. A genetic interaction of Atg11 with the Atg31-Atg31-Atg29 complex was observed to be mediated through Atg29<sup>99</sup>. Thus, an intimate functional relationship exists between the Atg17-Atg31-Atg29 complex and Atg11 in their roles as protein scaffolds.

### **1.6 Studying large macromolecular assemblies using electron microscopy**

In the field of structural biology, three techniques are predominantly used for structure determination: X-ray crystallography, nuclear magnetic resonance (NMR) spectroscopy, and single-

particle electron microscopy (EM). These techniques provide useful structural information of macromolecules through different means of data acquisition. X-ray crystallography obtains diffraction patterns from a protein crystal, while NMR relies on the physical phenomenon of nuclear spin in a magnetic field to obtain a NMR absorption spectrum. For single-particle EM, macromolecules are directly imaged through the use of a high-powered transmission electron microscope (TEM). Each technique has its own inherent strengths and weaknesses. X-ray crystallography and NMR have both been the primary methods for protein structural determination with the potential to obtain atomic level resolution and even study dynamics in the case of NMR. However, their use is limited by the fact that protein samples may not form a perfectly ordered 3D crystal for X-ray crystallography or some samples are too large to obtain an easily interpretable spectra for NMR. To determine protein structures that are not amenable to study by X-ray crystallography and NMR, the use of single-particle EM has risen to prominence.

Single-particle EM is particularly suited to studying large macromolecular assemblies on the order of >300 kDa in size<sup>102</sup>. To perform these studies, a small sample of pure protein is applied to a carbon-coated copper grid and the sample can then either be stained with heavy metal salts or vitrified prior to visualization by a TEM. After acquiring a large number of images and selecting individual “particles”, specialized image processing software is then used to calculate the three-dimensional (3D) reconstruction of the complex. Single-particle EM has several advantages for studying large-macromolecular assemblies. As many macromolecular assemblies require flexibility in certain domains to perform a function, single-particle EM is advantageous in that these dynamics can be visualized and modeled<sup>104</sup>. These dynamic features are typically absent in a static X-ray crystal structure. Furthermore, despite EM structures having lower resolutions, usually on the scale of 15-30 Å, the electron density map can be used as a molecular envelope to fit high-resolution crystal or NMR structures to generate “pseudo-atomic” models of a protein complex<sup>104,105</sup>. Excitingly, recent advances in electron microscopy equipment and image processing algorithms have drastically improved the practical resolution from

single-particle EM studies, and this is highlighted by the recent high-resolution models of the ribosome (6.5 Å) and proteasome (7.4 Å).

## 1.7 Thesis Overview

Despite extensive work to functionally characterize the Atg1 kinase complex, there is a lack in understanding the structural aspects of complex formation and function. Therefore, we were interested in determining the molecular structure of the Atg1 kinase complex. What was evident from the literature was the observed stability of the Atg17-Atg31-Atg29 complex, which has been purified by recombinant methods. Thus as an early first step in deciphering Atg1 kinase complex formation, we sought to determine the structure of the Atg17-Atg31-Atg29 complex.

To study the Atg17-Atg31-Atg29 complex, we employed the technique of single-particle electron microscopy. This established method has been previously used to study the structures of large dynamic macromolecular complexes and thus was a logical choice for this study. To perform these experiments, I established a purification protocol to obtain adequate amounts of protein for EM studies. The use of covalent fusion labels was used to localize the different subunits within the larger structure. Finally, conformational dynamics of the complex was assessed by measurements of particle dimensions.

During the process of this study a crystal structure of the *Lachancea thermotolerans* Atg17-Atg31-Atg29 was determined by X-ray crystallography<sup>92</sup>. These results provided evidence, which supported our studies, but also shifted our work towards structurally characterizing the Atg1 kinase complex by single-particle EM. As such, a new purification scheme was established to recombinantly express and purify a five-component “pentamer” assembly of the Atg1 kinase complex. EM analysis was used to study this pentameric assembly and further delineate Atg1 kinase complex formation.

In some preliminary work, the interacting protein scaffold Atg11, was purified using a novel yeast expression system. As an interacting partner of the Atg1 kinase complex, this was a logical extension to this project. The structure of Atg11 was further characterized by single-particle EM.

## Chapter 2: Materials and Methods

### 2.1 Purification in *S. cerevisiae*

#### 2.1.1 TAP tagging of Atg29 and Atg31 in yeast

The protease-deficient yeast strain BJ2168 (*MATa leu2 trp1 ura3 pep4-3 prb1-1122 prc1-407*) was used as a background strain for all endogenous tagging experiments. Atg29 and Atg31 were endogenously C-terminal tagged at their native locus with a tandem affinity purification (TAP) tag<sup>108</sup>. The TAP tag was amplified by polymerase chain reaction, from the plasmid pBS1539, with homologous regions to the endogenous gene. 3 µg of PCR product was transformed into yeast by the lithium acetate method<sup>109</sup>. Transformed yeast was grown on synthetic dropout media without uracil for two days at 30°C. and colonies were screened by colony PCR amplification of the tagged locus. Endogenous expression of the tagged subunit was confirmed by western blot of whole cell lysate using anti-TAP antibody (Thermo, CAB1001).

#### 2.1.2 TAP purification

TAP tagged Atg17, Atg31 and Atg29 were purified by the TAP purification method<sup>108</sup>. Atg31-TAP and Atg29-TAP were developed in house (See above section), Atg17-TAP strain was provided as a gift by Dr. Daniel J. Klionsky (University of Michigan). Yeast cells were grown to an OD<sub>600</sub> of ~2.5 and frozen at -80°C for storage. Approximately 15 – 20 grams of cells were resuspended in lysis buffer (100 mM HEPES pH 8, 250 mM KCl, 2 mM EDTA, 1 mM EGTA, 5% glycerol, 1% CHAPS, 2.5 mM DTT, 2 mM PMSF, 0.1 mM sodium vanadate, 2mM benzamidine, 50 mM NaF) containing EDTA-free protease inhibitor (Roche, 11873580001) and lysed by bead beating. The lysate was clarified by centrifugation at ~30,000 xg for 30 min, and the supernatant fraction was incubated with Immunoglobulin G (IgG) sepharose (GE Healthcare, 17-0969-01) for 1 h at 4°C. The resin was washed with buffer (50 mM Tris-HCl pH 8.0, 100 mM NaCl, 5% glycerol, 0.1% CHAPS, 0.5 mM DTT) and bound proteins were eluted by Tobacco etch virus (TEV) protease (Life Technologies, 12575-015) cleavage for 1.5 h at 16°C. The

elution was concentrated using an Amicon Ultra 10K centrifugation unit (Millipore, UFC901008) and loaded onto a Superose 6 column equilibrated with buffer (50 mM Tris-HCl pH 8.0, 100 mM NaCl, 5% glycerol, 0.1% CHAPS) and connected to an ÄKTAprime plus (GE Healthcare, 11-0013-13). Purified complexes were trichloroacetic acid (TCA)-precipitated for SDS-PAGE analysis or examined by EM.

## **2.2 Cloning and construction of co-expression vectors for recombinant protein expression**

A significant amount of cloning was required to produce the various constructs used in this study. In total, three different cloning methods were used; restriction enzyme cloning, restriction-free cloning (RF-cloning) and ligation independent cloning (LIC), which will be covered in more detail in the following text. A summary of the primers used for cloning and sequencing can be found in Appendix A.1 while all plasmids/vectors used can be found in Appendix A.2. All putative clones were confirmed by DNA sequencing (Genewiz, South Plainfield, NJ).

### **2.2.1 Cloning Atg genes for recombinant expression of Atg17-Atg31-Atg29 using the pET-Duet system**

The coding regions of Atg17 (SGD YLR423C), Atg31 (SGD YDR022C), and Atg29 (SGD YPL166W) were amplified by PCR from purified genomic DNA isolated from the yeast background strain BY4741 (*MATa his3Δ0 leu2Δ0 met15Δ0 ura3Δ0*). The genes were cloned by restriction enzyme cloning at the indicated sites (see Appendix A.1 and A.2). Atg17 was cloned into the pET28b-HMT<sup>110</sup> and pGEX-6P-1 vector (GE Healthcare, 28-9546-48). Atg31 and Atg29 were cloned into the two multiple cloning sites of pET-Duet1 and pCOLA-Duet1 (Novagen, 71406-3). More specifically, Atg31 was cloned into the first multiple cloning site, followed by sequential cloning of Atg29 into the second available multiple cloning site. These created the following vectors; pET28bHMT:Atg17 (pLC001), pGEX-6p-1: Atg17 (pLC002), pET-Duet1:6xHis-Atg31/Atg29 (pLC003) and pColA-Duet1:6xHisAtg31/Atg29 (pLC004). The phosphomimetic mutant Atg29 vector was created in a similar manner as the Atg31/Atg29 containing vectors except the Atg29 sequence was amplified from a vector provided by our collaborator (Dr. Daniel J. Klionsky, University of Michigan), that contained both the Atg29[3SD] and

Atg29[20STA/3SD] phosphomimetic forms. Cloning these mutants into pET-Duet1 created the vectors, pET-Duet1:Atg31-6xHis/Atg29[3SD] (pLC006) and pET-Duet1:Atg31-6xHis/Atg29[20STA/3SD] (pLC007).

### **2.2.2 Construction of GFP-fusion label vectors for GFP labelling of Atg31 and Atg29**

Green fluorescent protein (GFP) labelling vectors were constructed by cloning the GFP sequence into both multiple cloning sites of the pETDuet1 vector. GFP was amplified from a GFP containing plasmid<sup>111</sup> by PCR. Amplified product was then introduced into the pET-Duet1 vector by restriction enzyme cloning. The primers used for amplifying GFP are listed in Appendix A.1.

To C-terminal GFP label Atg31 and Atg29 a stop codon was removed to allow expression of the GFP tag. Two additional primers were used to amplify a stop codonless Atg31 and Atg29 gene sequence (see Appendix A.1). Atg31 and Atg29 constructs were then cloned into the C-terminal GFP vectors by restriction enzyme cloning. This created the vectors pGFP-C1:6xHis-Atg31GFP/Atg29 (pLC004) and pGFP-C2:6xHis-Atg31/Atg29GFP (pLC005).

### **2.2.3 Cloning Atg genes for recombinant expression using the pQLINK system**

We used the pQLINK system<sup>112</sup> to co-express a five component Atg1 pentamer complex. The pQLINK system consists of a novel “LINKing” sequence that uses a LIC method to join a vector fragment and an insert fragment. Three vectors are commercially available, the pQLINK-H, a N-terminal His-tag version, pQLINK-G, a N-terminal GST-tag version and pQLINK-N, a tagless vector. To produce a co-expression plasmid, we used restriction enzyme cloning to clone the genes for Atg17, Atg31-6xHis, and Atg1 CTD (SGD YGL180W) into the pQLINK-N vector. Atg29 and various Atg13 (SGD YPR185W) constructs (MD, CTD, FL) were cloned into pQLINK-N using a restriction-free (RF) cloning method<sup>113</sup> as these genes contained internal restriction site. These cloned genes were then fused together in a single vector using the novel LINK sequences.

To perform the linking step, acceptor pQLINK plasmid was digested with 10 units of SmaI (NEB, R0604S) at 25°C causing linearization of the vector. Donor pQLINK plasmid was digested with 10 units

of PacI (NEB, R0547S) at 37°C to excise the insert gene sequence to be linked. The linearized fragments were then treated with 1.5 units of T4 DNA polymerase (ThermoFisher, EP0061) in reaction buffer supplemented with 100 mM DTT and either 25 mM dCTP (for PacI treated inserts) or 25 mM dGTP (for SmaI treated vector). The two components were annealed at room temperature followed by transformation in DH5-*alpha* *E. coli*. These linking steps were performed sequentially until both the Atg17-Atg31-Atg29 complex and the five component pentamer were cloned into a single vector to produce:

pQLINK-N: Atg17/Atg29/Atg31 (pLC008)  
pQLINK-N: Atg17/Atg29/Atg31-6xHis/Atg1 CTD/Atg13 MD (pLC009)  
pQLINK-N: Atg17/Atg29/Atg31-6xHis/Atg1 CTD/Atg13 CTD (pLC010)  
pQLINK-N: Atg17/Atg29/Atg31-6xHis/Atg1 CTD/Atg13 FL (pLC011)

Additionally, we developed a His-tagged maltose binding protein (MBP) label pQLINK vector dubbed pQLINK-HMP that was used to clone His-MBP labelled Atg1 CTD and Atg13 CTD. These vectors were used to construct:

pQLINK-N: Atg17/Atg29/Atg31-6xHis/MBP-Atg1 CTD/Atg13 CTD (pLC012)  
pQLINK-N: Atg17/Atg29/Atg31-6xHis/Atg1 CTD/MBPAtg13 CTD (pLC013)

All vectors were subsequently used for co-expression of the pentamer assembly in *E. coli*.

### 2.2.6 Cloning of Atg11 into the pESC yeast expression system

The pESC series of vectors are a galactose-inducible expression system for use in *S. cerevisiae* cells. Each of the vector contains two multiple cloning sites suitable for co-expression of a maximum of two proteins. More proteins can be expressed in a single system through the use of vectors with different auxotrophic markers. In total, four vectors containing histidine, leucine, tryptophan or uracil (Ura) selectable markers are available. The multiple cloning sites use conventional restriction digestion cloning to insert the gene(s) of interest. However, Atg11 contains many cut sites that were not compatible with the pESC system. Therefore, to clone Atg11 into the pESC vector, we used RF-cloning<sup>113</sup>. Atg11 (SGD YPR049C) was amplified by PCR using primers containing compatible ends to the pESC-Ura vector. Subsequently, the PCR product was used as primers for amplification of the pESC-Ura vector along with insertion of Atg11. This cloning produced the vector pESC-Ura:Atg11 (pLC014).

## 2.3 Recombinant expression and purification

To facilitate EM studies purification of adequate amount of homogenous protein was essential. All of the following described proteins were expressed in the background *E. coli* strain BL21\* or BL21\* Rosetta. Several purification strategies were used but generally consisted of a single or two step affinity chromatography step followed by separation of bound complex by either gel filtration or glycerol gradient centrifugation. All SDS-PAGE gels were 12%, unless otherwise stated, and were visualized by either Coomassie Brilliant Blue or silver staining. Molecular weight markers used were Precision Plus Protein Ladder (BioRad).

### 2.3.1 Purification of recombinant Atg17-Atg31-Atg29

To purify recombinant Atg17-Atg31-Atg29, His-MBP-tagged Atg17 (pLC001) was co-expressed with 6xHis-Atg31 and Atg29 (pLC003) in *E. coli* BL21 Star TM (DE3) (Life Technologies, C6010-03). To express the complex, transformed BL21\* *E. coli* was grown at 37°C until an OD<sub>600</sub> = 0.6 and were induced using 0.25 mM Isopropyl β-D-1-thiogalactopyranoside (IPTG) at 16°C for 18 hours. 15-20 grams of cells were resuspended in lysis buffer (150 mM NaCl, 50 mM Tris-HCl pH 8.0, 1 mM PMSF) and lysed by sonication. The lysate was clarified by centrifugation at ~30,000 xg for 30 min, and the supernatant was incubated with HisPur nickel-NTA resin (Pierce, 88221) for 1 hour at 4°C followed by washes with buffer (150 mM NaCl, 50 mM Tris-HCl) and imidazole elution (150 mM NaCl, 50 mM Tris-HCl, 250 mM Imidazole). Ni<sup>2+</sup> elutions were then incubated with amylose resin (New England Biolabs, E8021S) for 1 hour at 4°C followed by elution with amylose elution buffer (150 mM NaCl, 50 mM Tris-HCl, 10 mM Maltose) We then removed the His-MBP tag by TEV protease cleavage for 18 hours at 4°C in dialysis buffer (150 mM NaCl, 50 mM Tris-HCl, 0.5 mM EDTA, 1 mM DTT). The cleaved complex was then concentrated in an Amicon 10K cutoff concentrator (Millipore, UFC801024) then separated by gel filtration chromatography using a Superose 6 column connected attached to an ÄKTAprime plus. The peak fraction was then analysis by SDS-PAGE or used for EM analysis.

We used the same procedure for purifying His-MBP-tagged Atg17-Atg31-Atg29 and His-MBP-tagged Atg17, except that the TEV cleavage step was eliminated. Amylose elution fractions were concentrated in an Amicon 10K cutoff concentrator (Millipore, UFC801024) then separated by gel filtration chromatography on a Superose 6 column attached to an ÄKTAprime plus.

For expression of complexes containing GFP-tagged Atg29 or Atg31, we expressed GST-Atg17 (pLC002) with either 6xHisAtg31GFP/Atg29 (pLC004) or 6xHisAtg31/Atg29GFP (pLC005) in BL21\* *E. coli*. The complexes were induced to express at 30°C for 5 hours. 15-20 grams of cells were resuspended in buffer (150 mM NaCl, 50 mM Tris-HCl pH8.0) and lysed by sonication. Cell lysate was incubated with glutathione agarose (Pierce, 16100) for 1 hour at 4°C and eluted in glutathione elution buffer (150 mM NaCl, 50 mM Tris-HCl, 10 mM reduced glutathione). The GST-tag was removed by PreScission protease (GE Healthcare, 27-0843-01) incubation for 18 hours at 4°C. The cleaved complex was then concentrated in an Amicon 10K cutoff concentrator (Millipore, UFC801024) and then separated by gel filtration chromatography on a Superose 6 column attached to an ÄKTAprime plus. The peak fractions were then analysed by SDS-PAGE or used for EM analysis.

### **2.3.2 Purification of recombinant Atg1 kinase pentamer complex**

The pentamer complex was expressed using a single plasmid constructed using the pQLINK system. In total, five purifications of the various pentamer assemblies were conducted and follow the same general procedure. Atg31 was C-terminal 6xHistidine tagged to facilitate the purification procedure. To initially assess stability of the complex with various Atg13 constructs, pLC009, pLC010 and pLC011 were expressed in BL21\* Rosetta *E. coli*. These complexes were expressed at 37°C until an  $OD_{600} = 0.6$  and induced at 37°C for 3-4 hours. 1-3 grams of cells were resuspended in lysis buffer (150 mM NaCl, 50 mM HEPES pH 8.0, 1 mM PMSF) and lysed by sonication. The lysate was clarified by centrifugation at  $\sim 30,000 \times g$  for 30 min, and the supernatant was incubated with HisPur nickel-NTA resin (Pierce, 88221) for 0.5 hours at 4°C followed by washes with buffer (150 mM NaCl, 50 mM HEPES pH 8.0) and imidazole elution (150 mM NaCl, 50 mM HEPES pH 8.0, 100 mM Imidazole). The  $Ni^{2+}$  elutions were

analyzed by SDS-PAGE and it was decided that Atg13 CTD containing complexes would be purified on a larger scale.

For large-scale purification, approximately 15-20 grams were used. The complex was purified using the same protocol previously mentioned. The nickel-sepharose elutions were concentrated in an Amicon 10K cutoff concentrator (Millipore, UFC801024), and separated by gel filtration chromatography on a Superose 6 column connected to an ÄKTAprime plus. The peak fractions were then analysed by SDS-PAGE and used for negative-stain EM.

### **2.3.3 GraFix protocol**

The GraFix protocol was adapted from the method by Kastner et al.<sup>114</sup> This modification uses a glycerol gradient in combination with glutaraldehyde to improve complex stability in preparation for analysis by negative-stain EM. In our method we studied the pentamer assembly by applying GraFix after purification by affinity and gel filtration chromatography. In particular, the peak fractions from gel filtration on a Superose 6 column were pooled and concentrated using an Amicon 10K cutoff concentrator (Millipore, UFC801024). The protein sample was then overlaid on a linear 12-24% glycerol gradient (150 mM NaCl, 50 mM HEPES pH 8.0, 12% or 24% glycerol) either with/or without 0.05% glutaraldehyde made using the Gradient Station (Biocomp Instruments). The gradients were centrifuged at 40,000 rpm for 16 hours at 4°C. The gradients were then fractionated using the Gradient station and samples were analyzed by SDS-PAGE and used for negative-stain EM.

### **2.3.3 Expression and purification of Atg11 using the pESC yeast expression system**

Approximately 1 µg of pESC-Ura:Atg11 (pLC0014) plasmid was transformed into the BJ2168 yeast strain (*MATa leu2 trp1 ura3 pep4-3 prb1-1122 prc1-407*) by the lithium acetate method<sup>109</sup>. Transformed yeast were selected on synthetic drop-out media without uracil (SD-Ura) for two days at 30°C. Putative colonies were screened by colony PCR. For expression, Atg11 starter cultures were grown at 30°C on SD-Ura media with 2% raffinose as the sole carbon source. These cells were grown to an OD<sub>600</sub> = 1.0 and were induced by adding solid powder of 2% peptone, 1% yeast extract and 2% galactose.

Cells were induced at 30°C for 16-18 hours. Endogenous expression of the tagged subunit was confirmed by Western blot of whole cell lysate using anti-FLAG antibody (Sigma).

Approximately 10-20 grams of cells were resuspended in lysis buffer (250 mM NaCl, 100 mM Tris-HCl pH 8.0, 5% Glycerol, 0.1% Triton X-100, 2 mM PMSF, 0.1 mM sodium vanadate, 2mM benzamide, 50 mM NaF) containing EDTA-free protease inhibitor (Roche, 11873580001) and lysed by bead beating. The lysate was clarified by centrifugation at ~30,000 xg for 30 min, and the supernatant fraction was incubated with M2 FLAG-sepharose (Sigma-Aldrich, A2220) for 2 hours at 4°C. The resin was washed with buffer A (250 mM NaCl, 100 mM Tris-HCl pH 8.0, 5% Glycerol, 0.1% Triton X-100) followed by buffer B (150 mM NaCl, 100 mM Tris-HCl pH 8.0, 5% Glycerol, 0.1% Triton X-100) and eluted using 0.5 mg/ml FLAG peptide in buffer B. The elution was concentrated using an Amicon Ultra 10K centrifugation unit (Millipore, UFC901008) and was further separated by gel filtration chromatography on a Superose 6 column connected to an ÄKTAprime plus. The peak fraction was analyzed by SDS-PAGE and used for negative-stain EM.

## **2.4 Electron microscopy**

Protein specimens were subject to negative-stain treatment prior to EM analysis<sup>115</sup>. Copper grids were prepared by carbon coating with a 208C High Vacuum Turbo Carbon Coater (Cressington). Carbon coated grids were hydrophilized with an easiGlow Glow Discharge unit (PELCO). Purified protein sample were annealed to the glow discharged grids and then stained with 0.75% (w/v) uranyl formate. Negatively-stained specimens were left to air dry prior to imaging. Raw images were recorded at a nominal magnification of 49,000X on a 4K x 4K Eagle charge-coupled device (CCD) camera (FEI) with a Tecnai Spirit transmission electron microscope (FEI) operated at an accelerating voltage of 120 kV. Images for 2D analysis were collected using the same instrument with the same operating parameters and at a defocus value of -1.2  $\mu\text{m}$ . For tilt-pair data collection, the same specimen areas were recorded at tilt angles of 55° and untilted under low-dose conditions at a nominal magnification of 49,000 and a defocus

value of  $-1.2 \mu\text{m}$  on the 4K X 4K Eagle CCD camera. For image processing,  $2 \times 2$  pixels were averaged to yield a pixel size of approximately  $4.6 \text{ \AA}$  at the specimen level.

## 2.5 Image processing

For two-dimensional (2D) analysis, particles for each dataset were interactively selected using Boxer<sup>116</sup> and windowed into a specified box pixel image. These selected particles were then translationally aligned, and subjected to ten cycles of multi-reference alignment using SPIDER<sup>117</sup>. Each round of alignment was followed by K-means classification specifying either 20, 50 or 100 classes. The particle number and box sizes used for image processing of each data set are summarized in Table 2.1.

**Table 2.1 Summary of processing parameters for data set**

Data Set	Particle Number	Box Size (Pixels)	Number of Classes
Atg17-Atg31-Atg29	10,251	112	20
MBP-Atg17-Atg31-Atg29	8,209	140	50
Atg17-Atg31GFP-Atg29	1,991	120	50
Atg17-Atg31-Atg29GFP	2,290	120	50
MBP-Atg17	5,922	140	100
Atg17-Atg31-Atg29[3SD]	4,671	112	50
Atg17-Atg31-Atg29[20STA3SD]	6,588	112	50
Atg17-Atg31-Atg29+GraFix	1,968	112	50
Atg17-Atg31-Atg29-Atg1 CTD-Atg13 CTD	3,700	120	50
Atg17-Atg31-Atg29-Atg1 CTD-Atg13 CTD + GraFix	2,787	120	50
Atg17-Atg31-Atg29-MBPAtg1 CTD-Atg13 CTD + GraFix	1,471	132	100
Atg17-Atg31-Atg29-Atg1 CTD-MBPAtg13 CTD + GraFix	1,702	132	100
Atg11	2,636	100	100

For three-dimensional (3D) reconstruction, particle pairs were interactively selected from both the untilted and  $55^\circ$  tilted images using WEB<sup>117</sup>. The selected particles were windowed into a specified box pixel image, and the particles from the untilted specimens were classified into 20 classes. 3D reconstruction was calculated for the largest class from the tilted specimens using the backprojection and

angular refinement procedures in SPIDER. The final resolution of the structure was estimated by the Fourier shell correlation (FSC) function of 0.5. Docking of crystal structures was performed by UCSF Chimera<sup>118</sup>.

## 2.6 Length and curvature analysis

Measurements of particles were performed on CorelDRAW5. Only class averages containing two visible MBP-labels were selected for analysis. 17 class averages for His-MBP-Atg17-Atg31-Atg29 and 18 class averages for His-MBP-Atg17 met these criteria. The length of each particle was measured as the junction-to-junction length beginning at the boundary of the MBP-Atg17 linker and ending at the next MBP-Atg17 linker boundary. Measurements of the cord length and height for each arc of a monomer of Atg17 were measured separately. The cord-length of an arc was determined to begin at the junction of the MBP-linker-Atg17 and end at the center of the Atg17 dimer, while the height was measured at the edge of the arc apex to the arc chord. Curvature was calculated using the derived arc radius formula;

$radius = \frac{H}{2} + \frac{W^2}{8H}$ , where H is the arc height and W is the cord length. The ratio of the radius was calculated by dividing one arc radius by the second arc radius in the same dimer.

## 2.7 Bioinformatics

Sequences were obtained either from the Saccharomyces Genome Database ([www.yeastgenome.org](http://www.yeastgenome.org))<sup>119</sup> or UniProt ([www.uniprot.org](http://www.uniprot.org))<sup>120</sup>. Sequence alignment was performed using ClustalW2 ([www.ebi.ac.uk/Tools/msa/clustalw2](http://www.ebi.ac.uk/Tools/msa/clustalw2))<sup>121,122</sup>. Coiled-coil prediction was performed with the coiled-coil prediction server ([http://embnet.vital-it.ch/software/COILS\\_form.html](http://embnet.vital-it.ch/software/COILS_form.html))<sup>123</sup>. Identification of IDPs was performed using the IUPRED server ([upred.enzim.hu](http://upred.enzim.hu))<sup>124,125</sup>

## 2.8 Construction of figures

Paint.NET was used to perform image contrast manipulation while InkScape was used to render and organize all figures.

## Chapter 3. Results

### 3.1 Analysis of *in vivo* purification of TAP tagged Atg17-Atg31-Atg29 ternary subcomplex

As an initial step to purify the Atg17-Atg31-Atg29 complex, we attempted to isolate the native complex from *S. cerevisiae* using the tandem affinity purification (TAP) method<sup>108</sup>. Endogenous C-terminal TAP-tagged Atg17, Atg31 and Atg29 were purified by incubating yeast cell lysate with IgG sepharose followed by TEV protease cleavage. The only purification to exhibit bands corresponding to Atg17, Atg31 and Atg29 was that of Atg29-TAP (compare Figure 3.1 A with Appendix B.1). The protein complex was further purified by gel filtration chromatography, which eluted at a size corresponding to a 600-kDa protein on a Superose 6 column. This fraction was analyzed by 12% SDS-PAGE which confirmed the appearance of several bands which corresponded to the correct molecular weights for Atg17, Atg31 and Atg29 (Figure 3.1A). The identities of the proteins in these fractions were analyzed by mass spectrometry that further confirmed these fractions were enriched for the ternary complex (see Appendix B.2).

The peak gel-filtration fractions were visualized by negative stain electron microscopy. Preliminary EM analysis provided a first glimpse into what the believed Atg17-Atg31-Atg29 complex looked like (Figure 3.1B). Observed particles adopted an elongated shape analogous to the letter “S.” However, despite these promising results, the particle yield was relatively low with few particles (<3) being observed per image. This low yield made it difficult to analyze the data in an effective manner and thus we sought an improved purification scheme to isolate the Atg17-Atg31-Atg29 complex.

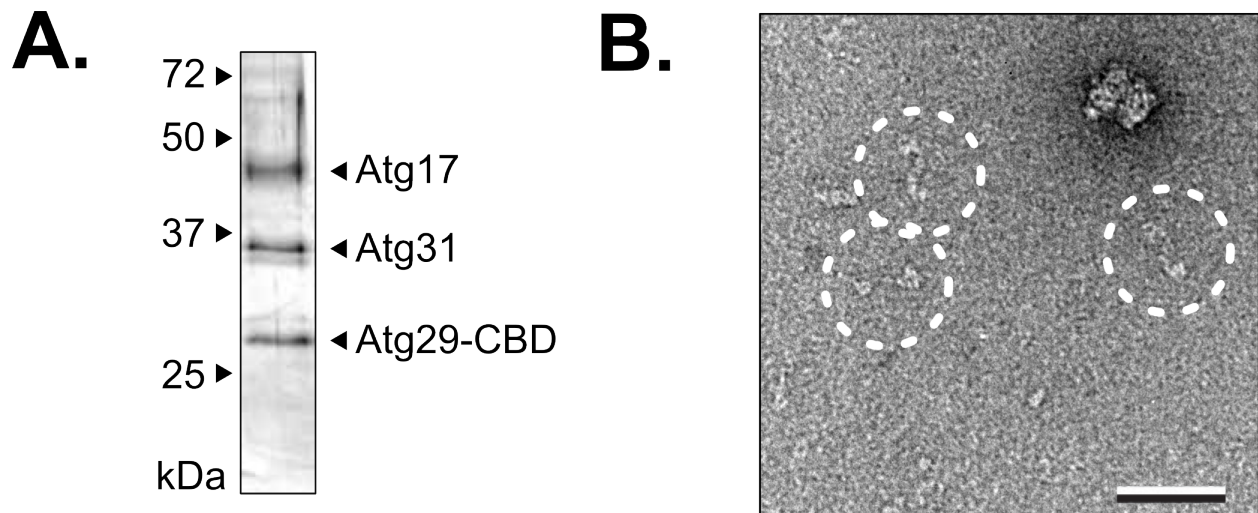


**Figure 3.1 Purification and negative stain EM analysis of native Atg29-TAP tagged complex.** (A) Analysis of native Atg17-Atg31-Atg29 complex purified from *S. cerevisiae* by silver-stained 12% SDS-PAGE. Estimated sizes for the Atg proteins are labelled. (B) Representative raw image of negative-stained native Atg17-Atg31-Atg29-CBD. Particles are dotted in circles (scale bar = 50nm).

### **3.2 Recombinant purification of the Atg17-Atg31-Atg29 ternary subcomplex**

Previous studies have shown that the Atg17-Atg31-Atg29 complex could be recombinantly overexpressed and purified from *E. coli*<sup>88</sup>. To improve upon our purification the ternary complex was reconstituted in an *E. coli* expression system. We co-expressed N-terminal hexahistidine-MBP-tagged Atg17, cloned into the pET28b-HMT vector, with N-terminal hexahistidine-tagged Atg31 and untagged Atg29, both cloned into a pET-Duet1 vector. This two vector system was expressed in BL21\* *E. coli* followed by two-step nickel-sepharose and amylose-sepharose affinity chromatography followed by cleavage of the His-MBP tag using TEV protease. The complex was separated by gel-filtration chromatography and the peak fraction was analyzed by 12% SDS-PAGE (Figure 3.2A). Similar to the native purification, several bands were observed that were believed to correspond to Atg17, Atg31 and Atg29 in stoichiometric quantities (Figure 3.2A). When these fractions were examined by negative stain EM, we observed morphologies similar to what was observed from the native purification (Figure 3.2B).

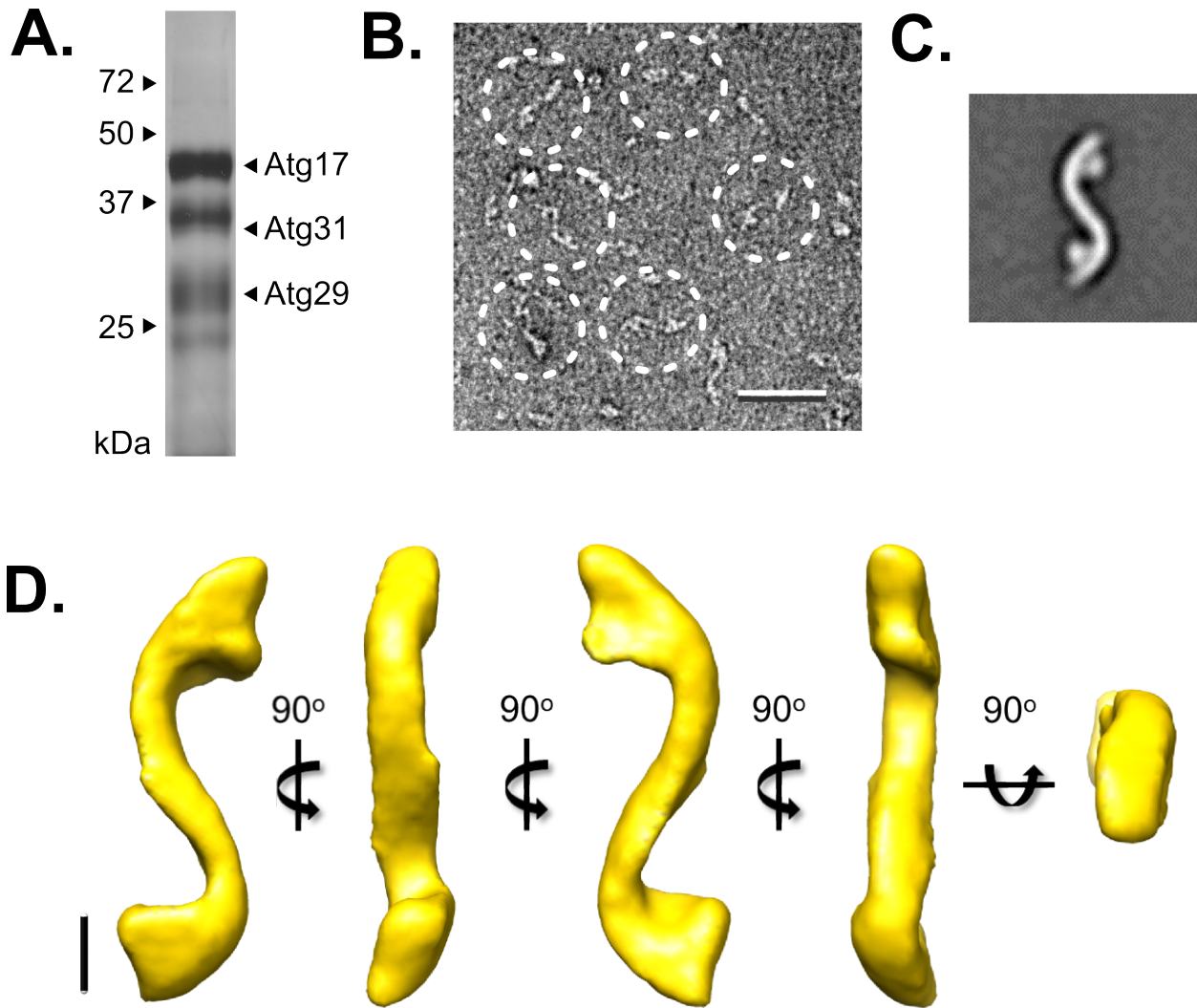


**Figure 3.2** *In vitro* purification and negative stain EM analysis of recombinant Atg17-Atg31-Atg29. (A) Native Atg17-6xHis-Atg31-Atg29 complex analyzed by Silver-stained 12% SDS-PAGE. Estimated size for the Atg proteins are labelled. (B) Representative raw image of negative-stained Atg17-Atg31-Atg29. Particles are dotted in circles (scale bar = 50 nm). (C) Class average analysis of 10,251 negatively stained particles. Major representative class, from ~1000 particles, is shown and exhibits a S-shape architecture with two-circular shaped domains attached to the terminal regions of the complex. (D) The 3D reconstruction of Atg17-Atg31-Atg29 viewed in several orientations (scale bar = 5 nm)

### 3.3 Electron microscopy analysis of the recombinant Atg17-Atg31-Atg29 ternary subcomplex

We conducted two-dimensional (2D) class average analysis of the ternary complex. The negative-stain procedure caused the Atg17-Atg31-Atg29 complex to preferentially orient itself on the carbon support layer, which aided in the analysis to produce an “average” view of the particle and greatly increases the signal-to-noise ratio. From a total of 10,251 particles from negative-stained images picked using WEB, the particles were classified into 20 classes using SPIDER<sup>117</sup>. The most dominant class average shows that the Atg17-Atg31-Atg29 ternary complex forms an extended S-shape architecture (Figure 3.2C). The overall shape appeared to contain a central scaffold making up most of the density of the “S,” while two globular densities were localized at the concave side of the arc. The ternary complex was elongated with an end-to-end distance of 345 Å. Its structure further hinted at a dimeric assembly due to the two-fold symmetry observed which agreed with previous biochemical findings<sup>88</sup>.

To gain even further structural insight, we conducted a 3D reconstruction of the complex by applying the random conical tilt approach to our dataset. By collecting pairs of images at an untilted and 55° tilt angle, angular information was obtained which SPIDER could use to produce a 3D structure. Overall, the 3D reconstruction showed two arcs joined by a central tube region (Figure 3.2D). Each arc had a radius of curvature of approximately 90 Å with each arc orienting in an opposite directions to produce the S-shape. Near the terminal regions of the arcs was the previously observed globular density. This reconstruction exhibited a 37 Å resolution (Fourier shell correlation = 0.5 criterion) with a tube diameter of 35 Å. These models provided a foundation to further understand the overall subunit organization. However, due to the low resolution of the electron density map, an alternative approach was required to delineate the subunit organization of this complex.

### 3.4 Subunit localization of Atg17, Atg31 and Atg29 using GFP and MBP fusion labels.

To determine the subunit organization and interaction interfaces of the Atg17-Atg31-Atg29 complex, a covalent fusion label approach was used. A large protein label is used to tag a subunit of interest, followed by the purification of the tagged complex, and analysis by 2D negative stain EM. Comparison of the labelled complex versus the unlabelled complex would reveal the location of the terminus of that subunit. This approach has been used successfully in previously studied protein complexes. For this study, a GFP<sup>111,126,127</sup> or MBP<sup>128,129</sup> tag was fused to the terminus of Atg17, Atg31 or Atg29.

As the purification of this complex involved expressing an N-terminal labeled His-MBP-Atg17, a logical first step was to examine the MBP-labeled Atg17 complex. The complex was purified without the MBP label. A dataset of 8,209 particles from negative-stained images was classified into 50 classes. The most dominant classes that emerged exhibited the same elongated S-shape structure with two additional globular densities localized to the tips of the S-shape (Figure 3.3A). From a subtracted difference image of untagged Atg17-Atg31-Atg29 from tagged His-MBP-Atg17-Atg31-Atg29, two additional terminal densities were clearly observed, supporting a dimeric assembly.

To facilitate labelling of Atg31 and Atg29, the pET-Duet1 vector was reengineered by incorporating an enhanced GFP (eGFP) sequence into the multiple cloning sites in the C-terminal positions. The pET-Duet-GFP (pGFPC1 and pGFPC2) vectors were used to express GFP-labelled Atg31 or Atg29. C-terminal GFP labelled Atg29-GFP and Atg31-GFP complexes were separately purified and subject to analysis by 2D negative stain EM. From the class averages, a single additional density were observed to localize to the convex side of the arc opposite to the globular densities in both Atg29-GFP and Atg31-GFP complexes (Figure 3.3B and C). The reason why only a single density was observed could be explained by flexibility either within the GFP moiety or linker (~ 12 amino acids in length) or through dynamics in the tagged subunit. The instability of GFP as a tag has been observed previously<sup>126</sup>. Nevertheless, In comparison to the untagged complex, a difference density overlay confirmed the observed GFP density. Together, these results further provide a model whereby Atg17 forms the major

backbone of the scaffold while Atg31-Atg29 are likely appended to the terminal globular regions. To further probe the structural role Atg17 has within the complex, analysis of the Atg17 dimer was conducted.

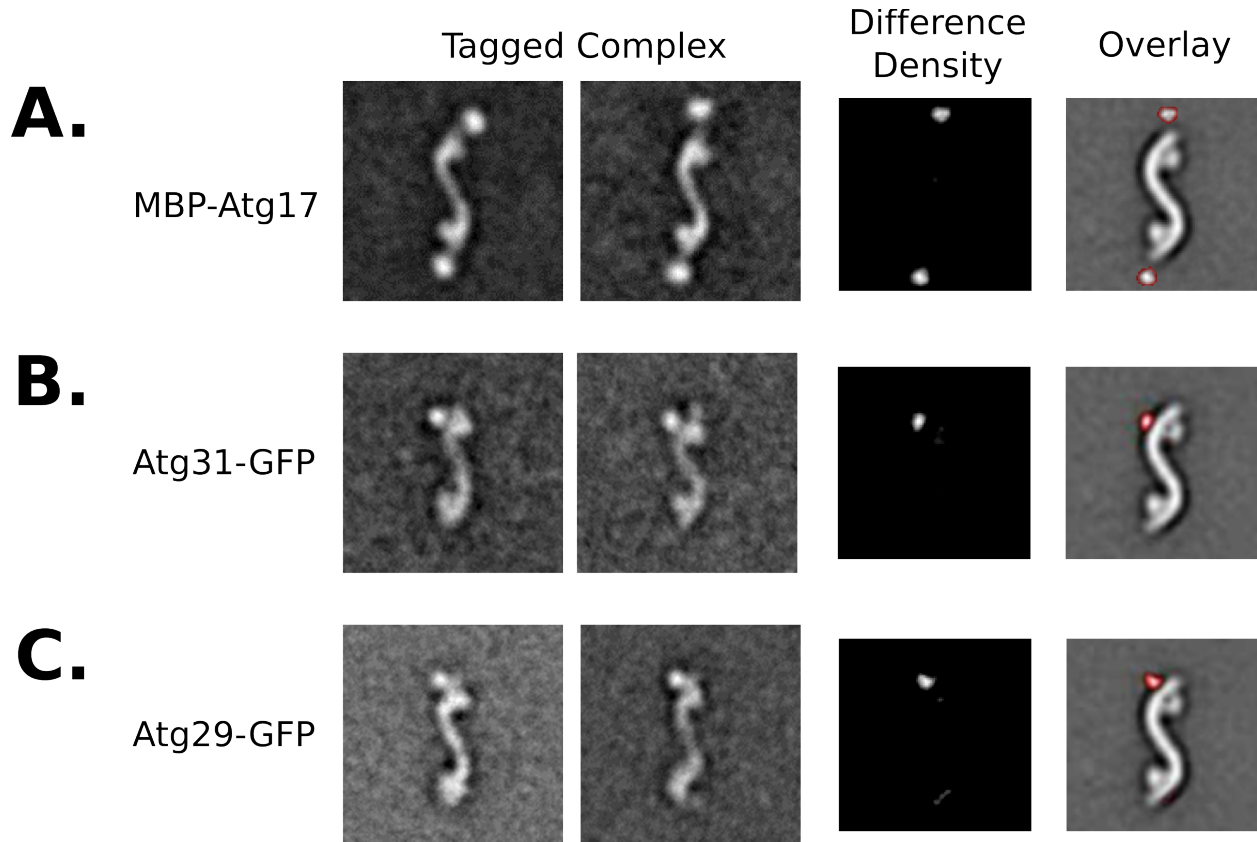


**Figure 3.3 Mapping of Atg17-Atg31-Atg29 complex subunits.** Tagged complexes (left panels) are representative class averages of negatively-stained samples. Difference density (middle panel) is a difference image generated from subtracting the untagged Atg17-Atg31-Atg29 average from the tagged complex average. The overlay (right panel) is the overlay of the difference density map and untagged Atg17-Atg31-Atg29 indicating the location of the tag (red). (A) Localization of Atg17 with MBP-Atg17 obtained from 8,209 particles in 50 classes. Side length = 59nm (B) Localization of Atg31 with Atg31-GFP obtained from 1,991 particles in 50 classes. (C) Localization of Atg29 with Atg29-GFP from 2,290 particles in 50 classes.

### **3.5 Atg17 mediates dimerization and forms the central scaffold of the complex.**

From the localization analysis it was proposed that Atg17, the largest protein in this complex, likely mediates dimerization. To test this hypothesis, His-MBP-Atg17 was expressed and purified by two-step nickel-sepharose and amylose-sepharose affinity chromatography followed by gel filtration on a Superose 6 column. The globular MBP tag was left on Atg17 to aid in visualizing the particles, as Atg17 on its own would have less contrast and have been difficult to image. MBP-Atg17 was purified to homogeneity and was further visualized by negative-stain EM and analyzed by 2D class average analysis (Figure 3.4A). A total of 5,922 particles were classified into 100 classes. The most dominant classes showed that Atg17 does indeed account for most of the density in the Atg17-Atg31-Atg29 complex and more than likely forms the central S-shape scaffold (Figure 9B). This result was further confirmed by analyzing the difference density map between Atg17 versus the Atg17-Atg31-Atg29 complex (Figure 3.4B). From these results, it is clear that globular densities are composed of Atg31 and Atg29. Another interesting feature from the 2D analysis was that Atg17 is capable of adopting several distinct conformations (Figure 3.4C). Atg17 was observed to adopt the familiar S-shape conformational but could also form a long “extended” form and an intermediate “asymmetric” form somewhere between the compact and extended conformations (Figure 3.4C). Together, these results indicate that the Atg17 dimer is conformationally dynamic. To better understand these dynamics, analysis of the dimensions of these particles was conducted.

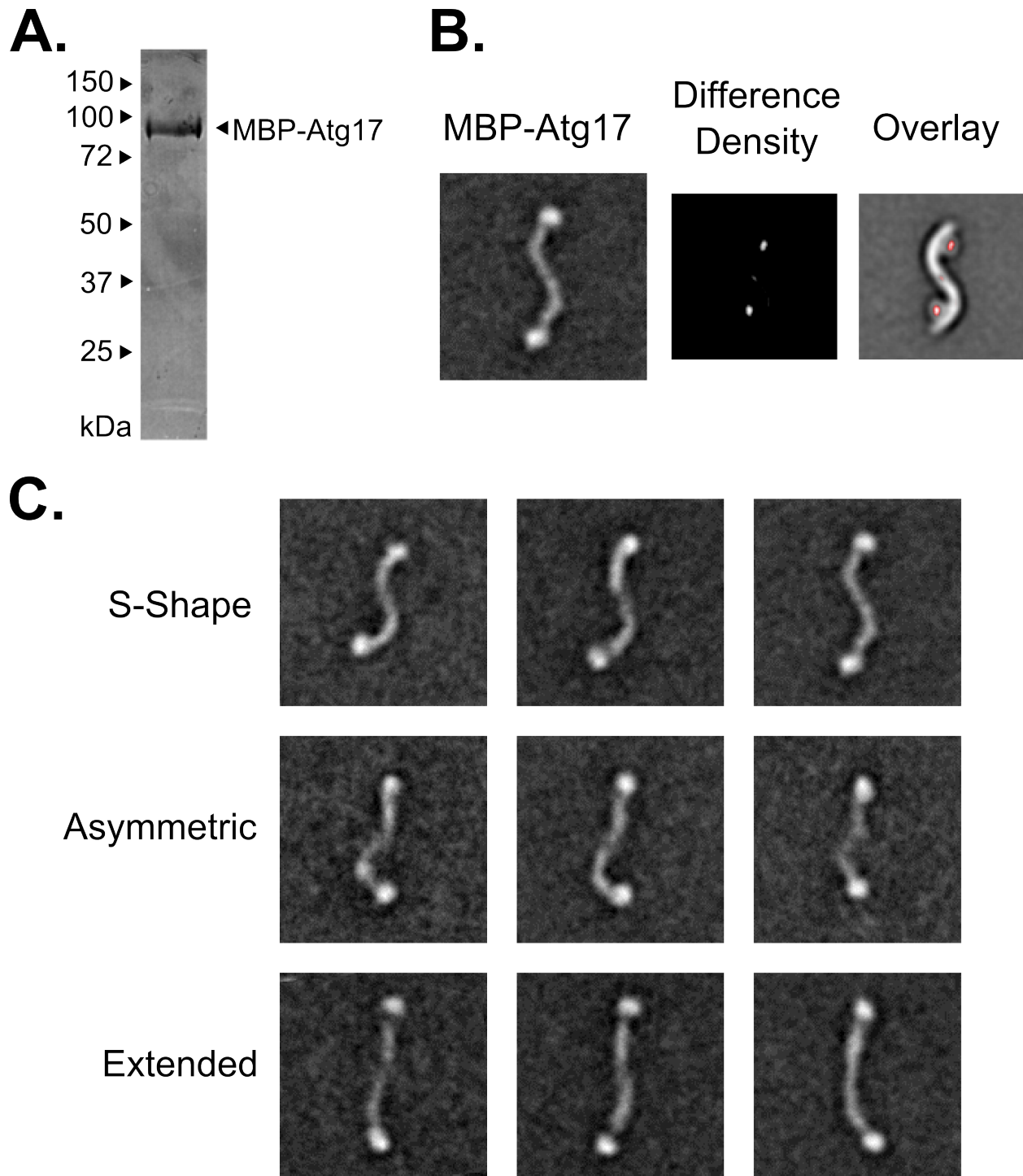


**Figure 3.4 Purification and EM analysis of the MBP-Atg17 dimer.** (A) Purified MBP-Atg17 analyzed by silver stained 12% SDS-PAGE. (B) Representative class average of MBP-Atg17 dimer obtained from 5,922 negative stained particles in 100 classes. Difference density is shown compared to MBP-Atg17-Atg31-Atg29 complex. Overlay shown is the difference density map over the untagged Atg17-Atg31-Atg29 complex. (C) Structural segregation of class averages from classification of 5,922 in 100 classes. MBP-Atg17 particles exhibiting a range of conformations Atg17 can adopt: S-shaped, asymmetric, and extended conformations. Side length of each panel is 64 nm.

### 3.6 Analyzing the conformational flexibility of the Atg17 dimer

To further investigate the conformational flexibility of Atg17 dimers, the radius of curvature and length of MBP-labeled Atg17 particles was compared to MBP-Atg17-Atg31-Atg29 particles. For this analysis, all selected class averages contained two discernible His-MBP densities because these averages showed well-defined boundaries for measurements. The length of a particle was measured as a junction-to-junction length at the boundary of the His-MBP linker and Atg17 (Figure 3.5A). The junction-to-junction lengths of His-MBP-labeled Atg17-Atg31-Atg29 particles fell within a narrow range between 275 Å to 310 Å, while the distribution of lengths was much broader for His-MBP-Atg17 and ranged from 158 Å to 345 Å (Figure 3.5B). Despite this variation in the range of lengths observed, the median values of length were 293 Å and 285 Å for the ternary complex and Atg17 respectively. These results indicate that the observed flexibility is an inherent property of Atg17 and is not significantly influenced by the presence of the His-MBP tags.

The radius of curvature was calculated from the measured cord length and arc height (Figure 3.5A). The measured curvature showed a narrow distribution of values for the His-MBP-labeled Atg17-Atg31-Atg29, with a median radius of 75 Å, whereas His-MBP-Atg17 exhibited a broader distribution, with a median radius of 213 Å. In fact, a large number of His-MBP-Atg17 particles exhibited little to no measurable curvature. Furthermore, when the radius of each arc was compared in a single dimer, we observed much lower correlation between the curvatures of each arc, indicating inherent flexibility of the two halves within the Atg17 dimer (Figure 3.5C). This was not observed in the context of the full complex as the radii of the two arcs correlated well, indicating a high degree of symmetry (Figure 3.5C)

Collectively, results from this analysis confirm that Atg17 is capable of adopting multiple conformations, and implicate a structural role of Atg31 and Atg29 in restricting this flexibility and maintaining the ternary complex in a rigid S-shape with well-defined curvatures.

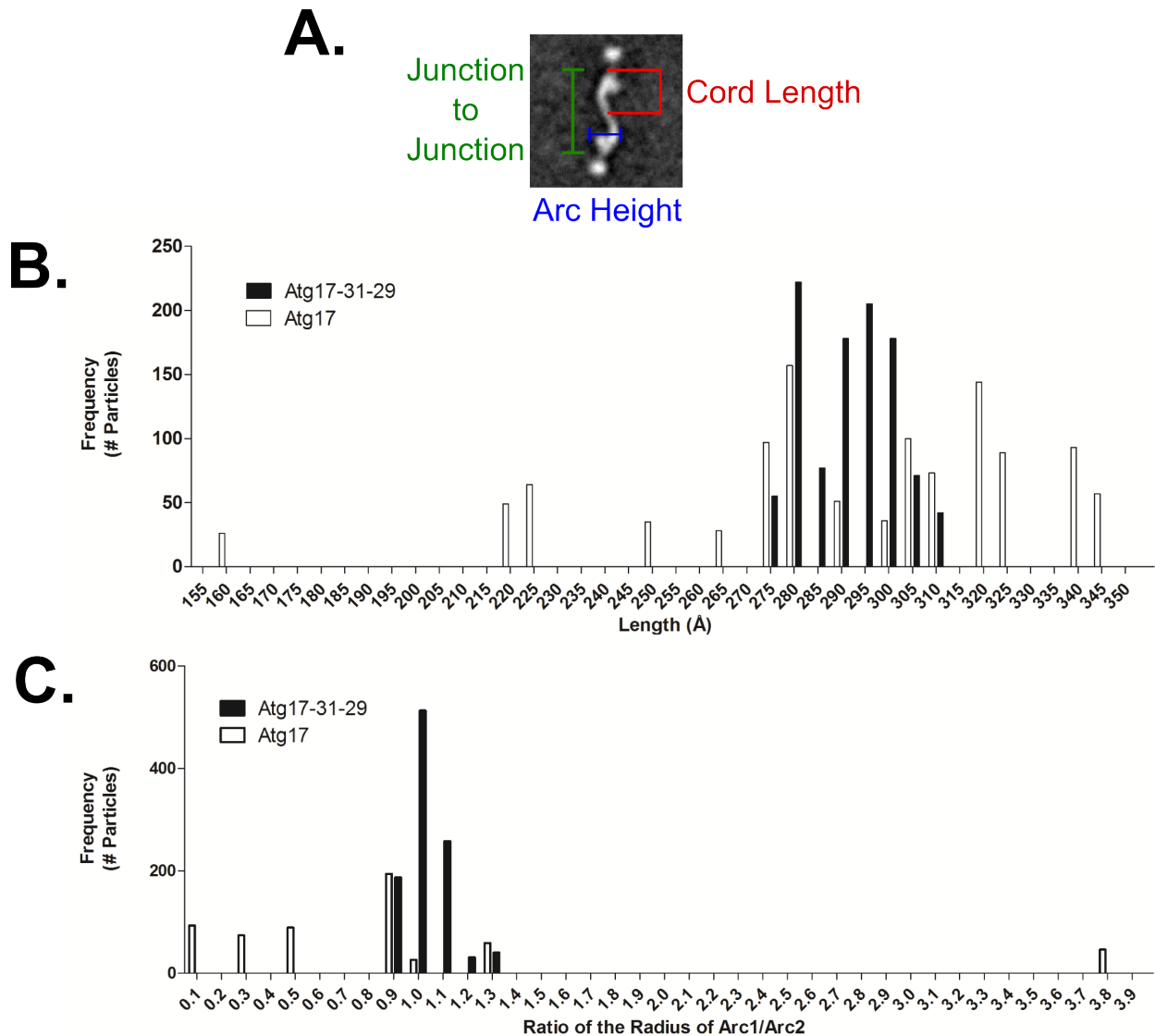


**Figure 3.5 Analysis of Atg17 dimer flexibility.** (A) A representative particle of MBP-Atg17-Atg31-Atg29 depicting measured parameters. (B) Distribution of junction-to-junction lengths measured for 17 class averages (1,029 total particles) of His-MBP-labeled Atg17-Atg31-Atg29 (black) and 18 class averages (1,099 total particles) of His-MBP-Atg17 (white). Median length was 293 Å and 285 Å for His-MBP-Atg17-Atg31-Atg29 and His-MBP-Atg17, respectively. (C) Distribution of the ratio of curvature measured for the two arcs within each ternary complex and Atg17 dimer. 17 class averages (1,029 total particles) of His-MBP-labeled Atg17-Atg31-Atg29 (black) and 9 class averages (539 total particles) of His-MBP-Atg17 particles (white) were analyzed. Median radius was 75 Å and 213 Å for His-MBP-Atg17-Atg31-Atg29 and His-MBP-Atg17, respectively.

### 3.7 Analysis of an “autophagy-induced” complex with phosphomimetic Atg29

Atg29 is phosphorylated in response to autophagy activation with several putative Atg29 phosphorylation sites being mapped to S197, S199, and S201<sup>99</sup>. Thus, complexes harbouring phosphorylated Atg29 should represent an “autophagy active” complex. To further study structural changes to the Atg17-Atg31-Atg29 complex during autophagy induction, Atg17-Atg31-Atg29 complex harbouring a phosphomimetic Atg29 mutant were purified and subject to negative stain 2D EM analysis. These Atg29 mutants were generated by mutating S197, S199, and S201 to an aspartate residue, and either leaving the first 20 serine/threonine residues unmutated (Atg29[3SD]) or mutating them to alanine (Atg29[20STA/3SD]). Two galleries of class averages were obtained from the classification of 4,671 Atg29[3SD]-containing and 6,558 Atg29[20STA/3SD]-containing particles, respectively (Figure 3.6A and B). Compared to the wild-type complex these averages indicated that the phosphomimetic mutations did not induce significant changes to the overall structure of the ternary complex as observed by EM.

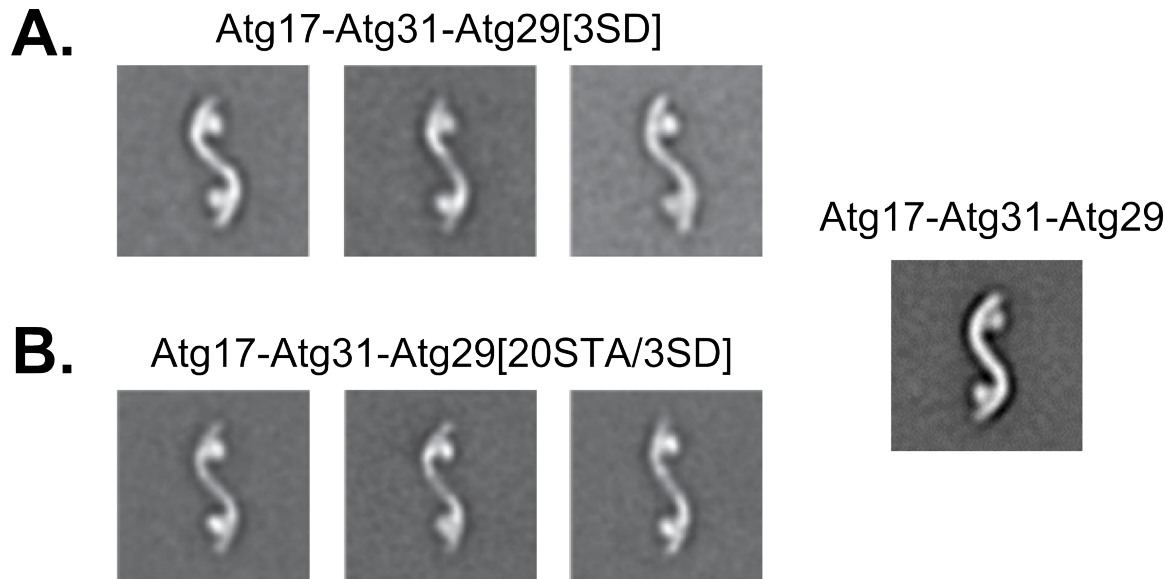


**Figure 3.6 Analysis of phosphomimetic Atg29 containing complexes.** A representative class average of Atg17-Atg31-Atg29 is on the right for reference. (A) Representative class averages obtained from classification of 4,671 negatively stained Atg29[3SD]-containing particles into 50 classes. (B) Representative class averages obtained from classification of 6,588 negatively stained Atg29[20STA/3SD]-containing particles into 50 classes.

### 3.8 Purification of the Atg1 kinase complex pentamer

The Atg1 kinase complex is composed of Atg1, Atg13, and the Atg17-Atg31-Atg29 ternary subcomplex. This complex is an important regulator of autophagy during starvation in yeast. Previous work identified the interaction interface of Atg1, Atg13, and Atg17, which mediates complex formation<sup>63,76,77,78,91</sup>. The Atg1 C-terminus (CTD) contains the binding site for Atg13, while the Atg13 C-terminus (CTD) contains the binding site for Atg1. The interaction of Atg17 with Atg1 is likely bridged through Atg13, indicating Atg13 is likely important for complex integrity. Another group recently showed that a minimal Atg1 kinase complex, consisting of small domains of Atg1 and Atg13 with full-length Atg17-Atg31-Atg29, could be reconstituted in an *E. coli* system<sup>92</sup>.

To gain structural insight into how Atg1 and Atg13 assemble with Atg17-Atg31-Atg29, we reconstituted a minimal Atg1 kinase complex. More specifically, full-length Atg17-Atg31-Atg29 was co-expressed with Atg1 CTD (residues 589-897) and either Atg13 middle domain (MD; residues 384-602), Atg13 C-terminal domain (CTD; residues 384-738), or Atg13 full-length (FL; residues 1-738) (Figure 3.7A). Compared to the previously mentioned pentamer assembly, our strategy uses much larger fragments of Atg13 (compared to Atg13 residues 350-550), which we believed would aid in visualization by EM.

To facilitate expression of this complex, we devised a new purification strategy using the pQLINK system<sup>112</sup>. This system takes advantage of a novel multiple cloning site which can “link” separate genes by ligation-independent cloning into a single plasmid. Using this system all five genes, Atg17, Atg31, Atg29, Atg1 CTD and the various forms of Atg13 (MD, CTD and FL) were cloned into a single vector. Atg31 was C-terminal His-tagged for purification purposes. To determine which pentamer assembly would be the most stable, the different forms of Atg13 were co-expressed with Atg17-Atg31-Atg29-Atg1 CTD in *E. coli* and purified by a single-step nickel-sepharose pull down followed by elution with 100 mM imidazole. The results of these preliminary purifications were analyzed by 12% SDS-PAGE gel (Figure 3.7B).

Purification of the pentamer should yield five distinct bands corresponding to the different components of the Atg1 kinase complex. Previous purification of the Atg17-Atg31-Atg29 (Figure 3.1A, 3.2A) shows that three bands are clearly observed at around the correct molecular weight for Atg17 (50kDa), Atg31 (22.1 kDa), and Atg29 (24.7 kDa). The expected sizes for these bands are annotated by arrows to the right of the gels (Figure 3.7B). Atg1 and Atg13 have not been purified previously, and thus an approximation of their molecular weight is depicted. Atg1 CTD is approximately 35.7 kDa and shown on the right of the gels by an arrow while the different constructs of Atg13 are as follows; Atg13 MD (23.7 kDa), Atg13 CTD (39.1 kDa), and Atg13 FL (83.3 kDa), and are labeled as a \* beside the corresponding gel.

From Figure 3.7B, purification of all pentamer complexes exhibited the presence of bands corresponding to the Atg17-Atg31-Atg29 in relatively stoichiometric levels. Another observation is that bands that correspond to the approximate molecular weight of the Atg13 constructs co-purified with Atg17-Atg31-Atg29 (Figure 3.7B), although the Atg13 MD is questionable due to the band being observed in all fractions. Looking more closely at the purification of Atg13 MD and Atg13 FL complexes, these purification did not exhibit a co-purified band corresponding to Atg1 CTD, due to the absence of a band around 35.7 kDa in size. The only purified complex that exhibited a presumed Atg1 CTD band was that of the Atg13 CTD pentamer assembly (Figure 3.7B). Thus, we moved forward to large-scale purification and structural characterization by EM of the Atg1 kinase complex pentamer containing Atg17-Atg31-Atg29, Atg1 CTD (residues 589-897), and Atg13 CTD (residues 384-738).

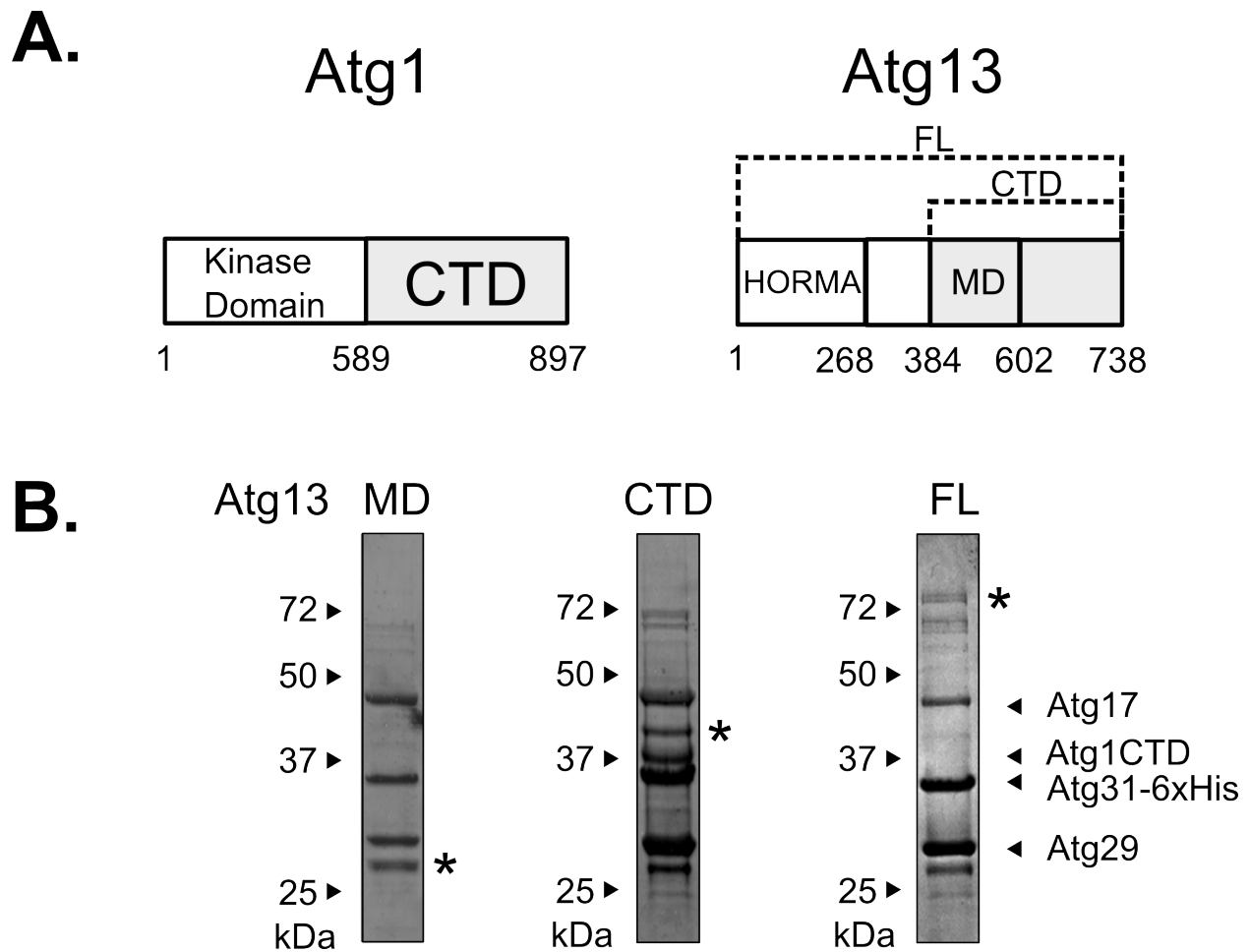


**Figure 3.7 Expression and purification of Atg1 kinase complex assemblies.** (A) Constructs of Atg1 and Atg13 used in pentamer assembly. CTD; C-terminal domain. HORMA<sup>95</sup>; Hop1p, Rev1p, and Mad2, MD; Middle-domain, FL; Full-length. (B) Ni<sup>2+</sup> imidazole elution of purified Atg1 kinase pentamer complexes expressed in *E. coli*. Coomassie-stained 12% SDS-PAGE. Predicted size of protein is shown on the right. \* indicates predicted Atg13 construct.

### 3.9 Structural analysis of the Atg1 kinase complex pentamer

With the identified Atg1 kinase complex assembly in hand, we sought to further structurally characterize the complex by single-particle EM. The Atg17-Atg31-Atg29-Atg1 CTD-Atg13 CTD complex was expressed in *E. coli* and purified by single-step nickel-sepharose chromatography. The complex was further separated by gel-filtration chromatography and the peak fraction was analyzed by 12% SDS-PAGE (Figure 3.8A). The results show that the complex does indeed purify as a pentamer assembly with five bands observed. Importantly, the complex eluted at a similar size to the Atg17-Atg31-Atg29 complex showing that the Atg1 and Atg13 components do indeed interact with the ternary complex. It is noted, however, that the stoichiometry of the complex was not readily determined from the observed gel. All components appear in stoichiometric quantities except for Atg13 CTD, which was less intense.

Nevertheless, the complex was visualized by negative-stain EM and analyzed by 2D analysis. The most dominant classes showed that the pentamer complex was structurally similar to the Atg17-Atg31-Atg29 complex (Figure 3.8B, -Glut Atg17-Atg31-Atg29-Atg1 CTD-Atg13 CTD). Indeed, almost no distinguishing features could be observed between the Atg17-Atg31-Atg29 and Atg17-Atg31-Atg29-Atg1 CTD-Atg13 CTD complexes. Therefore, we attempted a modified protocol using a mild protein cross-linker to promote stability of the complex and provide a sample that is more amenable to analysis by EM.

We employed gradient fixation (GraFix)<sup>114</sup> to further study the Atg1 kinase complex pentamer. GraFix uses a combination of a glycerol gradient centrifugation with the addition of glutaraldehyde. Glutaraldehyde is layered as a gradient in the glycerol gradient and thus a protein sample which travels into the glycerol gradient during centrifugation will encounter an increasing level of glutaraldehyde. Glutaraldehyde non-selectively crosslinks free amino groups and as a consequence too much fixative can result in the formation of artefacts. To test whether the GraFix protocol would cause artificial changes to the pentameric assembly, we performed a mock analysis of GraFix treated Atg17-Atg31-Atg29.

Atg17-Atg31-Atg29 was purified by single-step nickel-sepharose and gel filtration chromatography. The protein sample was then loaded onto a 12-24% glycerol gradient containing a

0-0.05% glutaraldehyde gradient. The tube was centrifuged at 40,000 rpm for 16 hours and the entire gradient was fractionated. The peak fraction was visualized by negative-stain EM and analyzed by 2D class average analysis. Our results show that the GraFix treated complex adopts a similar structure to the Atg17-Atg31-Atg29 complex and shows that the use of glutaraldehyde does not appear to significantly alter the structure of the complex (Figure 3.8B, +Glut Atg17-31-29).

The GraFix protocol was then used on the Atg17-Atg31-Atg29-Atg1 CTD-Atg13 CTD pentamer assembly. Again, using a 12-24% glycerol gradient with a 0-0.05% glutaraldehyde gradient, the purified pentamer assembly was subject to 2D class average analysis (Figure 3.8B). The GraFix treated pentamer assembly exhibited a similar overall structure to the Atg17-Atg31-Atg29 complex. When compared to the ternary complex and the unfixed pentamer complex it was observed that the terminal regions of the S-shape were enlarged and appeared to have additional density. These results indicate that our method allowed for observation of additional features in the structure. However, interpreting these observations is hindered by our inability to definitively localize the Atg1 CTD and Atg13 CTD from these images, despite each subunit being >30 kDa in size. These observations are likely due to inherent flexibility of the components leading to an “averaging” out of density or could suggest that Atg1 CTD and Atg13 CTD lay extremely close to the S-shape structure. To circumvent this problem, we applied the fusion-label approach by fusing large, “bulkier” tags to the Atg1 CTD and Atg13 CTD.

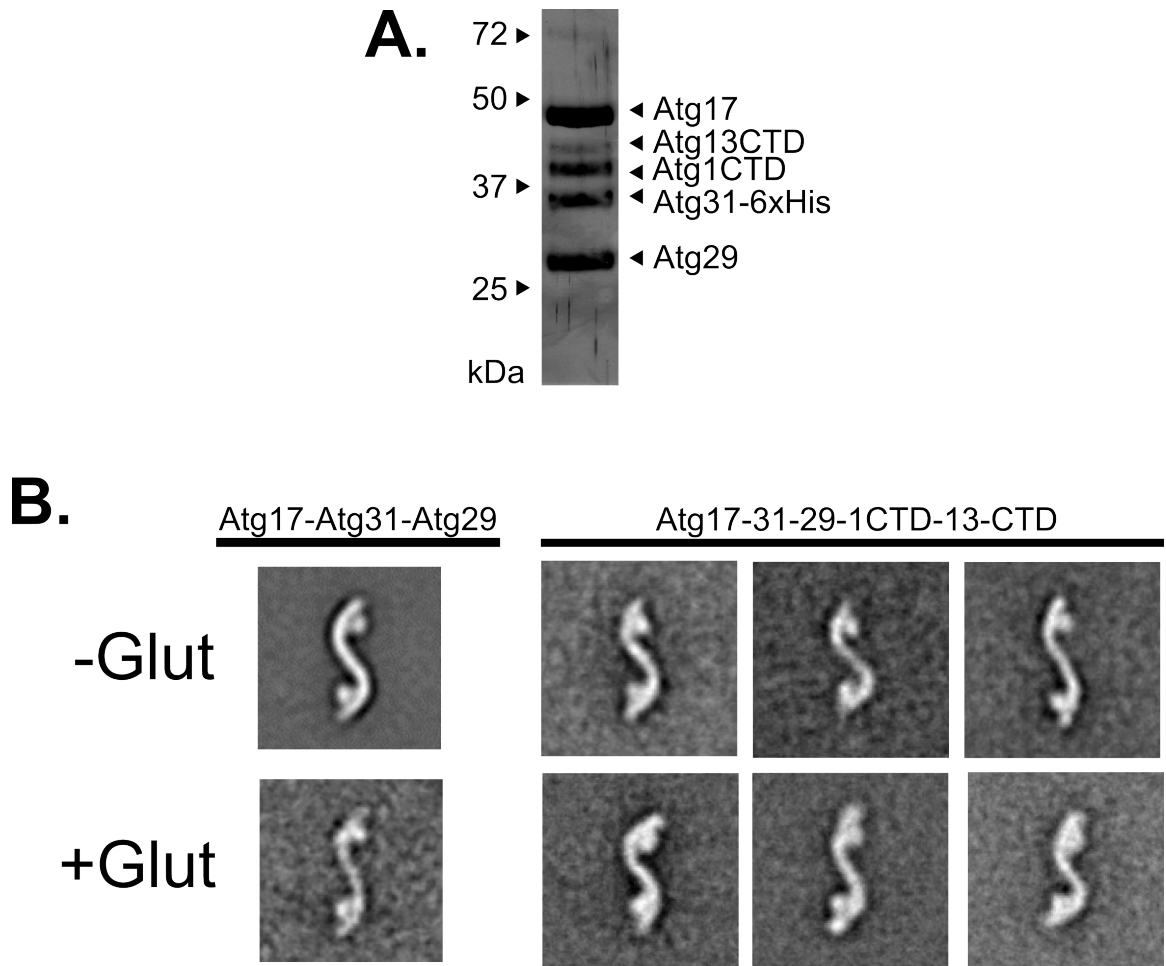


**Figure 3.8 EM analysis of the Atg1 kinase complex pentamer.** (A) Analysis of the purified Atg17-Atg31-Atg29-Atg1 CTD-Atg13 CTD pentamer complex by silver-stained 12% SDS-PAGE. Predicted sizes are labelled on the right. (B) EM analysis of the Atg1 kinase complex pentamer. Representative class average of Atg17-Atg31-Atg29 and Atg17-Atg31-Atg29-Atg1 CTD-Atg13 CTD complexes with (+Glut) and without GraFix (-Glut). Pentamer 3,700 particles. GraFix Pentamer 2,787 particles. Atg17-Atg31-Atg29 1,968 particles. Side length of each panel is 55 nm.

### 3.10 Subunit localization of Atg1 and Atg13 in the pentamer assembly

Despite obtaining adequate quantities of the Atg17-Atg31-Atg29-Atg1 CTD-Atg13 CTD pentamer complex for EM analysis, we were unable to definitively localize Atg1 and Atg13. To facilitate localization of these components in the EM structure, we fused a His-MBP tag to the N-terminus of Atg1 CTD or Atg13 CTD. These His-MBP-labelled genes were cloned with Atg17-Atg31-Atg29 and either unlabeled Atg1 CTD or unlabeled Atg13 CTD using the pQLINK system. The pentameric complex was then expressed and purified by single-step nickel-sepharose and gel filtration chromatography followed by the GraFix protocol. Both complexes were purified and subsequently analyzed by 12% SDS-PAGE.

The addition of a His-MBP-tag should increase the observed molecular weight of tagged components by approximately 42.5 kDa. Analysis of the purified complex showed that indeed the addition of the His-MBP tag shifted the molecular weight of both Atg1 CTD and Atg13 CTD to exhibit a band between the 72 kDa and 100 kDa molecular weight marker (Figure 3.9A and 3.9B). In the His-MBP-Atg1 CTD purified complex, bands corresponding to Atg17, Atg31, Atg29, and Atg13 CTD were clearly observed. While the His-MBP-Atg13 CTD containing complex only had bands corresponding to the Atg17-Atg31-Atg29 subcomplex. These results may indicate that the presence of the bulky His-MBP-tag at the N-terminus of Atg13 may interfere with interaction with Atg1 CTD.

The purified complex was visualized by negative-stain EM and subject to 2D analysis. For the His-MBP-Atg1 CTD purified complex, a total of 1,471 particles were analyzed. These results showed that the complex formed an S-shape structure with additional densities observed appended to the terminal ends of the S-shape, similar to what was observed with the His-MBP-Atg17 labeled complex (Figure 3.3A and 3.9A). This analysis indicated that His-MBP-Atg1 CTD is localized close to the terminal regions of the S-shape but not along the tubular central region.

For the His-MBP-Atg13 CTD containing complex, a total of 1,702 particles were analyzed. The averages for this dataset were much more well defined and clear densities were again observed appended to the terminal regions of the S-shape indicating that MBP-Atg13 CTD is localized in this region (Figure 3.9B). These labelling results further broaden our model for Atg1 kinase complex assembly. Atg17 forms

a central scaffold while Atg31 and Atg29 contribute to the globular densities localized at the terminal regions of the S-shape. Atg1 CTD and Atg13 CTD likely only interact with the extreme terminal regions of the S-shape.

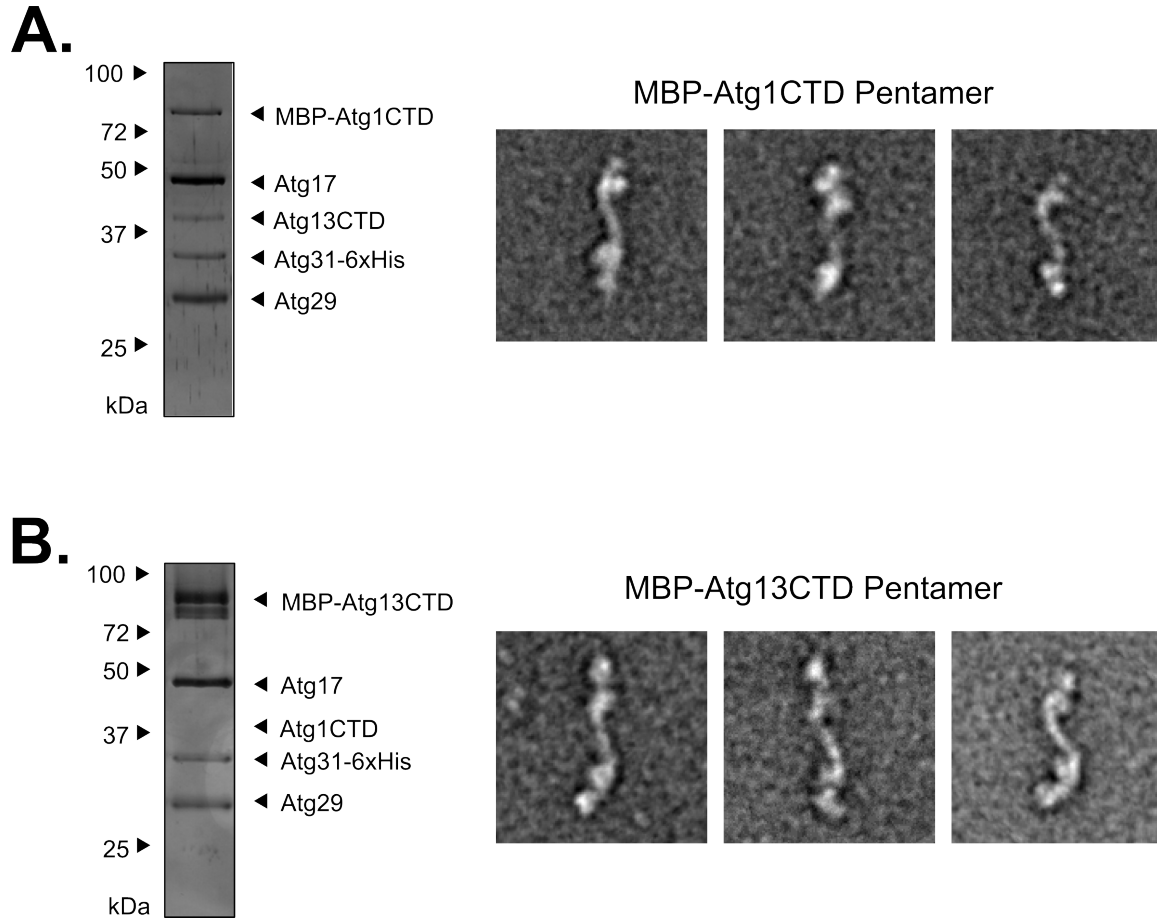


**Figure 3.9 Mapping of Atg1 CTD and Atg13 CTD in the Atg1 kinase complex pentamer.** Minimal Atg1 kinase complex pentamer assemblies were expressed with either His-MBP-labeled Atg1 CTD or Atg13 CTD. The complex was purified and subject to GraFix. SDS-Page analysis of the purified complex is shown. (A) His-MBP-Atg1 CTD containing pentamer. Representative class averages from 1,471 negatively stained His-MBP-Atg1 CTD particles from 100 classes. (B) His-MBP-Atg13 CTD containing pentamer. Representative class averages from 1,702 negatively stained His-MBP-Atg13 CTD particles from 100 classes. Side length of each panel is 55 nm.

### 3.11 Purification and EM analysis of Atg11

As a further extension to study the Atg1 kinase complex, we decided to characterize the Atg11 protein scaffold. In yeast, Atg11 is essential for the Cvt pathway but has also been found to play a significant role in organization of the PAS during basal autophagy and in the absence of Atg17. Importantly, Atg11 directly interacts with components of the Atg1 kinase complex. Studying Atg11 would provide insight into how the Atg1 kinase complex contributes to autophagy and organization of the PAS during nutrient rich conditions.

Atg11 has a predicted mass of 135 kDa, which made expression in bacterial systems particularly challenging. To facilitate expression of Atg11, we decided to use the pESC yeast expression system. This expression system uses a 2-micron plasmid that contains a two multiple cloning sites driven by a galactose inducible promoter. In this case, we only used one cloning site to insert Atg11 in frame with a C-terminal FLAG tag. The Atg11 containing pESC-URA vector was transformed into the protease-deficient BJ2168 yeast strain followed by growth on 2% raffinose containing uracil-minus media prior to induction with 2% galactose. Atg11 was purified by Anti-FLAG M2 resin chromatography followed by elution with 0.5 mg/ml FLAG peptide. The protein was separated by gel filtration chromatography and the peak fraction was analyzed by SDS-PAGE gel.

Results of our purification showed the presence of a single band between the 100 kDa and 150 kDa marker (Figure 3.10A). The observed band is a similar size to the predicted 136 kDa size of FLAG-tagged Atg11. This fraction was then visualized by negative stain EM. A heterogeneous mixture of particles was observed, and these particles appeared to exhibit an extended architecture (Figure 3.10B). Atg11 was then subject to 2D analysis, and a total of 2,636 particles were analyzed. The observed class averages showed that Atg11 adopts an elongated architecture indicative of a coiled-coil containing protein. Intriguingly, Atg11 can adopt an S-shape structure analogous to the Atg17-Atg31-Atg29 subcomplex, but is also inherently more flexible as alternative conformations were observed (Figure 3.10C). Further inspection of the gallery of averaged image revealed that a subset of Atg11 particles adopt a dimeric state. This observation is supported by previous biochemical analysis showing that Atg11 homodimerizes<sup>101</sup>.

Although the majority of Atg11 particles appeared to exist in a monomeric state, these observations remain to be confirmed as potential artefacts might arise from a dataset with heterogeneous particles. Nevertheless, these results provide the first glimpse of the molecular architecture of Atg11.

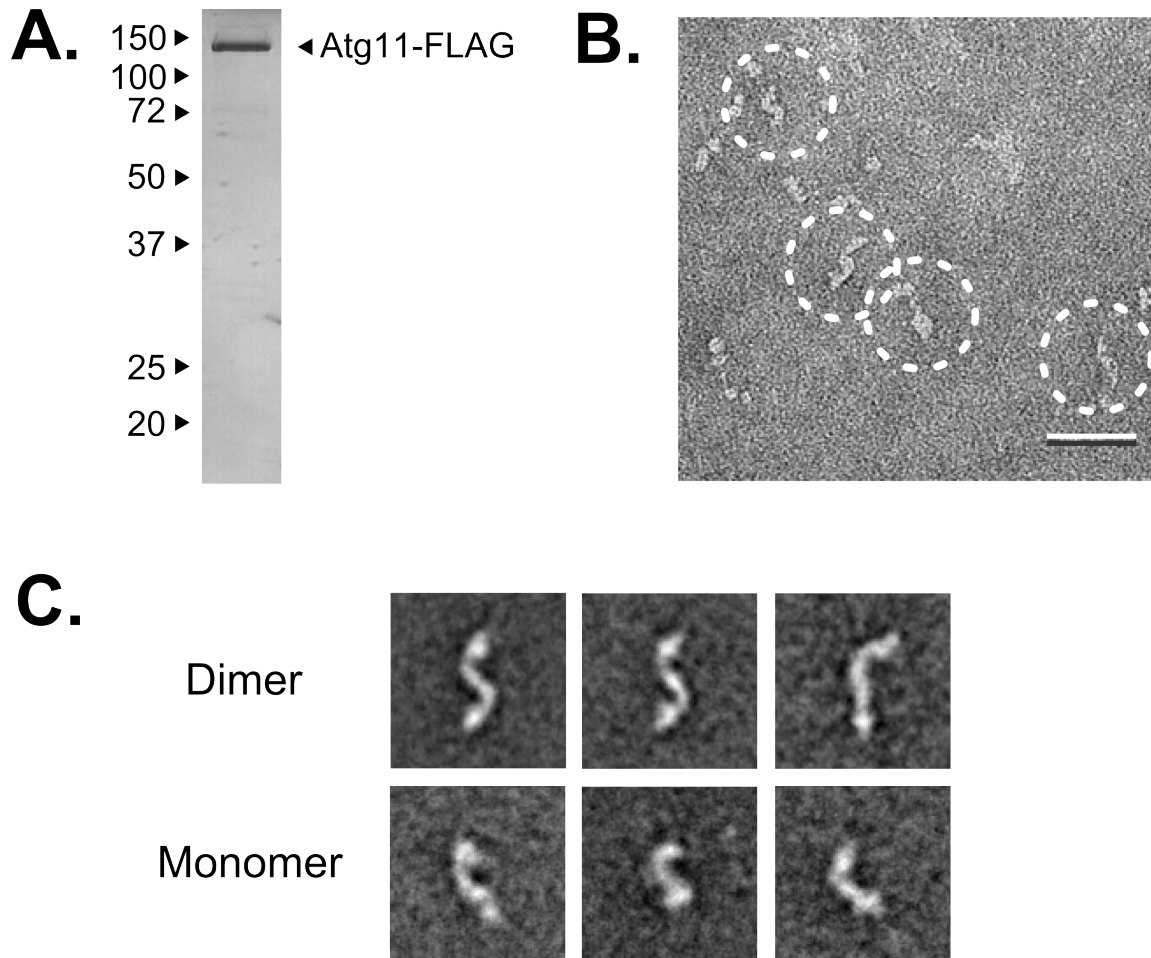


**Figure 3.10 Purification and EM analysis of Atg11.** (A) Atg11-FLAG was overexpression in yeast and purified by Anti-FLAG M2-resin and gel filtration chromatography and analyzed by 12% SDS-PAGE visualized by coomassie staining. (B) Representative raw image of negative-stained Atg11-FLAG. Particles are dotted in circles (scale bar = 50nm). (C) 2D analysis of 2,636 negatively stained particles. Major representative classes are shown and exhibit an elongated architecture. Potential monomer and dimer forms of Atg11 were observed. Side length of each panel is 42 nm.

## Chapter 4: Discussion

In this study, the structure of the Atg1 kinase complex was analyzed by single-particle EM. Results from my studies provided the first EM structure of the *S. cerevisiae* Atg17-Atg31-Atg29 regulatory subcomplex, and generated novel insights into the subunit interaction between Atg1 and Atg13 with Atg17-Atg31-Atg29. During the course of this study, the X-ray crystal structure of the Atg17-Atg31-Atg29 complex from the thermophilic yeast *L. thermotolerans* was determined<sup>92</sup>. Here the various models of Atg1 kinase complex formation will be consolidated and further discussed. I have also carried out preliminary structural studies on the important PAS organizer and protein scaffold Atg11.

### 4.1 Structure of the Atg17-Atg31-Atg29 regulatory subcomplex

#### 4.1.1 The EM structure of *S. cerevisiae* Atg17-Atg31-Atg29

Atg17, in complex with Atg31 and Atg29, function in the very early steps of autophagosome formation. Together, the Atg17-Atg31-Atg29 subcomplex functions as a positive regulator of the Atg1 kinase complex through mediating recruitment of Atg proteins to the PAS. The EM structure of Atg17-Atg31-Atg29 shows that the complex adopts a highly extended dimeric “S-shaped” structure with an end-to-end distance of 345 Å. Analysis of purified Atg17, confirmed that Atg17 made up a large part of the density of the complex and was likely mediating dimerization. The observations of two additional globular densities appended to the terminal regions of the “S-shape” were proposed to consist of Atg31 and Atg29, as seen from GFP-labeling experiments. The strikingly similar overall morphologies between recombinant and native Atg17-Atg31-Atg29 supported the physiological relevance of the model generated from the recombinant complex. Our model presents several key features that would mediate the function of the Atg17-Atg31-Atg29 subcomplex.

The complex adopts an elongated structure composed mostly of Atg17. In Atg17’s identified role as a protein scaffold, this extended architecture would provide a larger surface area for accessibility to docking interfaces on the complex. Indeed, other elongated protein scaffolds have been identified in the

literature<sup>130,131</sup>. Additionally, the dimeric nature of the Atg17-Atg31-Atg29 complex would functionally double the interaction sites and generates two modules, further promoting protein-protein interactions.

The two regulatory subunits, Atg31 and Atg29, localize to the terminal regions of the S-shape and make up the globular densities observed. The globular density is appended to the concave side of the Atg17 arc. As both proteins are phosphorylated during autophagy, this configuration would orient Atg31 and Atg29 in such a manner that would potential promote accessibility of their phosphorylation motifs to kinases. Although our EM studies on complexes containing phosphomimetic Atg29 show that phosphorylation likely does not appear to alter the overall architecture of Atg17-Atg31-Atg13, the structural changes induced by phosphorylation could be too subtle to be clearly distinguished by our techniques.

#### **4.1.2 The crystal structure of *L. thermotolerans* Atg17-Atg31-Atg29**

Recently, Ragusa *et al.* reported a structure of Atg17-Atg31-Atg29 based on crystallographic analysis of the Atg17-Atg31-Atg29 complex from the thermophile *L. thermotolerans* (Figure 4.1A). Notably, the crystal structure matched the EM structure of Atg17-Atg31-Atg29 from *S. cerevisiae*, despite relatively low sequence homology between the proteins from each species. Indeed, the high-resolution structure of the *L. thermotolerans* complex was unambiguously docked into our EM density map, which supports the physiological relevance of the high-resolution structure (Figure 4.1C).

The crystal structure of Atg17 is composed of four  $\alpha$ -helices forming a three-helix bundle. Atg31, on the other hand, adopts a  $\beta$ -sandwich motif with a single C-terminus  $\alpha$ -helix mediating interaction with Atg17 to form a four-helix bundle. In contrast, Atg29 is predominantly unstructured and only a single N-terminal  $\beta$ -strand that is engaged in an interaction interface with the N-terminus  $\beta$ -sandwich of Atg31 could be clearly defined from the electron density map. Atg31 and Atg29 forms stable heterodimers that interact with Atg17 through Atg31 and further localize to the concave side of the Atg17 arc.

The observed interaction interfaces from the crystal structure matches well with our predicted subunit organization determined from labeling experiments (Figure 4.1C). The N-terminus of Atg17 is found at the terminal region of the observed arc. The exception is the location of the C-terminus of Atg31, which in our EM analysis was localized to the convex side of the arc while in the high-resolution model it is localized to the concave side of the arc. This difference may be due to the ~12 amino acid linker joining Atg31 to GFP. As the diameter of Atg17 is ~35 Å, the linker joining the GFP moiety would be long enough to localize in the observed region. The C-terminus of Atg29, on the other hand, lacked resolvable electron density in the high-resolution model, and we were not able to compare its localization to the EM structure. The crystal structure suggests that the C-terminus of Atg29 likely points outward and away from Atg17. The docking analysis shows there is no apparent unaccounted density observed for Atg29. This observation further indicates that the C-terminal region of Atg29 is either completely unstructured or adopts a multitude of conformations that single-particle EM is unable to resolve.

The high-resolution model also confirmed that Atg17 mediates dimerization of the complex, which matches what we observed from studying the Atg17 dimer. The C-terminus of Atg17 mediates dimerization through several coiled coils. Furthermore, Ragusa *et al.* determined that Atg17 dimer formation was physiological relevant for the autophagy response by expressing C-terminal Atg17 truncations. Both localization of Atg17 and Atg8, to the PAS, and autophagy was impaired in cells expressing these mutants. Overall, both the crystal structure and EM structures support that the physiologically relevant form of the Atg17-Atg31-Atg29 is the dimeric form.

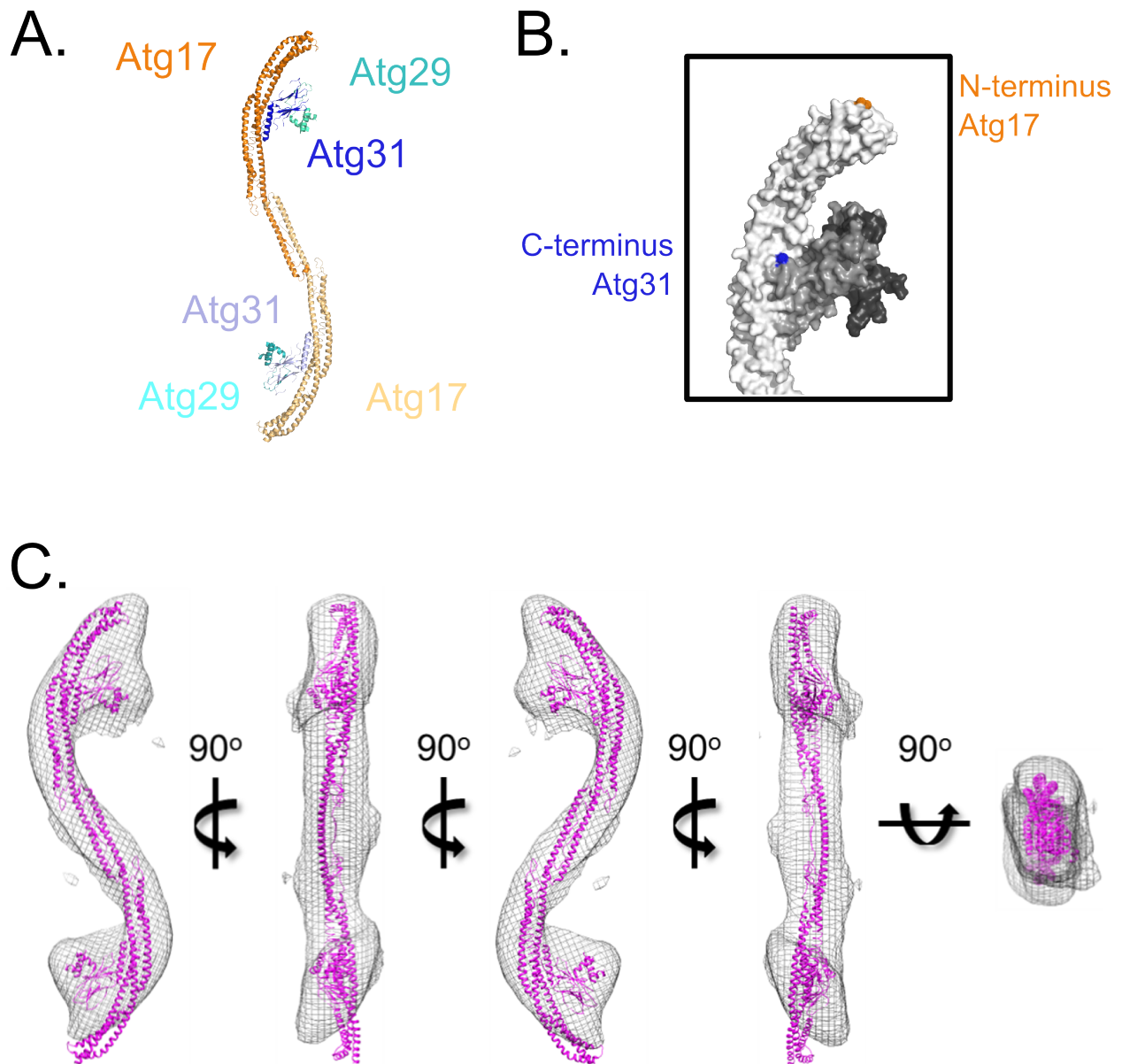


**Figure 4. 1** The crystal structure of *L. thermotolerans* Atg17-Atg31-Atg29. (A) Crystal structure of *L. thermotolerans* Atg17-Atg31-Atg29 (PDB accession code 4HPQ) with labeled Atg17 (orange), Atg31 (blue), Atg29 (cyan). (B) Localization of the N-terminus of Atg17 (orange) and C-terminus of Atg31 (blue) in the surface model of Atg17-Atg31-Atg29. (C) Docking of the crystal structure of the Atg17-Atg31-Atg29 complex into the EM density map of the *S. cerevisiae* complex. Docking was performed using UCSF Chimera and the panels represent the docked solution viewed in various orientations.

### 4.1.3 The business “N” of Atg17

Atg17 forms the bulk of the Atg17-Atg31-Atg29 complex and mediates its dimerization. Structural analysis of the purified Atg17 homodimer revealed that it is inherently dynamic and can adopt a range of conformations. The largest variability occurs at the terminal regions of the dimer. From analysis of particle dimensions, we showed that this observed flexibility contributes to variable lengths and curvature of the Atg17 arc. When compared to Atg17, in complex with Atg31 and Atg29, we further showed that Atg31 and Atg29 reduce conformational flexibility of Atg17, restricting the terminal region to a curved architecture. Thus, we propose a model in which Atg31 and Atg29 have a structural role in maintaining curvature of Atg17 (Figure 4.2A).

Previous studies identified critical regions required for Atg17's interaction with Atg1 and Atg13, key components of the Atg1 kinase complex<sup>63,76,77,78,91</sup>. According to the high-resolution model, these N-terminal regions localize distal to the point of contact of the Atg31-Atg29 dimer, where curvature is most prominent. These findings were further confirmed by sequence alignment of Atg17 from nine yeast species (see Appendix C.1 and Figure 4.2B; red residues). In total, several highly conserved regions were identified: an Atg31-interaction interface, a dimerization interface, and the N-terminal region of Atg17. Importantly, the conserved N-terminal region contained the proposed Atg1-Atg13 interaction interfaced mapped by previous biochemical analysis<sup>76,91</sup>.

Together, these observations highlight a role for the N-terminus of Atg17 as an important interface for interaction and formation of the Atg1 kinase complex. Additionally, Atg31 and Atg29 induce the observed curvature of this region. It is therefore possible that the distinct curvature is required for Atg17-Atg31-Atg29 binding to Atg1 and Atg13 in the context of the Atg1 kinase complex.

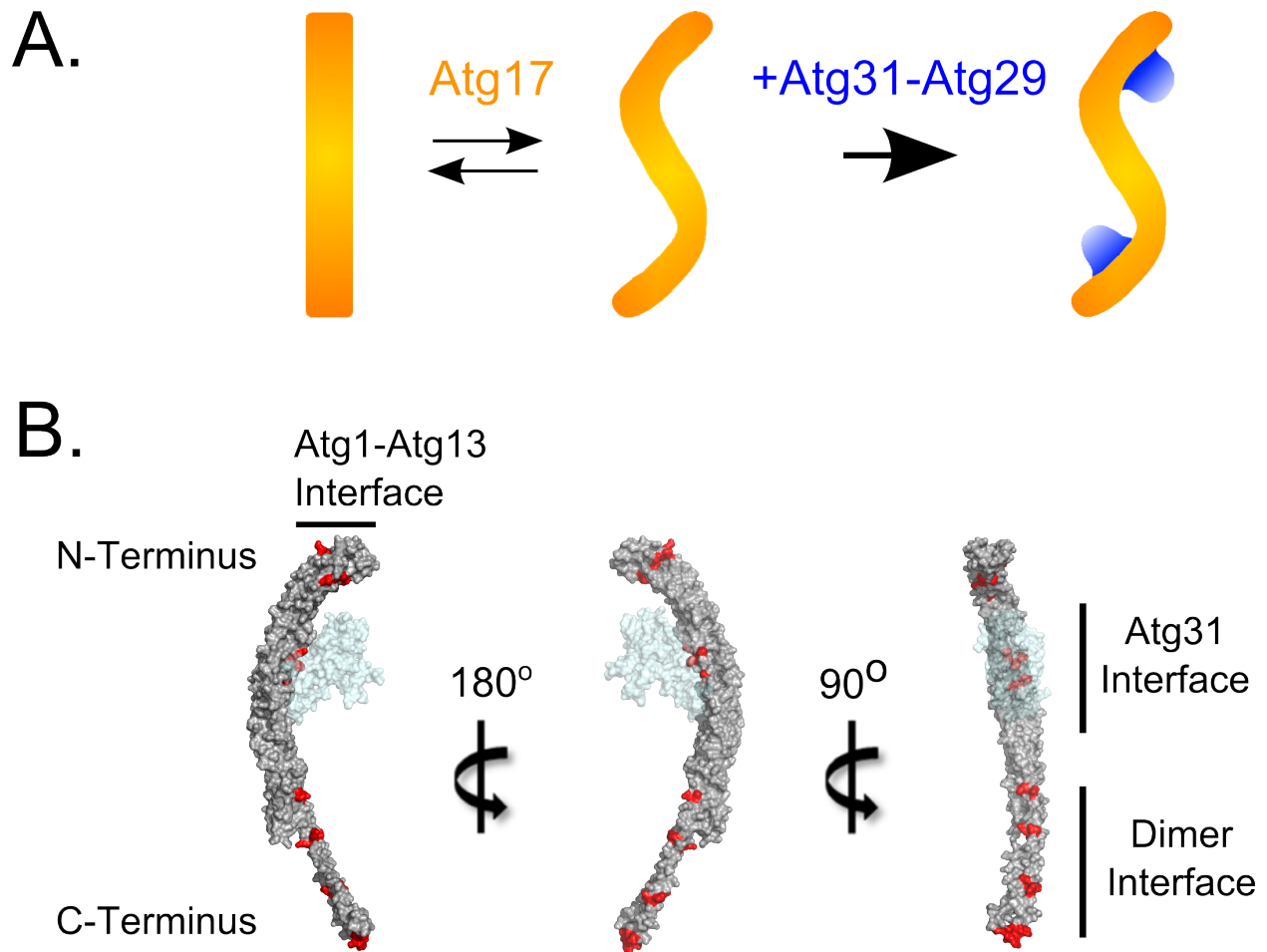


**Figure 4. 2 The N-terminus of Atg17 forms a curved interaction interface.** (A) A model for regulation of Atg17 conformational dynamics. In the absence of Atg31 and Atg29, Atg17 was observed to possess a high degree of flexibility. When Atg31 and Atg29 are present, the conformational flexibility of Atg17 is restricted into a curve, “S-shaped” architecture. (B) Identified interaction interfaces of Atg17. A single protomer of Atg17 (Grey) in complex with Atg31-Atg29 (transparent blue) in several orientations. Red residues are highly conserved between nine yeast species (see appendix C.1) and make up several interaction interfaces: putative Atg1-Atg13 interaction interface, Atg31 interaction interface, dimer interface.

## 4.2 Structure of the Atg1 kinase complex

### 4.2.1 Purification of the Atg1 kinase complex pentamer

The Atg17-Atg31-Atg29 subcomplex is part of the much larger Atg1 kinase complex. To determine how this complex assembles, we attempted to purify a limited pentamer assembly consisting of Atg17, Atg31, Atg29, Atg1 and Atg13. Previously, Ragusa *et al.* identified a minimal Atg1 kinase complex from *Kluyveromyces lactis* consisting of Atg17, Atg31, Atg29 and small domains from Atg1 (residues 562-831) and Atg13 (residues 350-550)<sup>92</sup>. This study laid a framework for us to identify the boundaries of Atg1 and Atg13 in the *S. cerevisiae* system for recombinant purification. We attempted to purify complexes containing Atg17-Atg31-Atg29 and the C-terminal domain of Atg1 (589-897) with several constructs of Atg13: Atg13 MD (residues 384-602), Atg13 CTD (residues 384-738) and Atg13 FL (residues 1-738). From the preliminary purifications, we observed that only complexes containing the Atg13 CTD construct purified as a pentamer assembly. Although Ragusa *et al.* purified their "mini pentamer" containing the middle domain of *K. lactis* Atg13 (residues 350-550), we did not obtain the same results using the analogous *S. cerevisiae* MD domain. This may indicate that our proposed construct, designed by sequence alignment of *K. lactis* and *S. cerevisiae*, is likely missing some regions required to bind the Atg17-Atg31-Atg29 complex and/or Atg1. The actual region in *S. cerevisiae* Atg13 that promotes complex integrity is likely located closer to the C-terminus, as the complexes containing the larger Atg13 CTD construct appears to be more stable. An additional interesting observation was that the Atg13 FL construct did not purify as a pentamer but rather only a single weaker band for Atg13 FL was observed with Atg17-Atg31-Atg29. This may indicate that the N-terminus of Atg13 might inhibit interaction with the C-terminus of Atg1. Additionally, as the *E. coli* system used may not have been adequate for expression of full-length Atg13. Previous attempts at purifying full-length Atg13 overexpressed in *E. coli* showed that the protein was highly unstable and likely misfolded (see Appendix C.2). This instability, and perhaps poor expression, may explain the absence of Atg13 MD and the decreased intensity of Atg13 FL.

#### 4.2.2 The EM structure of the Atg1 kinase complex pentamer

With the purified pentamer assembly of Atg17-Atg31-Atg29-Atg1 CTD-Atg13 CTD in hand, we analyzed the complex by single-particle EM. Initial attempt to characterize the overall structure of the pentamer complex by EM was hampered by our inability to unambiguously locate the densities contributed by Atg1 and Atg13. We therefore applied limited glutaraldehyde cross-linking with the goal of improving the stability and integrity of the complex. 2D analysis of the cross-linked species showed that additional densities are present near the terminal regions of the Atg17-Atg31-Atg29 S-shape structure, which result in an overall enlarged and swollen look to these regions. This observation does not appear to be artificially induced by the glutaraldehyde, as a mock analysis of similarly cross-linked Atg17-Atg31-Atg29 did not result in any morphological changes to its overall architecture. In spite of this promising result, we were unable to clearly distinguish Atg1 CTD and Atg13 CTD from the weak additional densities.

A major factor that hampered our ability to visualize Atg1 CTD and Atg13 CTD from the Atg1 pentamer is the intrinsically disordered/unstructured nature of these fragments, which has been confirmed by sequence analysis with the IUPRED server (Figure 4.3). In particular, the entire C-terminal region of Atg13 (Residues 267-738) is predicted to be highly unstructured while central regions of Atg1 (residues 350-650) are moderately unstructured. When compared to our purified constructs, at least Atg13 CTD (residues 384-738) and the first 100 residues of Atg1 CTD (residues 562-831) are predicted to be highly unstructured. On the other hand, the N-terminal region of Atg13 predicted to be highly structured according to IUPRED has recently been crystallized<sup>95</sup>.

Intrinsically disordered proteins (IDPs) have been studied by electron microscopy previously in the literature<sup>132,133</sup>. These studies have shown that IDPs are typically not amenable to conventional EM analysis. When studied by single-particle EM, and subject to class average analysis, predicted IDPs exhibit partial or complete loss of density in observed particles. As a result, significant portion, if not the entire, IDP will be absent in the obtained image. This is what was observed in our analysis of the

untreated pentamer complex, in which very little additional density could be observed. With gradient fixation, specifically limited cross-linking, we had hoped to promote the occurrence of observing Atg1 CTD and Atg13 CTD, which was the case, despite the density appearing washed out and blurred. Indeed, a similar observation was seen using GraFix to study a complex of the IDP histone-chaperone nucleoplasmin with its histone H3-H4 substrate<sup>133</sup>. Their analysis revealed that the EM structure of the IDP nucleoplasmin exhibited a wider overall structure compared to the solved crystal structure. Thus, the potential to obtain meaningful structural data of the pentamer complex by EM appears to have reached a limit without the use of larger fragments.

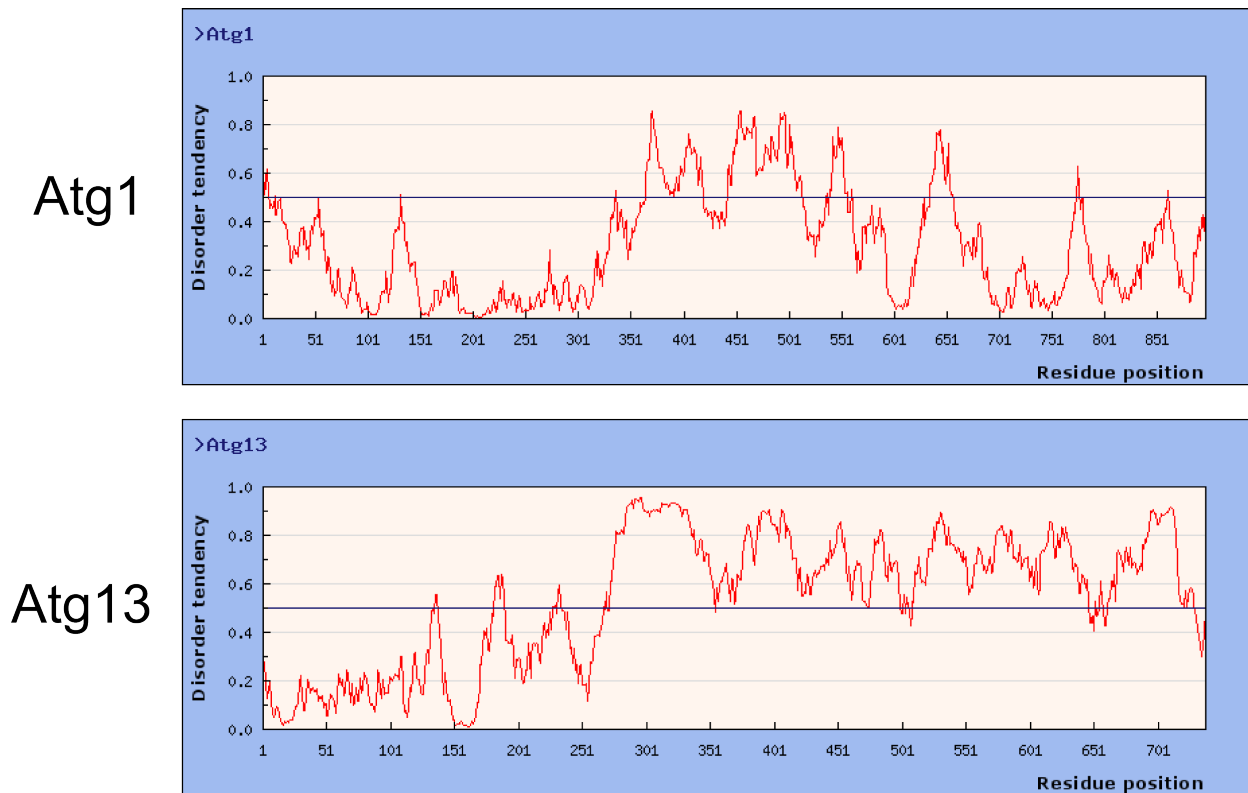


**Figure 4.3 Intrinsically disordered protein prediction of Atg1 and Atg13 by the IUPRED server.** Values of disorder tendency above 0.5 are considered to be highly disordered<sup>124,125</sup>.

To determine where Atg1 CTD and Atg13 CTD localized in the pentamer assembly we used fusion labels. We labelled Atg1 CTD or Atg13 CTD with an N-terminal His-MBP tag and the complexes was purified. His-MBPAtg1 CTD containing complex purified as a pentamer while His-MBP-Atg13 CTD containing complex purified as a complex with substoichiometric quantities of the Atg1 CTD component. These results suggest that the His-MBP-tag might occlude a potential binding site on Atg13 CTD that resulted in loss of Atg1 CTD. While the N-terminal region of the Atg1 CTD construct might have less of a role in complex integrity.

The purified His-MBP-labeled complexes were subject to single-particle EM and 2D class average analysis. The result of this analysis showed convincingly, unlike the unlabeled complex, that additional densities were localized in close proximity to the N-terminus of Atg17, as we have predicted. The densities observed for His-MBP-Atg13 CTD were conclusive with clear double-labelled particles indicating both Atg17 N-termini were interacting with His-MBP-Atg13 CTD. The densities observed for His-MBP-Atg1 CTD were less well defined but still reproducibly exhibited localization to similar areas at the N-terminus of Atg17. Together, these results support that the N-terminus of Atg17 does indeed form an Atg1-Atg13 interaction interface and further provides a basis for understanding the Atg1 kinase complex assembly. The Atg17-Atg31-Atg29 ternary complex constitutes a scaffold. As the complex is dimeric, this creates two nucleation points for complex assembly with Atg13 and Atg1 both localizing to the terminal regions of the S-shape scaffold (Figure 4.4). A result of this subunit organization is that two functional modules are formed. This structural configuration has broader implications in understanding the functions of the Atg1 kinase complex in both vesicle tethering and activation of Atg1 kinase activity.

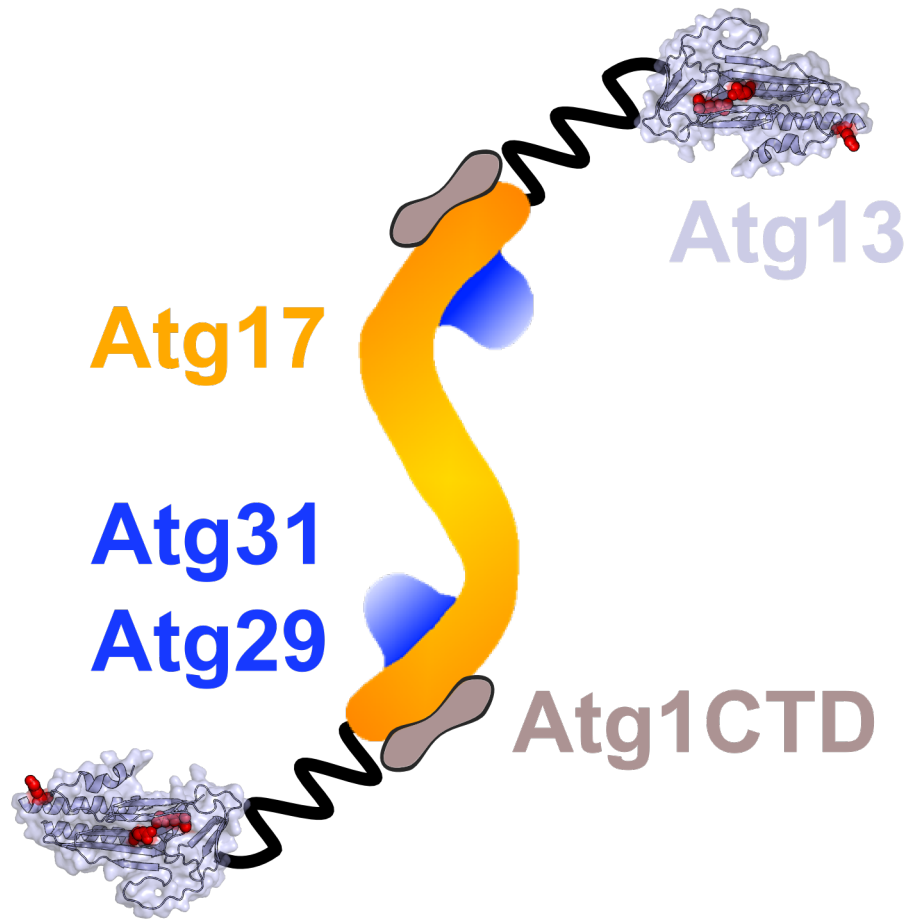


**Figure 4. 4 Model of Atg1 kinase complex assembly.** The EM structure of the dimeric Atg17-Atg31-Atg29 complex is shown; Atg17 (orange). Atg31 (blue), Atg29 (blue) is shown in complex with Atg13 (pale blue), depicting the crystal structure of the HORMA domain (PDB 4J2G) with an unstructured C-terminus (black), and Atg1 CTD (brown). Red residues from the Atg13-HORMA domain highlight putative PI(3)P interacting regions.

### 4.2.3 Models of Atg1 kinase complex function

Our structural data suggest a working model of how the Atg1 kinase complex functions to mediate autophagosome formation. During autophagosome formation, assembly of the Atg1 kinase complex is thought to have two important roles: tethering Atg9 vesicles and in activating Atg1 kinase activity. In yeast, Atg9 is a transmembrane protein found in high curvature 30-60 nm vesicles. During autophagy, Atg9 vesicles are localized to the PAS and provide the first membrane source for the growing autophagosome<sup>32</sup>. We propose that the Atg1 kinase complex can tether Atg9 vesicles that are mediated by the Atg17 and Atg1 components. Firstly, Atg17 can directly interact with Atg9<sup>34</sup>. As Atg17 is dimeric, the assembled Atg17-Atg31-Atg29 ternary complex can bind two Atg9 vesicles to mediate this tethering. Secondly, the Atg1 CTD domain has been shown to possess an intrinsic property to directly interact with high curvature vesicles<sup>92</sup>. Thus, assembly of the full Atg1 kinase complex can mediate Atg9 vesicle tethering through both a protein-protein interaction mediated by interaction of Atg17 with Atg9 and by an intrinsic property of Atg1 CTD to associate with membranes (Figure 4.5A). Furthermore, Atg1's association with the long-range TRAPPIII membrane-tethering complex may further promote Atg9 vesicle tethering at the PAS<sup>93</sup>. The positioning of Atg9 vesicles in the Atg1 kinase complex would place these vesicles into close proximity such that a SNARE protein complex would mediate the vesicle fusion. The exocytic Q/t-SNAREs, Sso1/2 and Sec9, have been implicated in the very early steps of autophagosome formation<sup>137</sup>.

Atg1 kinase activity has been shown to be indispensable for autophagosome formation in yeast<sup>83,84</sup>. Atg1 kinase activity is dependent on its association with Atg13 and Atg17<sup>83</sup>. Atg13's interaction in particular has been shown to promote Atg1 ability to auto-phosphorylate a key residue in the activation loop of the kinase<sup>83</sup>. This autophosphorylation event was essential for autophagy<sup>83,84</sup>. The subunit organization model generated from our structural studies suggests that assembly of the full Atg1 kinase complex could bring into close proximity two Atg1 subunits to promote autophosphorylation and activation of the Atg1 kinase (Figure 4.5B).

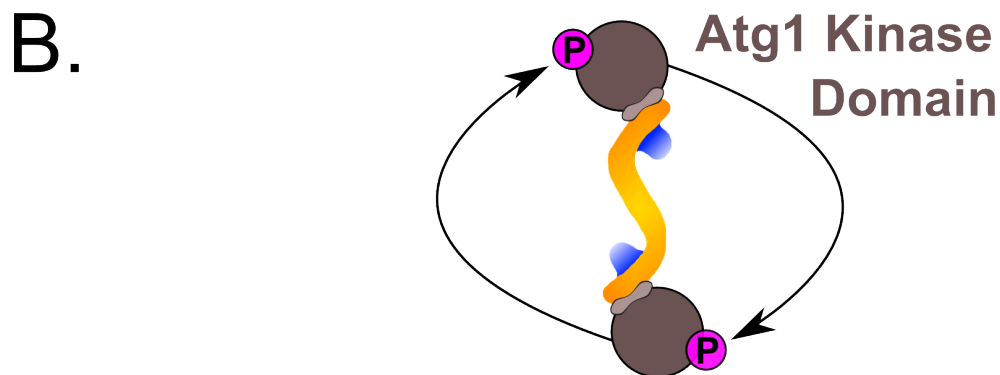
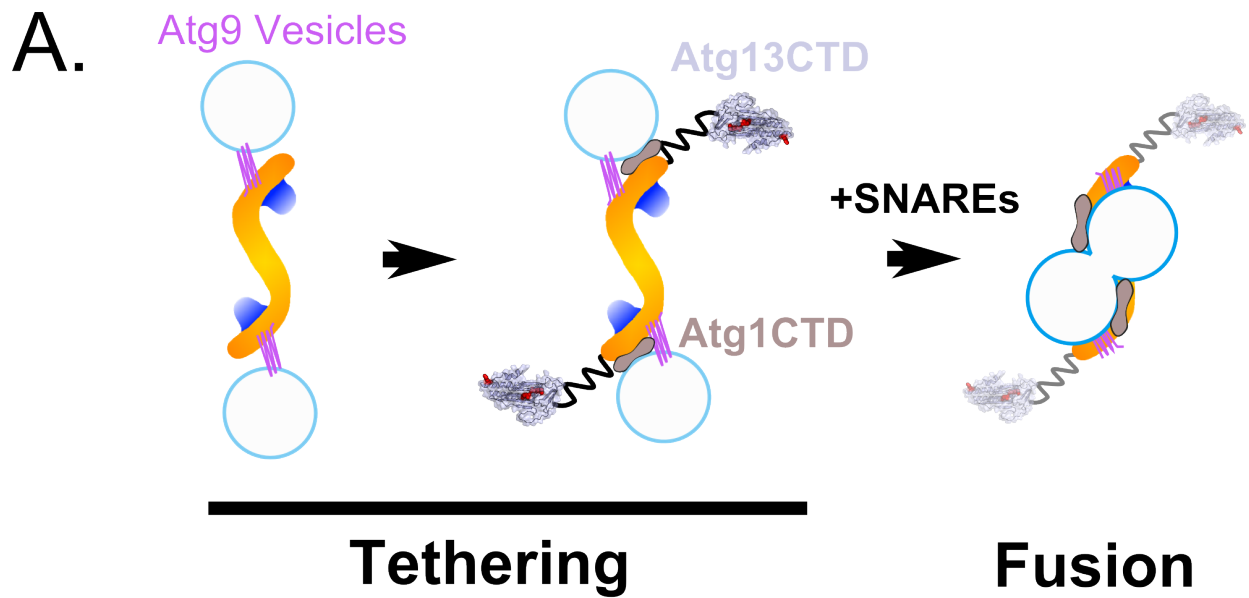


**Figure 4.5 Models of Atg1 kinase complex function.** (A) Model of vesicle tethering. High curvature Atg9 vesicles are tethered to the Atg1 kinase complex through two mechanisms; Atg9's association with Atg17 and through Atg1's intrinsic property to associate with membranes. Atg13 likely mediates a bridging interaction with Atg17 and Atg1 CTD. SNAREs likely have a role in mediating fusion of tethered Atg9 vesicles. (B) Model of Atg1 kinase activation. Dimeric Atg17-Atg31-Atg29 ternary complex can bring into close proximity two Atg1 subunits to promote autophosphorylation and Atg1 kinase activation.

### 4.3 The EM structure of Atg11

To characterize proteins that interact with the Atg1 kinase complex, we determined the structure of Atg11. Atg11 is an important autophagy protein required for facilitating formation of the PAS during both vegetative growth and starvation conditions. Atg11 is predicted to perform this through recruitment of proteins to the PAS in its function as a protein scaffold. In this role Atg11 has a similar function to Atg17. Indeed, secondary structure prediction predicts that Atg11 consists entirely of coiled-coils, similar to Atg17 (see Appendix C.3).

To facilitate this study we purified Atg11 from a yeast expression system. A eukaryotic expression system was necessary to express this 135-kDa protein as expression in *E. coli* showed that Atg11 mis-folded into large aggregates (unpublished data). Atg11 was purified and subject to single-particle EM and 2D class average analysis. Our results showed that Atg11 adopts an elongated and highly flexible architecture. Interestingly, these observed further suggest that Atg11 can homodimerize. Literature has predicted that the central domains of Atg11 are responsible for dimerization<sup>100</sup>, however we are unable to localize these particular regions in the observed images. Atg11 dimers do appear to transiently associate, as stable monomer forms of Atg11 were also observed.

The structure of Atg11 is indicative of coiled-coil containing protein<sup>134</sup>. Intriguingly, Atg11 adopts a remarkably similar architecture to the Atg17-Atg31-Atg29 complex. As both sets of proteins function in a similar role it is not surprising that they have similar structural features. Although the architecture of Atg17-Atg31-Atg29 is composed of three proteins Atg11 adopts a similar molecular architecture entirely on its own. The functional implication of this structural similarity remains to be discovered.

## Chapter 5. Conclusions

The Atg1 kinase complex, consisting of Atg1, Atg13, Atg17, Atg31 and Atg29, is an important hub for regulating autophagosome formation. However, structural insights into complex formation were, only until recently, completely unknown. We have determined the EM structure of the *Saccharomyces cerevisiae* Atg17-Atg31-Atg29 ternary complex. The entire complex is that of an “S-shaped” dimer with an elongated architecture  $\sim 345\text{\AA}$  long. Atg17 was found to form the central scaffold while Atg31 and Atg29 made up smaller globular domains appended to the S-shape. Additionally, Atg17 was found to mediate dimerization while Atg31 and Atg29 are suggested to have a structural role in restricting flexibility of Atg17. We further showed that a minimal pentamer composed of Atg1 CTD (residues 589-897), Atg13 CTD (residues 384-738) and Atg17-Atg31-Atg29 could be purified. Through localization experiments, the structure of this minimal Atg1 kinase complex showed that both Atg1 CTD and Atg13 CTD localized to the N-terminal region of Atg17. Additionally, an interacting partner of the Atg1 kinase complex, Atg11, showed an elongated architecture indicative of its role as a coiled-coil protein scaffold. Our work provided supportive evidence for the physiological relevance of the recently published crystal structure of *L. thermotolerans* Atg17-Atg31-Atg29. Collectively, results from this thesis provide a framework for understanding Atg1 kinase complex assembly and how it functions to promote autophagosome formation.

## Chapter 6. Future Experiments

Despite the work presented in our study many questions still remain concerning Atg1 kinase complex formation. Importantly, we have only determined a low-resolution interface for interaction of Atg1 and Atg13 but have not fully determined the molecular details behind this interaction. One way to determine the contribution of individual residues contributing to the interaction interface is by way of chemical crosslinking and mass spectrometry<sup>135</sup>. This technique would be useful in resolving distinct residues required for interaction without the use of structural analysis.

We have proposed that Atg31 and Atg29 likely restrict Atg17 into an S-shape with well-defined curvature of its N-terminal region. It has yet to be shown whether the curvature of Atg17 has any role in mediating interaction of Atg1 and Atg13 or what the role Atg31 or Atg29 has in this interaction. Thus, simply a reconstitution of an Atg17-Atg13-Atg1 complex would provide insight into how Atg31 and Atg29 contribute to complex integrity.

Looking more closely at regulation, nearly all components are differentially phosphorylated in response to autophagy activation. Atg31 and Atg29 have increased phosphorylation<sup>88,99</sup>, Atg13<sup>73</sup> is largely dephosphorylated, while Atg1 is both phosphorylated and dephosphorylated<sup>73,74,75</sup>. As such, the complexes that we purified, except in the case of the phosphomimetic Atg29 mutants, represent non-physiologically relevant complexes. To further understand the role of post-translational modifications, identifying the phosphorylation state of each component and studying what effect that has on complex formation would be essential.

Studies in the yeast system provided useful insight into the mechanism of complex formation and function in higher eukaryotic systems. The ULK1 kinase complex<sup>80</sup> has been identified as an ortholog to the Atg1 kinase complex. Importantly, as autophagy has a role in human disease, modulation of autophagy at the level of induction would be an important target for future therapeutics. Ultimately, obtaining a structure of the ULK1/Atg1 kinase would provide the necessary foundation to propel development of small molecules targeting this important autophagy regulator.

## References

1. Mizushima, N. (2011). Autophagy in protein and organelle turnover. *Cold Spring Harb. Symp. Quant. Biol.* **76**, 397–402.
2. Myeku, N., and Figueiredo-Pereira, M. E. (2011) Dynamics of the degradation of ubiquitinated proteins by proteasomes and autophagy: association with sequestosome 1/p62. *J. Biol. Chem.* **286**, 22426–40.
3. Kaushik, S., Bandyopadhyay, U., Sridhar, S., Kiffin, R., Martinez-Vicente, M., Kon, M., Orenstein, S. J., Wong, E., and Cuervo, A. M. (2011) Chaperone-mediated autophagy at a glance. *J. Cell Sci.* **124**, 495–9.
4. Li, W., Li, J., and Bao, J. (2012) Microautophagy: lesser-known self-eating. *Cell. Mol. Life Sci.* **69**, 1125–36.
5. Reggiori, F., and Klionsky, D. J. (2013). Autophagic Processes in Yeast: Mechanism, Machinery and Regulation. *Genetics* **194**, 341–361.
6. Umekawa, M., and Klionsky, D. J. (2012) The Cytoplasm-to-Vacuole Targeting Pathway: A Historical Perspective. *Int. J. Cell Biol.* **2012**, 142634.
7. Debnath, J., and Murrow, L. (2012). Autophagy as a Stress-Response and Quality-Control Mechanism: Implications for Cell Injury and Human Disease. *Annu. Rev. Pathol. Mech. Dis.* **8**, 105-137.
8. Kroemer, G., Mariño, G., & Levine, B. (2010). Autophagy and the integrated stress response. *Mol. cell*, **40**, 280–93.
9. Lee, J.-A. (2012) Neuronal autophagy: a housekeeper or a fighter in neuronal cell survival? *Exp. Neurobiol.* **21**, 1–8.
10. Liu, E. Y., & Ryan, K. M. (2012). Autophagy and cancer--issues we need to digest. *J. Cell Sci.* **125**, 2349–58.
11. Choi, A. M. K., Ryter, S. W., and Levine, B. (2013). Autophagy in human health and disease. *N. Engl. J. Med.* **368**, 651–62.
12. Levine, B., & Kroemer, G. (2008). Autophagy in the pathogenesis of disease. *Cell*, **132**, 27–42.
13. Malicdan, M. C., Noguchi, S., Nonaka, I., Saftig, P., & Nishino, I. (2008). Lysosomal myopathies: an excessive build-up in autophagosomes is too much to handle. *Neuromuscul. Disord.* **18**, 521–9.

14. Kuballa, P., Nolte, W. M., Castoreno, A. B., & Xavier, R. J. (2012). Autophagy and the immune system. *Ann. Rev. Immun.* **30**, 611–46.
15. Rubinsztein, D. C., Mariño, G., & Kroemer, G. (2011). Autophagy and aging. *Cell.* **146**, 682–95.
16. Mizushima, N., & Levine, B. (2010). Autophagy in mammalian development and differentiation. *Nat. Cell Biol.* **12**, 823–30.
17. Eskelinen, E., Reggiori, F., Baba, M., & Seglen, P. O. (2011). Seeing is believing The impact of electron microscopy on autophagy research. *Autophagy.* **7**, 935–956.
18. Ashford, T. P., and Porter, K. R. (1962). Cytoplasmic Components in Hepatic Cell Lysosomes. *J. Cell Biol.* **12**, 198-202.
19. Nakatogawa, H., Suzuki, K., Kamada, Y., and Ohsumi, Y. (2009). Dynamics and diversity in autophagy mechanisms: lessons from yeast. *Nat. Rev. Mol. Cell Biol.* **10**, 458–67.
20. Suzuki, K., and Ohsumi, Y. (2007). Molecular machinery of autophagosome formation in yeast, *Saccharomyces cerevisiae*. *FEBS Lett.* **581**, 2156–61.
21. Takeshige, K., Baba, M., Tsuboi, S., Noda, T., & Ohsumi, Y. (1992). Autophagy in yeast demonstrated with proteinase-deficient mutants and conditions for its induction. *J. Cell Biol.* **119**, 301–11.
22. Tsukada, M., and Ohsumi, Y. (1993) Isolation and characterization of autophagy-defective mutants of *Saccharomyces cerevisiae*. *FEBS Lett.* **333**, 169–174.
23. Suzuki, K., Kubota, Y., Sekito, T., and Ohsumi, Y. (2007) Hierarchy of Atg proteins in pre-autophagosomal structure organization. *Genes Cells.* **12**, 209–18.
24. Suzuki, K., Akioka, M., Kondo-Kakuta, C., Yamamoto, H., and Ohsumi, Y. (2013) Fine mapping of autophagy-related proteins during autophagosome formation in *Saccharomyces cerevisiae*. *J. Cell Sci.* **126**, 2534–44.
25. Cheong, H., Nair, U., Geng, J., and Klionsky, D. J. (2008). The Atg1 Kinase Complex Is Involved in the Regulation of Protein Recruitment to Initiate Sequestering Vesicle Formation for Nonspecific Autophagy in *Saccharomyces cerevisiae*. *Mol. Biol. Cell.* **19**, 668–681.
26. Hailey, D. W., Rambold, A. S., Satpute-Krishnan, P., Mitra, K., Sougrat, R., Kim, P. K., and Lippincott-Schwartz, J. (2010) Mitochondria supply membranes for autophagosome biogenesis during starvation. *Cell.* **141**, 656–67.
27. Ge, L., Melville, D., Zhang, M., and Schekman, R. (2013) The ER-Golgi intermediate compartment is a key membrane source for the LC3 lipidation step of autophagosome biogenesis. *Elife.* **2**, e00947.

28. Hayashi-Nishino, M., Fujita, N., Noda, T., Yamaguchi, A., Yoshimori, T., and Yamamoto, A. (2009) A subdomain of the endoplasmic reticulum forms a cradle for autophagosome formation. *Nat. Cell Biol.* **11**, 1433–7.
29. Ravikumar, B., Moreau, K., Jahreiss, L., Puri, C., and Rubinsztein, D. C. (2010) Plasma membrane contributes to the formation of pre-autophagosomal structures. *Nat. Cell Biol.* **12**, 747–57.
30. Hamasaki, M., Furuta, N., Matsuda, A., Nezu, A., Yamamoto, A., Fujita, N., Oomori, H., Noda, T., Haraguchi, T., Hiraoka, Y., Amano, A., and Yoshimori, T. (2013) Autophagosomes form at ER-mitochondria contact sites. *Nature.* **495**, 389–93.
31. Mari, M., and Reggiori, F. (2010) Atg9 reservoirs, a new organelle of the yeast endomembrane system? *Autophagy.* **6**, 1221–3.
32. Yamamoto, H., Kakuta, S., Watanabe, T. M., Kitamura, A., Sekito, T., Kondo-Kakuta, C., Ichikawa, R., Kinjo, M., and Ohsumi, Y. (2012). Atg9 vesicles are an important membrane source during early steps of autophagosome formation. *J. Cell Biol.* **198**, 219–33.
33. Noda, T., Kim, J., Huang, W. P., Baba, M., Tokunaga, C., Ohsumi, Y., and Klionsky, D. J. (2000). Apg9p/Cvt7p is an integral membrane protein required for transport vesicle formation in the Cvt and autophagy pathways. *J. Cell Biol.* **148**, 465–80.
34. Sekito, T., Kawamata, T., Ichikawa, R., Suzuki, K., and Ohsumi, Y. (2009) Atg17 recruits Atg9 to organize the pre-autophagosomal structure. *Genes Cells.* **14**, 525–38.
35. Reggiori, F., Tucker, K. a, Stromhaug, P. E., and Klionsky, D. J. (2004). The Atg1-Atg13 complex regulates Atg9 and Atg23 retrieval transport from the pre-autophagosomal structure. *Dev. Cell.* **6**, 79–90.
36. Kakuta, S., Yamamoto, H., Negishi, L., Kondo-Kakuta, C., Hayashi, N., and Ohsumi, Y. (2012). Atg9 vesicles recruit vesicle-tethering proteins Trs85 and Ypt1 to the autophagosome formation site. *J. Bio. Chem.* **287**, 44261–9.
37. Lipatova, Z., Belogortseva, N., Zhang, X. Q., Kim, J., Taussig, D., and Segev, N. (2012) Regulation of selective autophagy onset by a Ypt/Rab GTPase module. *Proc. Natl. Acad. Sci. U.S.A.* **109**, 6981–6.
38. Kihara, a, Noda, T., Ishihara, N., and Ohsumi, Y. (2001) Two distinct Vps34 phosphatidylinositol 3-kinase complexes function in autophagy and carboxypeptidase Y sorting in *Saccharomyces cerevisiae*. *J. Cell Biol.* **152**, 519–30
39. Obara, K., Noda, T., Niimi, K., and Ohsumi, Y. (2008) Transport of phosphatidylinositol 3-phosphate into the vacuole via autophagic membranes in *Saccharomyces cerevisiae*. *Genes Cells.* **13**, 537–47.

40. Kihara, a, Noda, T., Ishihara, N., and Ohsumi, Y. (2001). Two distinct Vps34 phosphatidylinositol 3-kinase complexes function in autophagy and carboxypeptidase Y sorting in *Saccharomyces cerevisiae*. *J. Cell Biol.* **152**, 519–30.
41. Araki, Y., Ku, W.C., Akioka, M., May, A. I., Hayashi, Y., Arisaka, F., Ishihama, Yasushi., Ohsumi, Y. (2013). Atg38 is required for autophagy-specific phosphatidylinositol 3-kinase complex integrity. *J. Cell Biol.* **203**, 299–313.
42. Obara, K., Sekito, T., and Ohsumi, Y. (2006). Assortment of Phosphatidylinositol 3-Kinase Complexes—Atg14p Directs Association of Complex I to the Pre-autophagosomal Structure in *Saccharomyces cerevisiae*. *Mol. Biol. Cell.* **17**, 1527–1539.
43. Fogel, A. I., Dlouhy, B. J., Wang, C., Ryu, S.-W., Neutzner, A., Hasson, S. A., Sideris, D.P., Abeliovich, H., Youle, R. J. (2013). Role of membrane association and atg14-dependent phosphorylation in beclin-1-mediated autophagy. *Mol. Biol. Cell.* **33**, 3675–88.
44. Fan, W., Nassiri, A., and Zhong, Q. (2011). Autophagosome targeting and membrane curvature sensing by Barkor/Atg14(L). *Proc. Natl. Acad. Sci. U. S. A.* **108**, 7769–74.
45. Noda, N. N., Kobayashi, T., Adachi, W., Fujioka, Y., Ohsumi, Y., and Inagaki, F. (2012). Structure of the novel C-terminal domain of vacuolar protein sorting 30/autophagy-related protein 6 and its specific role in autophagy. *J. Biol. Chem.* **287**, 16256–66.
46. Tamura, N., Oku, M., Ito, M., Noda, N. N., Inagaki, F., and Sakai, Y. (2013) Atg18 phosphoregulation controls organellar dynamics by modulating its phosphoinositide-binding activity. *J. Cell Biol.* **202**, 685-98.
47. Obara, K., Sekito, T., Niimi, K., and Ohsumi, Y. (2008) The Atg18-Atg2 complex is recruited to autophagic membranes via phosphatidylinositol 3-phosphate and exerts an essential function. *J. Biol. Chem.* **283**, 23972–80.
48. Nice, D. C., Sato, T. K., Stromhaug, P. E., Emr, S. D., and Klionsky, D. J. (2002) Cooperative binding of the cytoplasm to vacuole targeting pathway proteins, Cvt13 and Cvt20, to phosphatidylinositol 3-phosphate at the pre-autophagosomal structure is required for selective autophagy. *J. Biol. Chem.* **277**, 30198–207.
49. Strømhaug, P. E., Reggiori, F., Guan, J., Wang, C.-W., and Klionsky, D. J. (2004) Atg21 is a phosphoinositide binding protein required for efficient lipidation and localization of Atg8 during uptake of aminopeptidase I by selective autophagy. *Mol. Biol. Cell.* **15**, 3553–66.
50. Ano, Y., Hattori, T., Oku, M., Mukaiyama, H., Baba, M., Ohsumi, Y., Kato, N., and Sakai, Y. (2005) A sorting nexin PpAtg24 regulates vacuolar membrane dynamics during pexophagy via binding to phosphatidylinositol-3-phosphate. *Mol. Biol. Cell.* **16**, 446–57.
51. Balla, T. (2013) Phosphoinositides: tiny lipids with giant impact on cell regulation. *Physiol. Rev.* **93**, 1019–137.

52. Kobayashi, T., Suzuki, K., and Ohsumi, Y. (2012). Autophagosome formation can be achieved in the absence of Atg18 by expressing engineered PAS-targeted Atg2. *FEBS Lett.* **586**, 2473–8.
53. Orsi, A., Razi, M., Dooley, H. C., Robinson, D., Weston, A. E., Collinson, L. M., and Tooze, S. A. (2012) Dynamic and transient interactions of Atg9 with autophagosomes, but not membrane integration, are required for autophagy. *Mol. Biol. Cell.* **23**, 1860–73
54. Mizushima, N., Noda, T., Yoshimori, T., Tanaka, Y., Ishii, T., George, M. D., Klionsky, D.J., Ohsumi, M., Ohsumi, Y. (1998). A protein conjugation system essential for autophagy. *Nature.* **395**, 395–8.
55. Ichimura, Y., Kirisako, T., Takao, T., Satomi, Y., Shimonishi, Y., Ishihara, N., Mizushima, N., Tanida, I., Kominami, E., Ohsumi, M., Noda, T., and Ohsumi, Y. (2000) A ubiquitin-like system mediates protein lipidation. *Nature.* **408**, 488–92.
56. Otomo, C., Metlagel, Z., Takaesu, G., and Otomo, T. (2012) Structure of the human ATG12~ATG5 conjugate required for LC3 lipidation in autophagy. *Nat. Struct. Mol. Biol.* **20**.
57. Fujioka, Y., Noda, N. N., Nakatogawa, H., Ohsumi, Y., and Inagaki, F. (2010). Dimeric coiled-coil structure of *Saccharomyces cerevisiae* Atg16 and its functional significance in autophagy. *J. Biol. Chem.* **285**, 1508–15.
58. Nair, U., Yen, W.-L., Mari, M., Cao, Y., Xie, Z., Baba, M., Reggiori, F., and Klionsky, D. J. (2012). A role for Atg8-PE deconjugation in autophagosome biogenesis. *Autophagy.* **8**, 780–793.
59. Nakatogawa, H., Ishii, J., Asai, E., and Ohsumi, Y. (2012). Atg4 recycles inappropriately lipidated Atg8 to promote autophagosome biogenesis. *Autophagy.* **8**, 1–10.
60. Yu, Z.-Q., Ni, T., Hong, B., Wang, H.-Y., Jiang, F.-J., Zou, S., Chen, Y., Zheng, X.-L., Klionsky, D. J., Liang, Y., et al. (2012). Dual roles of Atg8-PE deconjugation by Atg4 in autophagy. *Autophagy.* **8**, 1–10.
61. Teter, S. A., Eggerton, K. P., Scott, S. V, Kim, J., Fischer, A. M., and Klionsky, D. J. (2001) Degradation of lipid vesicles in the yeast vacuole requires function of Cvt17, a putative lipase. *J. Biol. Chem.* **276**, 2083–7.
62. Yang, Z., Huang, J., Geng, J., Nair, U., and Klionsky, D. J. (2006) Atg22 recycles amino acids to link the degradative and recycling functions of autophagy. *Mol. Biol. Cell* **17**, 5094–104.
63. Kamada, Y., Funakoshi, T., Shintani, T., Nagano, K., Ohsumi, M., and Ohsumi, Y. (2000) Tor-mediated induction of autophagy via an Apg1 protein kinase complex. *J. Cell Biol.* **150**, 1507–13.
64. Stephan, J. S., Yeh, Y.-Y., Ramachandran, V., Deminoff, S. J., and Herman, P. K. (2009) The Tor and PKA signaling pathways independently target the Atg1/Atg13 protein kinase complex to control autophagy. *Proc. Natl. Acad. Sci. U. S. A.* **106**, 17049–54.

65. Wang, Z., Wilson, W. A., Fujino, M. A., and Roach, P. J. (2001) Antagonistic controls of autophagy and glycogen accumulation by Snf1p, the yeast homolog of AMP-activated protein kinase, and the cyclin-dependent kinase Pho85p. *Mol. Cell. Biol.* **21**, 5742–52.
66. Kim, J., Kundu, M., Viollet, B., and Guan, K.-L. (2011) AMPK and mTOR regulate autophagy through direct phosphorylation of Ulk1. *Nat. Cell Biol.* **13**, 132–41.
67. Noda, T. and Ohsumi, Y. (1998) Tor, a Phosphatidylinositol Kinase Homologue, Controls Autophagy in Yeast. *J. Biol. Chem.* **273**, 3963–3966.
68. Zoncu, R., Efeyan, A., and Sabatini, D. M. (2011) mTOR: from growth signal integration to cancer, diabetes and ageing. *Nat. Rev. Mol. Cell Biol.* **12**, 21–35.
69. Yorimitsu, T., Zaman, S., Broach, J. R., and Klionsky, D. J. (2007) Protein kinase A and Sch9 cooperatively regulate induction of autophagy in *Saccharomyces cerevisiae*. *Mol. Biol. Cell.* **18**, 4180–9.
70. Budovskaya, Y. V., Stephan, J. S., Reggiori, F., Klionsky, D. J., and Herman, P. K. (2004) The Ras/cAMP-dependent protein kinase signaling pathway regulates an early step of the autophagy process in *Saccharomyces cerevisiae*. *J. Biol. Chem.* **279**, 20663–71.
71. Urban, J., Souillard, A., Huber, A., Lippman, S., Mukhopadhyay, D., Deloche, O., Wanke, V., Anrather, D., Ammerer, G., Riezman, H., Broach, J. R., De Virgilio, C., Hall, M. N., and Loewith, R. (2007) Sch9 is a major target of TORC1 in *Saccharomyces cerevisiae*. *Mol. Cell.* **26**, 663–74.
72. Stephan, J. S., and Herman, P. K. The regulation of autophagy in eukaryotic cells: do all roads pass through Atg1? *Autophagy.* **2**, 146–8.
73. Kamada, Y., Yoshino, K., Kondo, C., Kawamata, T., Oshiro, N., Yonezawa, K., and Ohsumi, Y. (2010) Tor directly controls the Atg1 kinase complex to regulate autophagy. *Mol. Cell. Biol.* **30**, 1049–58
74. Kijanska, M., Dohnal, I., Reiter, W., Kaspar, S., Stoffel, I., Ammerer, G., Kraft, C., and Peter, M. (2010) Activation of Atg1 kinase in autophagy by regulated phosphorylation. *Autophagy.* **6**, 1168–1178.
75. Yeh, Y.-Y., Shah, K. H., Chou, C.-C., Hsiao, H.-H., Wrasman, K. M., Stephan, J. S., Stamatakis, D., Khoo, K.-H., and Herman, P. K. (2011) The identification and analysis of phosphorylation sites on the Atg1 protein kinase. *Autophagy.* **7**, 716–726.
76. Cheong, H., Yorimitsu, T., Reggiori, F., Legakis, J. E., Wang, C., and Klionsky, D. J. (2005) Atg17 Regulates the Magnitude of the Autophagic Response. *Mol. Biol. Cell.* **16**, 3438–3453
77. Kawamata, T., Kamada, Y., Kabeya, Y., Sekito, T., and Ohsumi, Y. (2008) Organization of the Pre-autophagosomal Structure Responsible for Autophagosome Formation. *Mol. Biol. Cell.* **19**, 2039–2050

78. Cheong, H., Nair, U., Geng, J., and Klionsky, D. J. (2008) The Atg1 Kinase Complex Is Involved in the Regulation of Protein Recruitment to Initiate Sequestering Vesicle Formation for Nonspecific Autophagy in *Saccharomyces cerevisiae*. *Mol. Biol. Cell.* **19**, 668–681
79. Cao, Y., Nair, U., Yasumura-Yorimitsu, K., and Klionsky, D. J. (2009) A multiple ATG gene knockout strain for yeast two-hybrid analysis. *Autophagy.* **5**, 699–705
80. Ganley, I. G., Lam, D. H., Wang, J., Ding, X., Chen, S., and Jiang, X. (2009) ULK1.ATG13.FIP200 complex mediates mTOR signaling and is essential for autophagy. *J. Biol. Chem.* **284**, 12297–305.
81. Mercer, C. a, Kaliappan, A., and Dennis, P. B. (2009) A novel, human Atg13 binding protein, Atg101, interacts with ULK1 and is essential for macroautophagy. *Autophagy.* **5**, 649–62.
82. Matsuura, a, Tsukada, M., Wada, Y., and Ohsumi, Y. (1997) Apg1p, a novel protein kinase required for the autophagic process in *Saccharomyces cerevisiae*. *Gene.* **192**, 245–50.
83. Yeh, Y.-Y., Shah, K. H., and Herman, P. K. (2011) An Atg13 protein-mediated self-association of the Atg1 protein kinase is important for the induction of autophagy. *J. Biol. Chem.* **286**, 28931–9.
84. Yeh, Y.-Y., Wrasman, K., and Herman, P. K. (2010) Autophosphorylation within the Atg1 activation loop is required for both kinase activity and the induction of autophagy in *Saccharomyces cerevisiae*. *Genetics.* **185**, 871–82.
85. Abeliovich, H., Zhang, C., Dunn, W. A., Shokat, K. M., and Klionsky, D. J. (2003) Chemical genetic analysis of Apg1 reveals a non-kinase role in the induction of autophagy. *Mol. Biol. Cell.* **14**, 477–90.
86. Deminoff, S. J., and Herman, P. K. Identifying Atg1 Substrates: Four Means to an End. *Autophagy.* **3**, 667–673.
87. Russell, R. C., Tian, Y., Yuan, H., Park, H. W., Chang, Y.-Y., Kim, J., Kim, H., Neufeld, T. P., Dillin, A., and Guan, K.-L. (2013) ULK1 induces autophagy by phosphorylating Beclin-1 and activating VPS34 lipid kinase. *Nat. Cell Biol.* **15**, 1–12.
88. Kabeya, Y., Noda, N. N., Fujioka, Y., Suzuki, K., Inagaki, F., and Ohsumi, Y. (2009) Characterization of the Atg17–Atg29–Atg31 complex specifically required for starvation-induced autophagy in *Saccharomyces cerevisiae*. *Biochem. Biophys. Res. Commun.* **389**, 612–15.
89. Kraft, C., Kijanska, M., Kalie, E., Siergiejuk, E., Lee, S. S., Semplicio, G., Stoffel, I., Brezovich, A., Verma, M., Hansmann, I., Ammerer, G., Hofmann, K., Tooze, S., and Peter, M. (2012) Binding of the Atg1/ULK1 kinase to the ubiquitin-like protein Atg8 regulates autophagy. *EMBO J.* **31**, 3691–703.

90. Nakatogawa, H., Ohbayashi, S., Sakoh-Nakatogawa, M., Kakuta, S., Suzuki, S. W., Kirisako, H., Kondo-Kakuta, C., Noda, N. N., Yamamoto, H., and Ohsumi, Y. (2012) The Autophagy-Related Protein Kinase Atg1 Interacts with the Ubiquitin-Like Protein Atg8 via the Atg8 Family Interacting Motif to Facilitate Autophagosome Formation. *J. Biol. Chem.* **287**, 28503–507.
91. Kabeya, Y., Kamada, Y., Baba, M., Takikawa, H., Sasaki, M., and Ohsumi, Y. (2005) Atg17 Functions in Cooperation with Atg1 and Atg13 in Yeast Autophagy. **16**, 2544–2553
92. Ragusa, M. J., Stanley, R. E., and Hurley, J. H. (2012) Architecture of the Atg17 Complex as a Scaffold for Autophagosome Biogenesis. *Cell.* **151**, 1501–12.
93. Wang, J., Menon, S., Yamasaki, a., Chou, H.-T., Walz, T., Jiang, Y., and Ferro-Novick, S. (2013) Ypt1 recruits the Atg1 kinase to the preautophagosomal structure. *Proc. Natl. Acad. Sci. U. S. A.* **110**, 9800-5.
94. Funakoshi, T., Matsuura, a, Noda, T., and Ohsumi, Y. (1997) Analyses of APG13 gene involved in autophagy in yeast, *Saccharomyces cerevisiae*. *Gene.* **192**, 207–13.
95. Jao, C. C., Ragusa, M. J., Stanley, R. E., and Hurley, J. H. (2013) A HORMA domain in Atg13 mediates PI 3-kinase recruitment in autophagy. *Proc. Natl. Acad. Sci. U. S. A.* **110**, 5486-91.
96. Sironi, L., Mapelli, M., Knapp, S., De Antoni, A., Jeang, K.-T., and Musacchio, A. (2002) Crystal structure of the tetrameric Mad1-Mad2 core complex: implications of a “safety belt” binding mechanism for the spindle checkpoint. *EMBO J.* **21**, 2496–506.
97. Kabeya, Y., Kawamata, T., Suzuki, K., and Ohsumi, Y. (2007) Cis1/Atg31 is required for autophagosome formation in *Saccharomyces cerevisiae*. *Biochem. Biophys. Res. Commun.* **356**, 405–10 .
98. Kawamata, T., Kamada, Y., Suzuki, K., Kuboshima, N., Akimatsu, H., Ota, S., Ohsumi, M., and Ohsumi, Y. (2005) Characterization of a novel autophagy-specific gene, ATG29. *Biochem. Biophys. Res. Commun.* **338**, 1884–9
99. Mao, K., Chew, L. H., Inoue-Aono, Y., Cheong, H., Nair, U., Popelka, H., Yip, C. K., and Klionsky, D. J. (2013) Atg29 phosphorylation regulates coordination of the Atg17-Atg31-Atg29 complex with the Atg11 scaffold during autophagy initiation. *Proc. Natl. Acad. Sci. U. S. A.* **110**, E2875–84.
100. Kim, J., Kamada, Y., Stromhaug, P. E., Guan, J., Hefner-Gravink, a, Baba, M., Scott, S. V, Ohsumi, Y., Dunn, W. a, and Klionsky, D. J. (2001) Cvt9/Gsa9 functions in sequestering selective cytosolic cargo destined for the vacuole. *J. Cell Biol.* **153**, 381–96.
101. Yorimitsu, T., and Klionsky, D. J. (2005) Atg11 Links Cargo to the Vesicle-forming Machinery in the Cytoplasm to Vacuole Targeting Pathway. *Mol. Biol. Cell.* **16**, 1593–1605
102. Sander, B., and Golas, M. M. (2011) Visualization of bionanostructures using transmission electron microscopical techniques. *Microsc. Res. Tech.* **74**, 642–63

103. Rossmann, M. G. (2000) Fitting atomic models into electron-microscopy maps. *Acta Crystallogr. D. Biol. Crystallogr.* **56**, 1341–9.
104. Trabuco, L. G., Villa, E., Mitra, K., Frank, J., and Schulten, K. (2008) Flexible fitting of atomic structures into electron microscopy maps using molecular dynamics. *Structure.* **16**, 673–83
105. Rossmann, M. G. (2000) Fitting atomic models into electron-microscopy maps. *Acta Crystallogr. D. Biol. Crystallogr.* **56**, 1341–9
106. Beck, F., Unverdorben, P., Bohn, S., Schweitzer, A., Pfeifer, G., Sakata, E., Nickell, S., Plitzko, J. M., Villa, E., Baumeister, W., and Förster, F. (2012) Near-atomic resolution structural model of the yeast 26S proteasome. *Proc. Natl. Acad. Sci. U. S. A.* **109**, 14870–5.
107. Bai, X.-C., Fernandez, I. S., McMullan, G., and Scheres, S. H. (2013) Ribosome structures to near-atomic resolution from thirty thousand cryo-EM particles. *Elife.* **2**, e00461
108. Puig, O., Caspary, F., Rigaut, G., Rutz, B., Bouveret, E., Bragado-Nilsson, E., Wilm, M., and Séraphin, B. (2001) The Tandem Affinity Purification (TAP) Method: A General Procedure of Protein Complex Purification. *Methods.* **24**, 218–229
109. Guthrie, C., Fink, G. R., Daniel Gietz, R., & Woods, R. A. (2002). Transformation of yeast by lithium acetate/single-stranded carrier DNA/polyethylene glycol method. *Methods Enzymol.*, **350**, 87–96.
110. Van Petegem, F., Clark, K. A., Chatelain, F. C., & Minor, D. L. (2004). Structure of a complex between a voltage-gated calcium channel beta-subunit and an alpha-subunit domain. *Nature.* **429**, 671–5.
111. Waldo, G. S., Standish, B. M., Berendzen, J., & Terwilliger, T. C. (1999). Rapid protein-folding assay using green fluorescent protein. *Nat. Biotech.* **17**, 691–5.
112. Scheich, C., Kümmel, D., Soumailakakis, D., Heinemann, U., and Büsow, K. (2007) Vectors for co-expression of an unrestricted number of proteins. *Nucleic Acids Res.* **35**, e43.
113. van den Ent, F., and Löwe, J. (2006) RF cloning: a restriction-free method for inserting target genes into plasmids. *J. Biochem. Biophys. Methods.* **67**, 67–74.
114. Kastner, B., Fischer, N., Golas, M. M., Sander, B., Dube, P., Boehringer, D., Hartmuth, K., Deckert, J., Hauer, F., Wolf, E., Uchtenhagen, H., Urlaub, H., Herzog, F., Peters, J. M., Poerschke, D., Lührmann, R., and Stark, H. (2008) GraFix: sample preparation for single-particle electron cryomicroscopy. *Nat. Methods* **5**, 53–5
115. Ohi, M., Li, Y., Cheng, Y., and Walz, T. (2004) Negative Staining and Image Classification - Powerful Tools in Modern Electron Microscopy. *Biol. Proced. Online* **6**, 23–34
116. Ludtke, S. J., Baldwin, P. R., and Chiu, W. (1999) EMAN: semiautomated software for high-resolution single-particle reconstructions. *J. Struct. Biol.* **128**, 82–97

117. Frank, J., Radermacher, M., Penczek, P., Zhu, J., Li, Y., Ladjadj, M., and Leith, A. (1996) SPIDER and WEB: processing and visualization of images in 3D electron microscopy and related fields. *J. Struct. Biol.* **116**, 190–9.
118. Pettersen, E. F., Goddard, T. D., Huang, C. C., Couch, G. S., Greenblatt, D. M., Meng, E. C., and Ferrin, T. E. (2004) UCSF Chimera--a visualization system for exploratory research and analysis. *J. Comput. Chem.* **25**, 1605–12.
119. Cherry, J. M., Hong, E. L., Amundsen, C., Balakrishnan, R., Binkley, G., Chan, E. T., Christie, K. R., Costanzo, M. C., Dwight, S. S., Engel, S. R., Fisk, D. G., Hirschman, J. E., Hitz, B. C., Karra, K., Krieger, C. J., Miyasato, S. R., Nash, R. S., Park, J., Skrzypek, M. S., Simison, M., Weng, S., and Wong, E. D. (2012) Saccharomyces Genome Database: the genomics resource of budding yeast. *Nucleic Acids Res.* **40**, D700–5.
120. The UniProt Consortium (2013) Update on activities at the Universal Protein Resource (UniProt) in 2013. *Nucleic Acids Res.* **41**, D43–7.
121. Larkin, M. A., Blackshields, G., Brown, N. P., Chenna, R., McGettigan, P. A., McWilliam, H., Valentin, F., Wallace, I. M., Wilm, A., Lopez, R., Thompson, J. D., Gibson, T. J., and Higgins, D. G. (2007) Clustal W and Clustal X version 2.0. *Bioinformatics.* **23**, 2947–8
122. Goujon, M., McWilliam, H., Li, W., Valentin, F., Squizzato, S., Paern, J., and Lopez, R. (2010) A new bioinformatics analysis tools framework at EMBL-EBI. *Nucleic Acids Res.* **38**, W695–9
123. Lupas, A., Van Dyke, M., and Stock, J. (1991) Predicting coiled coils from protein sequences. *Science.* **252**, 1162–4.
124. Dosztányi, Z., Csizmok, V., Tompa, P., and Simon, I. (2005) IUPred: web server for the prediction of intrinsically unstructured regions of proteins based on estimated energy content. *Bioinformatics.* **21**, 3433–4
125. Dosztányi, Z., Csizmók, V., Tompa, P., and Simon, I. (2005) The pairwise energy content estimated from amino acid composition discriminates between folded and intrinsically unstructured proteins. *J. Mol. Biol.* **347**, 827–39
126. Kampmann, M., and Blobel, G. (2009) Three-dimensional structure and flexibility of a membrane-coating module of the nuclear pore complex. *Nat. Struct. Mol. Biol.* **16**, 782–8
127. Yip, C. K., and Walz, T. (2011) Molecular structure and flexibility of the yeast coatmer as revealed by electron microscopy. *J. Mol. Biol.* **408**, 825–31.
128. Ciferri, C., Lander, G. C., Maiolica, A., Herzog, F., Aebersold, R., and Nogales, E. (2012) Molecular architecture of human polycomb repressive complex 2. *Elife.* **1**, e00005
129. Ramey, V. H., Wong, A., Fang, J., Howes, S., Barnes, G., and Nogales, E. (2011) Subunit organization in the Dam1 kinetochore complex and its ring around microtubules. *Mol. Biol. Cell.* **22**, 4335–42.

130. Andersen, K. R., Onischenko, E., Tang, J. H., Kumar, P., Chen, J. Z., Ulrich, A., Liphardt, J. T., Weis, K., and Schwartz, T. U. (2013) Scaffold nucleoporins Nup188 and Nup192 share structural and functional properties with nuclear transport receptors. *Elife*. **2**, e00745.
131. Keskin, O., and Nussinov, R. (2005) Favorable scaffolds: proteins with different sequence, structure and function may associate in similar ways. *Protein Eng. Des. Sel.* **18**, 11–24
132. Smith, F. D., Reichow, S. L., Esseltine, J. L., Shi, D., Langeberg, L. K., Scott, J. D., and Gonen, T. (2013) Intrinsic disorder within an AKAP-protein kinase A complex guides local substrate phosphorylation. *Elife*. **2**, e01319.
133. Ramos, I., Fernández-Rivero, N., Arranz, R., Aloria, K., Finn, R., Arizmendi, J. M., Ausió, J., Valpuesta, J. M., Muga, A., and Prado, A. (2013) The intrinsically disordered distal face of nucleoplasmin recognizes distinct oligomerization states of histones. *Nucleic Acids Res.*, gkt899–
134. Kim, Y., Heuser, J. E., Waterman, C. M., and Cleveland, D. W. (2008) CENP-E combines a slow, processive motor and a flexible coiled coil to produce an essential motile kinetochore tether. *J. Cell Biol.* **181**, 411–9.
135. Leitner, A., Walzthoeni, T., Kahraman, A., Herzog, F., Rinner, O., Beck, M., and Aebersold, R. (2010) Probing native protein structures by chemical cross-linking, mass spectrometry, and bioinformatics. *Mol. Cell. Proteomics* **9**, 1634–49.
136. Karanasios, E., Stapleton, E., Manifava, M., Kaizuka, T., Mizushima, N., Walker, S. A., and Ktistakis, N. T. (2013) Dynamic association of the ULK1 complex with omegasomes during autophagy induction. *J. Cell Sci.* **126**, 5224–5238.
137. Nair, U., Jotwani, A., Geng, J., Gammoh, N., Richerson, D., Yen, W.-L., Griffith, J., Nag, S., Wang, K., Moss, T., Baba, M., McNew, J. a, Jiang, X., Reggiori, F., Melia, T. J., and Klionsky, D. J. (2011) SNARE proteins are required for macroautophagy. *Cell* **146**, 290–302.

# Appendix

## Appendix A: Cloning

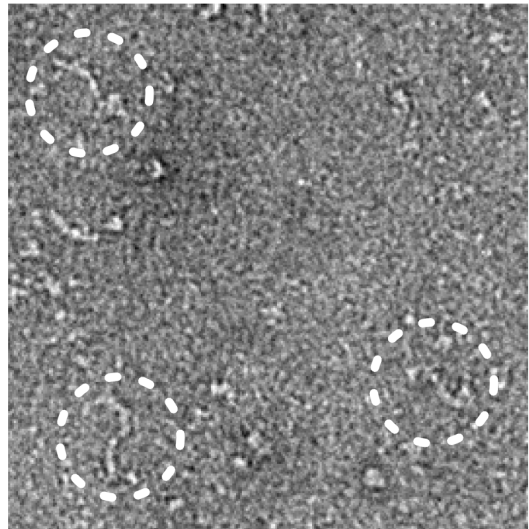
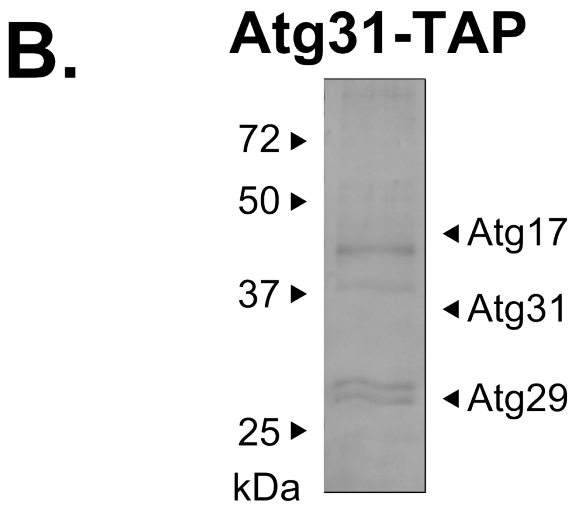
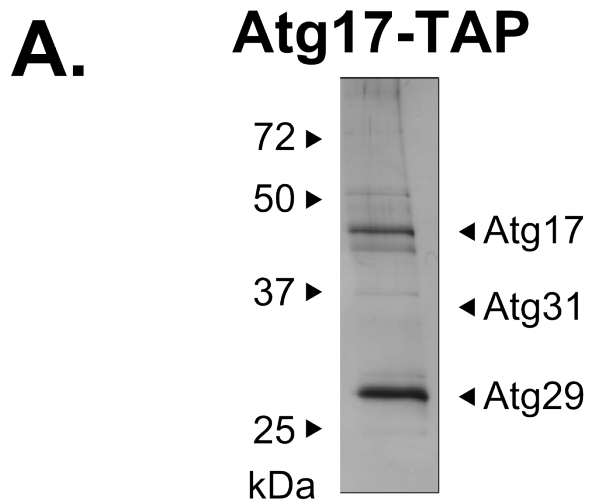
**Appendix Table A.1 Primers used for cloning**

Primer Name	Sequence	Vector	Expressed Construct
Atg17NdeIF	CCA CGG CAT ATG AAC GAA GCA GAT GTT ACA AAA TTT GTT AAT AAT GCC AG	pET28bHMT	HMT-Atg17
Atg17BamHIF	CCA CGG GGA TCC ATG AAC GAA GCA GAT GTT ACA AAA TTT GTT AAT AAT GCC AG	pGEX6P1	GST-Atg17
Atg17NotIR	CCA CCG GCGGCCGCTA AGG ATT CTT CAC GTT GTA ATT TAA AGT GTA CAG GGA AG	pGex6p1	HMT-Atg17
		pET28bHMT	
Atg31BamHIF	CCA CGG G GAT CCG ATG AAT GTT ACA GTT ACT GTT TAT GAT AAA AAT GTC AAG TAC AGA	pET Duet1	6xHis-Atg31
		pColADuet1	
Atg31HindIIIR	CCA CCG AAGCT TCA TAC GGA ATT GGA GAG CAT TTG TAA TTG TTC ATT	pET Duet1	6xHis-Atg31
		pColADuet1	
Atg29NdeIF	CCA CGG CAT ATG ATT ATG AAT AGT ACA AAC ACA GTT GTA TAT ATC AAA GTT AAG GGT AG	pET Duet1	Atg29
		pColADuet1	
Atg29XhoIR	CCA CCG CTC GAG TCA GAA TTG CAA TCT GTC CAT TAG CGC TTC TTC	pET Duet1	Atg29
		pColADuet1	
TEVeGFPNotIF	cca egg GCGGCCGCA CTC GAA AAC CTG TAC TTC CAA TCC GTG AGC AAG GGC GAG GAG C	C-terminal GFP in MCS1	--
eGFPAflII	cca egg CTT AAG TTA CTT GTA CAG CTC GTC CAT GCC G	C-terminal GFP in MCS1	--
TEVeGFPXhoIF	cca egg CTC GAG CTC GAA AAC CTG TAC TTC CAA TCC GTG AGC AAG GGC GAG GAG C	C-terminal GFP in MCS1	--
eGFPAvrIIIR	cca egg CCT AGG TTA CTT GTA CAG CTC GTC CAT GCC G	C-terminal GFP in MCS1	--
Atg31NotIRnostonp	CCA CCG GC GGC CGC TAC GGA ATT GGA GAG CAT TTG TAA TTG TTC ATT	pGFPC1	Atg31-GFP
Atg29XhoIRnostonp	CCA CCG CTC GAG GAA TTG CAA TCT GTC CAT TAG CGC TTC TTC	pGFPC2	Atg31-GFP
Atg31Not1R	CCA CCG GC GGC CGC TAGTGATGGTGTATGGTGTATG TAC GGA ATT GGA GAG CAT TTG TAA	pQLINK	Atg31-6xHIS
Atg1BamHIF	cca egg GGA TCC AATACTAATATCGTTAGTATTTTGGAACTCTCTGGCCGCAAAG	pQLINK	Atg1
Atg1NotIR	CCA CCG GCGGCCGCTAATTTTGGTGGTTCATCTTCTGCCTCAATATTTTCAAC	pQLINK	Atg1
Atg13-RF1F	CATTAAGAGGAGAAAATTAACATG GTTGCCGAAGAG GACATCGAGAAG	pQLINK	Atg13FL
Atg13-RF738R	CTTCATGCATGCGAAGACTGGATCC TTAACCTTCTTTAGAAAAGTTTCATATCACTCATG	pQLINK	Atg13CTD/FL
Atg13RF384F	CATTAAGAGGAGAAAATTAACATG AGTGCGAGCAGAAATCCCTCTAATTCATCG	pQLINK	Atg13MD/CTD
Atg13RF602R	CTTCATGCATGCGAAGACTGGATCC TCA ACT CTC TCC ACC AAA AAT AGG AGG TAA GC	pQLINK	Atg13MD
Atg11RFf	catcaaaaaaaagtaagaattttgaaaattc ATGGCAGACGCTGATGAATATAGCAC	pESC	Atg11
Atg11RFr	Gtaatccatcgatactagtgcggccgc AACTCCCTGGTATGAAACCACAAC	pESC	Atg11

**Appendix Table A.2 Plasmids for bacterial expression**

	Plasmid	Insert	Cloning	Cloning Cut Sites
pLC001	pET28bHMT	Atg17	Restriction Digest	NdeI/NotI
pLC002	pGEX-6p1	Atg17	Restriction Digest	BamHI/NotI
pLC003	pET-Duet1	Atg31/Atg29	Restriction Digest	Atg31: BamHI/HindI II Atg29: NdeI/XhoI
pLC003	pColA-Duet1	Atg31/Atg29	Restriction Digest	Atg31: BamHI/HindI II Atg29: NdeI/XhoI
pLC004	pGFP-MCS1C-Duet1	Atg31GFP/Atg29	Restriction Digest	Atg31: BamHI/NotI Atg29: NdeI/XhoI
pLC005	pGFP-MCS2C-Duet1	Atg31/Atg29GFP	Restriction Digest	Atg31: BamHI/HindI II Atg29: NdeI/XhoI
pLC006	pET Duet1	Atg31/Atg29[3SD]	Restriction Digest	Atg31: BamHI/HindI II Atg29: NdeI/XhoI
pLC007	pET Duet1	Atg31/Atg29[20SA3SD]	Restriction Digest	Atg31: BamHI/HindI II Atg29: NdeI/XhoI
pLC008	pQLINK-N	Atg17/Atg29/Atg31	pQLINKing	--
pLC009	pQLINK-N	Atg17/Atg29/Atg31- 6xHis/Atg1CTD/Atg13MD	pQLINKing	--
pLC010	pQLINK-N	Atg17/Atg29/Atg31- 6xHis/Atg1CTD/Atg13CTD	pQLINKing	--
pLC011	pQLINK-N	Atg17/Atg29/Atg31-6xHis/Atg1CTD/Atg13FL	pQLINKing	--
pCL012	pQLINK-N	Atg17/Atg29/Atg31-6xHis/MBP- Atg1CTD/Atg13CTD	pQLINKing	--
pCL013	pQLINK-N	Atg17/Atg29/Atg31-6xHis/Atg1CTD/MBP- Atg13CTD	pQLINKing	--
pCL014	pESC-Ura	Atg11	Restriction Free Cloning	--

Appendix B: Results



**Appendix B.1 *In vivo* purification of Atg17-TAP and Atg13-TAP strains. analyzed by 12% SDS-PAGE visualized by silver-stain. Analyzed by negative-stain EM. (A) Atg17-TAP (B) Atg31-TAP.**

**Appendix Table B.2 Mass spectrometry of TAP purified Atg17-Atg31-Atg29.**

	Number of Peptides	Coverage by amino acid account (%)
Atg17	27	66.43
Atg29	9	63.38
Atg31	9	63.78

Appendix C: Discussion

```

CAGL -----MPESLAERARSTLLKAQVLCREVESRIAEVKDRLSQWE--KNRHTLRF 46
ZYRO -----MSNEVTDIFVSNARNFLVEAQVLCCEEASMRIVGAKGELSKWQ--QDVSKLRF 50
SACE -----MNEADVTKFVNNARKTLTDAQLLCSANLRIVDIKKLSSWQ--LSISKLN 50
LATH -----MNEAVIEKLENSRKFLTGAKLICQESNDHLTTTKLRIREWQ--KFQSKLHF 50
KLLA --MSDAATTIPSDEIDKLWNKARNQLVEAQVECEESLKILSKVRTEMSSQ--KSRFKLKF 57
ASGO -----MSSSNQVKGFYFNAQRRLSRAQALCONSODTLHNMQLLVRWQ--RTVSKLQF 51
SCPO -----MELLQQWTQQAKAALTQARQLCGDAHKNFEDAKTDLRNSI--KQHQQKLE 48
YALI -----MEQLFREQDALAAAGPLCQESQDVLARARQNLEVAV--HLGIRTQF 45
CAAL MTNEINSATVTQDEVIKWSREAQSTLEKTQKICTDAQSSMQTAQELTILIPDKLQAI 60
      .:: * : * . : .

CAGL LVSCLEHQLG--FLEQCALRQIGRALIETEWVQVVLVDLVNEMKLWYDKIQRLRLERLDQV 105
ZYRO MISCLKSQGD--FLYKNVLKVGIGENLIKTEWVQVMLVDLIKTMKYWQDQISARVAQLNNI 109
SACE LIVGLRQGGK--FLYT--ILKEGIGTKLQKQWNQAVLVVLVDEMKYWQYEITSKVQRLDGI 108
LATH VLDCIQQQTK--FLSEILLREGIGRNLIEEESQTVLVRVNDMKFWQNEITKMMNKLDNI 109
KLLA ILNCLVNQVE--FFKNIMLEKCI STELIDNEWSKLVLVEIVNDVSYWQNEITTKMKILQGT 116
ASGO TIHCICNQTV--FLAECILKKTVGQQLIETEWKRMLLDELOGEMQRSQEIEITGKIDALRRT 110
SCPO LAKLTASQCT--RLDS-----STALIKQLLDLVQNYPTFNQNLVHDLRLESSLKRRLDC 100
YALI LAKAHAHQWT--LASK-----FYSNALTRTKKSLQTVTRQOTRFOAARGALEALGELAAT 99
CAAL LFKSYREQYDSILKQIETTKIYLHTNIDKVFNDIKDLLDPSLARLNNILLELKKTRVPSI 120
      * : :

CAGL ENILVADN-----KHLSHYISQEQALVLKRLDEVPIIRPQIENIQTYDTMCKVRVQK 159
ZYRO NNVLVSGNDTNDQNLGDFIPKENTHILDERLKEIPIIKQQIENITSQYHNMTKKVGEQ 169
SACE VNELISSEKDDTDPKLGDIYISRDNVNLLNDKLEVPVIERQIENIKLOYENMVRKVNKE 168
LATH TNEIDQQHN-----SKLGDIFISRDSSHILDSKLEIPTIRKQVENITROYQTMLAKVQSQ 164
KLLA KYDLTDDHS-----SLSDFICMDHVDILOQKIDEIPIIKQVQVNIROHYKSIKDRINQ 170
ASGO KNELDGGG-----ATLADFI SMENIFLLGDKLKDVPVQVEQVEHIKVQYSELVDKVVVEQ 164
SCPO TLDPALGSEY----TNLYAFVDDTALEDLKTRLRGV-----TDGVWNAFEKLAGLLEED 150
YALI PVQLRVNNG----AHNREFVDEDLISAQVQKGWNEVHEEALNVFRVLLPEIQR--HGD 153
CAAL VVEGTSEGK-----TLFDFTSIQSINLLKENIGIFKSNCSKIKNLLDLEVKEKLNIEQD 174
      * : .

CAGL LINKRLTE-----IKTIFDSQFGDEL TET--AELTEVKPRDLDSIELELVDIYINS 207
ZYRO LIFTRIKT-----VEATFNKNLGSESELEN--KTLSEIPEEMDNLEHELVEYINS 217
SACE LIDTKLTD-----VTQKFQSKFGIDNLME--TNVAEQFSRELTDLKDLAEIMNS 216
LATH LVESRMKG-----LRDEFSSKFGDQCREN--LKLNEEFTNEADQLEQELADFLKS 212
KLLA LVAVKLLK-----LRTYFDSHFSRDSKNNLFKLESYVTELNEFENELADFLRS 220
ASGO LQNNRVVK-----LEADFAAFAFRSGKNDF--NAFSMKYLQKIRQLETDLADILKS 212
SCPO LCANYHKR-----LEAVSLDFLPPAYNDT-----AEELADLLLQ 184
YALI IVNRSKKE-----FEREKAEQTELLIHQTS--DSGIYDLLNSAEACSEDMANLLQS 202
CAAL RMNSRWNKSVKMYDLIAPLQLELRALIHGASNES--NSFMGTILRENQALENELVSIEM 232
      . : : :

CAGL LTDHFDKQ---ALEKGLFNDSNE--YDELLKIVSADDSQLDDIMKHLNLTIDSTNHQID 262
ZYRO LTDHFDKCK---LLQSKKLEGPS---YQELLKVVTKDN GELGSIETLTKD TIRDVDQVLE 271
SACE LTQHFDKTL---LLQDKKIDNDE---REELFKVVQGDDELKELYNIFKTLHEVIDDVVK TIL 270
LATH FTDHFDKCS---ALSSRSVSPED---AQNLFEIVERDDKDLAAINSLLQDA AIDVASFVR 266
KLLA ITDHFDKCT---ILKEQQIPLPD---LKELFQIVKDDTQLENIRELVFETGLEVKAFSK 274
ASGO LTDHYDKCS---LLKAGDLPAAE---QAELEFVVKNDQELDSIMGVLEVIVRDIKSLAK 266
SCPO VAQHYDQCS---EALNIYDTLSDA--EKKDLQEVLQSDSNHVPVSVLTELRSGLDQTIHYFN 240
YALI LARHYDLCERGQDLSTGAIEAEDVNELGELRAVLEND AQQLPDVDELQERLDEVKQGCQ 262
CAAL QTNHFDQCMKAVELISSNGCDMN-----LGVLKND AQELPEVFKELTTIYDIILRNEE 286
      : * : : :

CAGL KVEYILDIKTKQKTILHGKINELIANCTKY-----SEYLAI FKG IATSIEKFK 310
ZYRO NFKNLLERKTIDKVNLSQINKLINEFHKH-----QEYLMIFKDISELISTFK 319
SACE NLGQFLQAKIKEKTELHSEVSEIINDFNRN-----LEYLLIFKDISNLDISFK 318
LATH KVNMLLDERDADKAKMQATLSKLLTELKHH-----EYISVFEGISALIQKFK 314
KLLA KVNETISEIMDKIGGFHLLASKIVTELEKC-----EYLSIFQKIANLVFVYK 322
ASGO NVSIRLRQKERDKQQLKNAMGKAHSELLKY-----EEHLTVFQGI DDLIRNFK 314
SCPO AVQSYKSKVDSATSILEALAEELNKNQLTN-----QRHEAAHELMRAQTG--- 285
YALI GVHNHMTQMYHSYSLEVRQLEGIQAVEKTM-----DATLEICETQQRDTKEYL 310
CAAL RSKKFLATHMPNIEKISDIVKEELAVFRKFKTEEIPRYTFLIAECENKLEKCSMPVKSDQ 346
      :

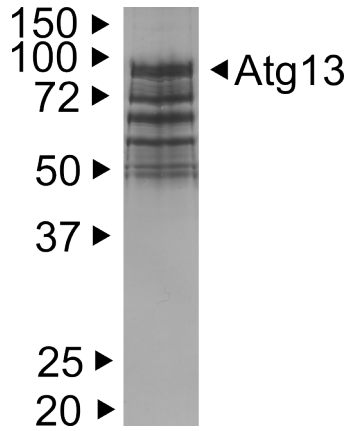
```

```

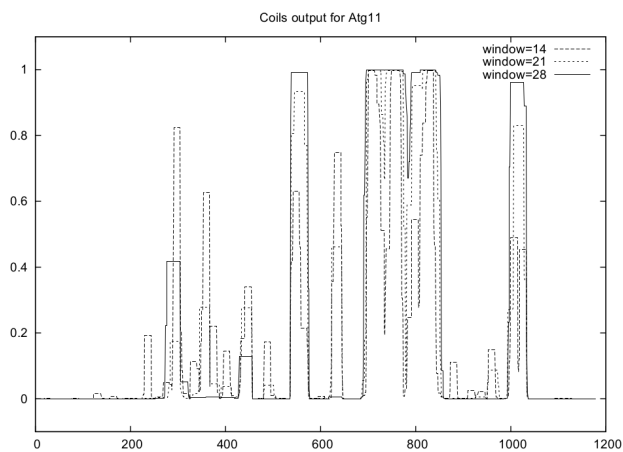
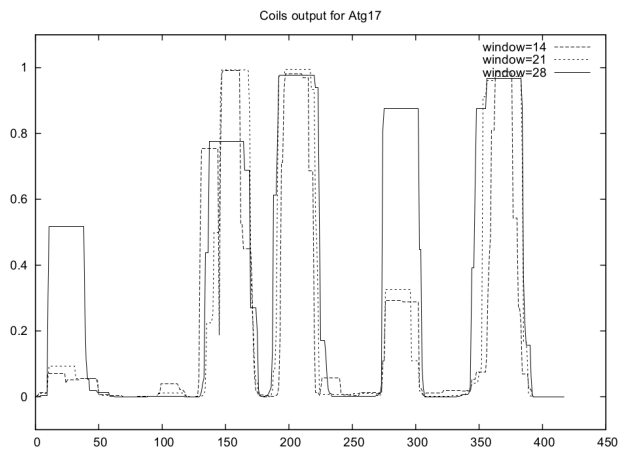
CAGL      EGCMQDIQLTKELYKFYDEFENSYNKLLQEVQRRRALSQK---MLGIIKNCENELKTLHD 367
ZYRO      ESCLQEVKLTKELCEFYQNFKTSYYNLLDEVERRRSVAQE---MTIVLQESQQKLHALHT 376
SACE      NSCTQDIQTTKELCEFYDNFEESYGNLVLEAKRRKDVANR---MKTILKDCEKQLQNLDA 375
LATH      ASCLEDIRQTRNLLDFYANFERSYHNLLKEVKRRKETAAK---LSQILKSCETQLEQINT 371
KLLA      ESCIKKIEQVQQLCEFYDKFKLGYKNLLRERDRRKATALQ---MEKILKECQEKLQALS 379
ASGO      ASCLHNVSKVRELCEFYDNFLNSYQVLLREVERRRRVAKQ---MEDILQACEGQLMALS 371
SCPO      LEIPQLAQELVQLERHYTHFAKAYTALLQEIHRRQTYENC---VRSIVDEFVGRLEKEQQ 342
YALI      LKVQRYVSETS AVVTHYQTFFLNSYKALLHEAERRNAEAK---MKDYVTEVNAKLAQMSI 367
CAAL      SPSQVYTQTLQELTEHYVKFINIYKTKYLAE LHHQQFTYPRKFLKKLTEFLNEDIYRIQI 406
          : . * * * * : : : : :
          :
CAGL      EDQKLRTHFLSENGAFLP-ETIWPGEIDDLSPLYALDYHIKEI----- 409
ZYRO      QDQKAREGFLSENANYLP-ETIWPBKIDDLTPLYSLDYTIKDI----- 418
SACE      QDQEERQNFIAENGTLYP-ETIWPBKIDDFSSLYTLNYNVKNP----- 417
LATH      ADLRERQMFLLENGNYLP-ETIWPDEIGSLSPLYTLNIEVRKV----- 413
KLLA      ADLDQRQQFLLENGDYLP-ENIWPGYIDDMESMYSFEYSIHNVPN----- 423
ASGO      TDLKQRQQFLMRHGDYLP-ENIWPGNIDDLSPLYDLEYRIKKV----- 413
SCPO      AEAACRIDFFNQYGDYLP-QTLWGAVTDPPLHFEIIEHQYTELPNVKVIPDKNDKSKQR 401
YALI      QETNRRQDFVAQQGDYLP-ADIWDEL LPSRRFEARELDGEL----- 408
CAAL      EESERRRQWTSRYGEFIPSEFKLPGEHELPIVQIIIEGLEYIQKEDGQEEEPNIGNEKE 466
          : * : . . : : *
          :
CAGL      -----
ZYRO      -----
SACE      -----
LATH      -----
KLLA      -----
ASGO      -----
SCPO      EKSSTTASKR 411
YALI      -----
CAAL      LMDMITGSNK 476

```

**Appendix C.1 Alignment of Atg17.** Alignment was performed with using ClustalW2<sup>121,122</sup>. SACE: *S. cerevisiae*. CAGL: *Candida Glabrata*. ZYRO: *Zygosaccharomyces Rouxxi*. LATH: *Lachaenea Thermotolerans*. KLLA: *Kluveryomyces Klactis*. ASGO: *Ashbya gossypii*. CAAL: *Candida albicans*. YALI: *Yarrowia lipolytica*. SCPO: *Schizosaccharomyces pombe*



**Appendix C.2 Purified Atg13 exhibiting multiple bands.**



**Appendix C.3 Coiled coil prediction for Atg17 and Atg11. Prediction was performed using the coiled-coil prediction server<sup>123</sup>. Atg17 (Top) and Atg11 (Bottom)**